

**Analysis of ice types along the northern coast of Ellesmere Island, Nunavut,  
Canada, and their relationship to Synthetic Aperture Radar (SAR) backscatter**

**Miriam Richer McCallum**

Thesis submitted to the Faculty of Graduate and Postdoctoral  
Affairs in partial fulfillment of the requirements  
for the degree of

Master of Science

In

Geography

Carleton University  
Ottawa, Ontario

Supervisors:

Dr. Derek Mueller (Carleton University)  
Dr. Luke Copland (University of Ottawa)

© 2015

Miriam Richer McCallum

## **Abstract**

Ice shelves and other ice features along the northern coast of Ellesmere Island are a complex mixture of ice originating from marine and meteoric sources. This is reflected in the considerable variability in Synthetic Aperture Radar (SAR) backscatter in remotely sensed imagery. This study analyzed the properties of three different ice types across the Milne and Petersen ice shelves and associated them with SAR backscatter. The results indicated that the grain diameter of each ice type was unique in horizontal thin sections and that bubble shape and size were associated with SAR variables. Furthermore, cores extracted from areas originally thought to be glacially-fed were identified as being marine in origin, suggesting that considerable surface ablation has taken place over the past three decades. This research offers the potential to improve our ability to assess long-term changes (past and future) of the ice cover along the northern coast of Ellesmere Island.

## **Acknowledgments**

I would like to thank the various organizations that funded this research: ArcticNet (a Network of Centres of Excellence of Canada), the Canada Foundation for Innovation (CFI), the Ontario Research Fund (ORF), Glacio-Ex, Carleton University, Climate and Cryosphere (CliC) Project, the Northern Scientific Training Program (NSTP), National Sciences and Engineering Research Council of Canada (NSERC), the Polar Continental Shelf Project (PCSP). Furthermore, organizations that provided imagery for this research: the Canadian Ice Service (CIS), Environment Canada.

I will be forever grateful to my supervisors Dr. Luke Copland and Dr. Derek Mueller for their guidance and especially their patience and to have provided me with the opportunity to study the massive and vulnerable ice shelves in the most beautiful place on Earth, the Canadian High Arctic. In addition, I would like to thank Dr. Derek Mueller, it is hard to put into words how much I am grateful, I could not have been able to go through this without you.

I would like to thank Adrienne White, Tyler de Jong, Andrew Hamilton and Nat Wilson for field work assistance and members of the Water & Ice Research Lab (WIRL) and Laboratory for Cryospheric Research. I would also like to thank Dave Burgess (Geological Survey of Canada), Bob Frederking (National Research Council of Canada), and Wayne Pollard (McGill University) for their advice on ice microstructure and the use of their equipment for the laboratory work.

Finally, I would like to thank my friends and family for their support and love. “Moman et Popa”, Jacqueline Richer and Roger McCallum, deserve special thanks for their constant support

and showing me the important things in life. They are the ones that inspired and taught me to follow my dreams and live life to the fullest. I would especially like to thank a wonderful man, a man I am proud to call grand-pa, and to whom I dedicate my master's thesis, John McCallum. My academic career would not have been possible without him. Unfortunately, he will not have had the chance to read my thesis, but deep down inside I know he is proud and would tell me "you're not just a pretty face".

## Table of contents

Abstract .....	ii
Acknowledgments .....	iii
List of Tables .....	vii
List of Illustrations .....	viii
List of Appendices .....	xiii
Chapter 1 Introduction .....	1
1.1. Thesis objectives .....	8
1.2. Thesis structure .....	9
Chapter 2 Literature Review .....	11
2.1. Ice texture and microstructure .....	11
2.2. Coastal ice types of Northern Ellesmere Island .....	13
2.2.1. Ice shelves .....	13
2.2.2. Epishelf lake ice .....	18
2.2.3 Other ice types on Northern Ellesmere Island .....	20
2.3 Texture and structure of the different ice types found across the Ellesmere ice shelves ....	21
2.4. Synthetic Aperture Radar (SAR) backscatter and ice .....	24
2.4.1. Principles of SAR .....	24
2.4.2. Microwave interaction (scattering) with the Earth's surface .....	30
2.4.3. SAR interactions with ice .....	32
Chapter 3 Methods .....	43
3.1 Study area .....	43
3.2. Fieldwork .....	45
3.3. Survey of surface conditions .....	49
3.4. Laboratory work .....	49
3.4.1. Sample preparation .....	49
3.4.2. Ice texture analysis .....	51
3.4.3. Remote Sensing/SAR backscatter analysis .....	52
3.4.4. Statistical analysis .....	53
Chapter 4 Results .....	57

4.1. Surface condition survey .....	57
4.2. Snow cover and ice surface .....	58
4.3. Ice structure .....	59
4.4. Salinity and temperature.....	62
4.5. Ice texture.....	63
4.6. Backscatter analysis .....	65
4.7. Relationship between SAR variables and ice properties.....	66
Chapter 5 Discussion .....	87
5.1. Ice identification.....	88
5.2. Radar signature of the ice and SAR visual interpretation .....	93
5.3. Relating radar return with ice properties.....	95
5.4. Ice shelf structure and origins .....	96
Chapter 6 Conclusions .....	103
Chapter 7 References .....	106
Appendix A.....	114
Appendix B.....	116

## List of Tables

<b>Table 2.1:</b> Compilation of bulk salinity and temperature data from different ice types from Northern Ellesmere Island. ....	41
<b>Table 2.2:</b> Compilation of the SAR backscatter (dB) in HH polarization of various ice types. ...	42
<b>Table 4.1:</b> Detail of ice cores extracted across the Milne Ice Shelf (MIS), the Milne epishelf lake (MEL), and Petersen Ice Shelf (PIS) in May 2013. Ice core B4 was extracted in May 2012. ....	83
<b>Table 4.2:</b> Descriptive statistics of the ice properties for each of the ice types sampled in this study. ....	84
<b>Table 4.3:</b> Descriptive statistics of the SAR backscatter (April 27, 2013) for each of the ice types sampled in this study. ....	85
<b>Table 4.4:</b> RADARSAT-2 incidence angle across each ice core location. ....	86

## List of Illustrations

**Figure 1.1:** A) Location of the study site on northern Ellesmere Island. B) NW coast of Ellesmere Island showing the last remaining Canadian ice shelves (as of summer 2014) and location of recently collapsed ice shelves (from left to right): former Serson Ice Shelf (SIS), Petersen Ice Shelf (PIS), Milne Ice Shelf (MIS), former Ayles Ice Shelf (FAIS), Ward Hunt Ice Shelf (WHIS), and former Markham Ice Shelf (FMHIS)..... 10

**Figure 2.1:** Representation of the crystal lattice of ice Ih. Spheres (red and white) represent oxygen and hydrogen atoms, respectively. Rods (grey) represent hydrogen bonds. The yellow dashed line symbolizes the hexagonal symmetry of the lattice (Faria et al., 2014b). The c-axis of the crystal is perpendicular to the plane shown here. .... 35

**Figure 2.2:** Interpretation of two distinct stratigraphic units found in part of the Ward Hunt Ice Shelf. This cross section was based on two ice cores (A, B) and laboratory analyses and shows alternating stratified basement ice (brackish ice) and old sea ice layers. After Lyons et al., 1971. .... 36

**Figure 2.3:** Backscatter of ice dammed lake ice and environmental change. A) RADARSAT-1 Wide Beam B Scan-SAR image of northernmost Ellesmere Island, February, 2002 (© CSA 2002). A bright SAR signature indicates the presence of an ice dammed lake (including epishelf lakes) (c.f., Jeffries. 2002; Veillette et al., 2008). B) RADARSAT-2 Wide Beam images, March, 2009 (©MDA 2009) with major remaining, and former ice shelves (from left to right): former Serson Ice Shelf (SIS), Petersen Ice Shelf (PIS), Milne Ice Shelf (MIS), former Ayles Ice Shelf (FAIS), Ward Hunt Ice Shelf (WHIS), and former Markham Ice Shelf (FMHIS). Areas of bright SAR return in 2002 appear darker with the exception of the Milne Fiord Epishelf Lake (green circle) which indicates the loss of the freshwater ice and the ice dammed lakes (Mueller et al., unpublished)..... 37

**Figure 2.4:** Different ice types found along the northern coast of Ellesmere Island. Stipple indicates ice rises and glaciers, a simple hatch (sh) indicates exposed basement ice (marine ice), solid grey indicates iced firn (meteoric ice) and cross hatch (ch) indicates floating glacier portions of ice shelves. A) Ward Hunt Ice Shelf, B) Serson Ice Shelf, C) Milne Ice Shelf, D) Ayles Ice Shelf, E) Markham Ice Shelf. After Mueller et al., 2006. .... 38

**Figure 2.5:** Examples of SAR backscatter (RADARSAT-2 wide beam mode (March, 5 2009), over different sea ice types. Multiyear Landfast Sea Ice (outlined in red) has a high backscatter due to low salinity and greater bubble concentration within the first meter below the surface, resulting in volume scattering. First year ice (outlined in blue) has a lower backscatter due to higher salinity concentration, resulting in the absorption of the radar (Pope et al., 2012). Stars show location of ice core extraction by Pope et al. (2012)..... 39

**Figure 2.6:** Examples of multiple SAR scattering mechanism across different surfaces. Smooth surfaces reflect the radiation away from the sensor without returning a signal, resulting in a dark tone. A rough surface yields surface scattering, resulting in a brighter toned image. Double bounce occurs when the radar interacts with two surfaces at right angles to each other, which enhances the amount of energy reflected back to the sensor. Volume scattering is the result of the radiation being transmitted across an interface and then interacting with inhomogeneities in a volume of material, resulting in a brighter toned image..... 40

**Figure 3.1:** A) Location of study site on northern Ellesmere Island, B) NW coast of Ellesmere Island showing location of the Milne and Petersen ice shelves. C) RADARSAT-2 image (wide beam mode, April 27, 2013) of the Milne and Petersen ice shelves showing the ice core extracted for each ice type. D-F) Snow covers across ice type A, B, and C, respectively, taken during the May 2013 fieldwork..... 55

**Figure 3.2:** Photograph of ice core thin section, under cross-polarized light, drilled in a ridge from the central unit of the Milne Ice Shelf providing supporting evidence of the texture of glacially fed shelf ice showing grains with even edges which do not interlock, gird lines 1 cm apart (Jeffries, 1985a). ..... 56

**Figure 4.1:** SAR transects showing the backscatter variability across the different ice types extracted from RADARSAT-2 fine-quad wide beam mode images acquired on April 17, 2012 (A & C) and April 27, 2013 (B & D), respectively. A,B) Milne Fiord transect; arrows indicate areas of higher backscatter (moraine, conical mounds, surface crevassing) across ice type Bm. C, D) Transect along the Petersen Ice Shelf..... 67

**Figure 4.2:** A) RADARSAT-2 image (fine quad wide beam mode, April 27, 2013) of the Milne Ice Shelf. Red: HH, Green: VV, Blue: HV. B) Photograph of the ice with a dark signature where presumably sea ice is filling a crack in the ice shelf (green square). C) Photograph of one of the numerous extensive cracks found across the ice shelf that has a bright SAR signature (yellow square). D) Photograph of a trough with a dark signature taken from the top of an adjacent ridge (blue square). E) Photograph of moraine material and conical mounds that have a bright SAR signature (pink square). F) Extensive surface fracturing that is associated with lineaments with a bright signature (orange square). G) A smooth ice surface with both a bright and dark SAR signature (red square). RADARSAT-2 image © MDA 2013. Images B-G were taken during the May 2013 fieldwork..... 68

**Figure 4.3:** Images of the ice surface A) Ice surface across the meteoric ice found on the outer section of the Milne Ice Shelf showing areas of rotten and broken surface. B) Ice surface across the Milne Epishelf Lake found on the inner section of the Milne Ice Shelf, showing the dark and solid surface. C) Ice surface across the Milne Epishelf Lake at core site CME3 showing the candle ice surface. Images A-C were taken during the May 2013 fieldwork..... 69

**Figure 4.4:** Ice structures viewed in the field in natural light. Ice type A had a cloudy appearance due to an abundance of tiny bubbles and rounded bubble clusters. Ice subtype Bm had a milky appearance and few bubbles, and ice subtype Bp had a milky appearance and elongated bubble structures. Ice type C was clear with long elongated bubbles. .... 70

**Figure 4.5:** Boxplot of the bubble dimensions by ice type. A) Horizontal size. B) Vertical size. C) Aspect ratio (horizontal/vertical). D) Bubble diameter. The Kruskal-Wallis test or ANOVA *p*-value is listed in each plot. .... 71

**Figure 4.6:** Typical bulk salinity profiles for each ice type (accuracy of  $\pm 0.1$  psu). A) Type A. B) Type Bm. C) Type Bp. D) Type C. Because ice type C did not have many salinity profiles taken all three cores were plotted into the one profile (each profile are recorded for each ice core extracted)..... 72

**Figure 4.7:** Bulk salinity profile for core B4 (ice type Bp) with break in the x-axis (Salinity (psu)) at high values..... 73

**Figure 4.8:** Internal ice core temperatures taken every  $\sim 15$  cm (accuracy  $\pm 0.5^\circ\text{C}$ ) during field measurements. A) Type A. B) Type Bm. C) Type Bp. D) Type C. .... 74

**Figure 4.9:** Typical ice texture for each ice type viewed in polarized light. Ice type A had homogeneous, medium-grained texture of equant-shaped grains (euhedral) and granular, with sharp edges and corners. Ice subtype Bm had an inhomogeneous, medium to coarse grain texture with subhedral grains, a granular and tabular shape, and rounding of the edges and corners of the grains (jigsaw pattern). Ice subtype Bp had an inhomogeneous grain texture varying from very fine to very coarse, with mixture of euhedral, subhedral and anhedral grain shape and had granular, tabular and columnar shapes. Ice type C at the surface had an inhomogeneous texture and was both euhedral and subhedral (top), while at the bottom of the core the ice was homogeneous and anhedral, due to the very large grain diameter..... 75

**Figure 4.10:** Grain diameters from laboratory measurements of prepared thin sections between cross-polarized light for each ice type. A) Type A. B) Type Bm. C) Type Bp. D) Type C. .... 76

**Figure 4.11:** Boxplot of the grain dimensions by ice type for horizontal (A-C) and vertical (D-F) sections. A, D) Length. B, E) Width. C, F) Aspect ratio (Length/Width). The Kruskal-Wallis test *p*-value is listed in each plot..... 77

**Figure 4.12:** Ice core segment 134-149 cm from core B3 showing possible evidence of glacier ice texture (Red Circle). However a bulk salinity of 0.94 psu and rounding of the grains implies it is old sea ice (Jeffries et al., 1989)..... 78

**Figure 4.13:** Histogram of the backscatter by ice type. A-C)  $\sigma^{\circ}_{HH}$ ,  $\sigma^{\circ}_{VV}$ , and  $\sigma^{\circ}_{HV}$ , respectively. Type A (pink), type B (green) and type C (cyan) overlap as follows: both type A & B (dark green), both type A & C (purple), overlap of all ice types (dark blue). ..... 79

**Figure 4.14:** Boxplot of the different polarization and polarization ratio according to each ice type. A-C)  $\sigma^{\circ}_{HH}$ ,  $\sigma^{\circ}_{VV}$ , and  $\sigma^{\circ}_{HV}$ , respectively D-F) Co-pol ratio, cross-pol ratio (HV/HH), and cross-pol ratio (HV/VV), respectively. The *p*-value from the Kruskal-Wallis Test indicating if each data set is drawn from the same population. .... 80

**Figure 4.15:** Relationship between SAR and bubble variables. A) HH backscatter vs bubble diameter. B) VV backscatter vs bubble diameter. C) Co-pol ratio vs bubble concentration. D) Cross-pol ratio (HV/HH) vs bubble diameter. The Spearman *r* and *p*-value are listed in each scatterplot and a line of best fit is provided. .... 81

**Figure 4.16:** Relationship between SAR and grain variables. A) Cross-pol ratio (HV/HH) vs grain length from vertical thin sections. B) Cross-pol ratio (HV/HH) vs grain diameter from vertical thin sections. C) Cross-pol ratio (HV/VV) vs grain diameter from horizontal thin sections. D) Cross-pol ratio (HH/VV) vs grain aspect ratio from horizontal thin sections. The Spearman *r* and *p*-value are listed in each scatterplot and a line of best fit is provided. .... 82

**Figure 5.1:** A1) The structure and texture of ice type A, both in natural and polarized light, consisting of meteoric ice, or iced firm, bottom. A2) Sng evidence of the of the meteoric ice structure and texture (Ragle et al., 1964). B1) The texture, in polarized light, of ice type B, from the Milne Ice Shelf (Bm) consisting of brackish and sea ice (marine ice). B2) Supporting evidence of the texture of marine ice (Far left and middle: brackish ice (Jeffries et al., 1989) and far right: FY sea ice (Tucker et al., 1984)). C1) he texture, in polarized light, of ice type B, from the Petersen Ice Shelf (Bp) providing of old sea ice (marine ice). C2) Supporting evidence of the texture of old sea ice (marine ice) (Jeffries et al., 1989). D1) The texture, in polarized light, of ice type C consisting of congelation epishelf lake ice.D2) Supporting evidence of the texture of congelation ice (Alaska Satellite Facility, 2014). ..... 99

**Figure 5.2:** The frequency distribution of salinity values in brackish ice and sea ice extracted from the Ward Hunt Ice Shelf, showing that 75% of the brackish ice samples were found in the 0-0.25 psu category, while sea ice occupied all 9 classes, with only 5% in the 0-0.25 psu category. After Jeffries et al. (1989). ..... 100

**Figure 5.3:** Basal power reflection coefficient (PRC) interpretation across the Milne Ice Shelf where regions less than -30 dB implies the possible presence of brackish ice. After Narod et al. (1988). ..... 101

**Figure 5.4:** Ice surface showing the debris rich surface across the central Milne Ice Shelf from June, 2012 (Photo taken by helicopter courtesy of Andrew Hamilton)..... 102

## List of Appendices

<b>Appendix A1:</b> Ice structure legend for Figure A2 .....	114
<b>Appendix A2:</b> Visual structure of each ice core extracted from each ice type. See Figure A1 for legend.....	115
<b>Appendix B1:</b> Results of the surface analysis .....	116
<b>Appendix B2:</b> Ice structure, temperature and bulk salinity data. For the fracture and dirt variables 0=no presence, 1=presence, and the bubble concentration are rated 1-4 (1=low, 4=very high) (NA meaning no data available).....	117
<b>Appendix B3:</b> Measurements of individual bubbles from the structural analysis.....	121
<b>Appendix B4:</b> Ice grain dimensions.....	126

## Chapter 1 Introduction

Canada's landmass extends as far north as 83°N, which is some of the most northerly land in the world (Van Wijngaarden, 2014). Over the period 1880-2012, average global surface temperature has increased by 0.85°C (IPCC, 2013). This warming has not been uniform over the Earth's surface and particularly rapid increases, up to twice the global rate, have been observed in the Arctic (Serreze and Barry, 2011). For example, Van Wijngaarden (2014) reported that temperature increases as large as 5°C occurred in the western Canadian Arctic over the period 1954-2003. Furthermore, they found that temperatures increased by 0.28°C decade<sup>-1</sup> at Alert station, Ellesmere Island, from 1947-2014. The largest temperature changes have been found during the winter and spring, while the smallest have been in autumn (Anisimov et al., 2007; Derksen et al., 2012; Van Wijngaarden, 2014).

This rapid atmospheric warming has had a pronounced effect on the cryosphere. For example, September Arctic sea ice extent has declined at an average rate of 13% per decade since 1979 and the Arctic Ocean has been projected to become nearly ice-free during the summer within this century (Stroeve et al., 2012; Parkinson, 2014; IPCC, 2013). There has been enhanced mass loss of the Greenland Ice Sheet over the past 20 years, with these losses providing one of the largest current contributions to global sea-level rise, accounting for 0.5 mm yr<sup>-1</sup> of a total of 3.2 mm yr<sup>-1</sup> (Hanna et al., 2008; Khan et al., 2014). Permafrost temperatures in Canada have also increased between 0.5 to 2°C since the late 1970s (Derksen et al., 2012; IPCC, 2013). On Ellesmere Island, along

Canada's northernmost coastline, recent changes include a switch from perennial to annual lake ice cover in coastal lakes (Mueller et al., 2008), the break-up and loss of multi-year landfast sea ice (MLSI) (Pope et al., 2012) as well as the thinning and recent break-up of the last remaining Canadian ice shelves (Mortimer et al., 2012; Copland et al., 2007; Mueller et al., 2008, White et al., 2015).

Satellite remote sensing has provided a valuable tool to assess the impacts of atmospheric warming in the Arctic. This is helped by the fact that most scientific satellites are polar-orbiting, with the convergence of orbits at high latitude often providing frequent repeat coverage of up to several times per day (e.g., MODIS optical satellite imagery; Copland et al., 2007). The use of high resolution optical imagery has been employed to measure glacier area changes (Berthier et al., 2005), gravity data from satellites can be used to monitor changes in glacier mass (Velicogna, 2014), and laser altimeters can measure changes in the thickness of glaciers and sea ice (Connor et al., 2009). In addition, monitoring of the dramatic reduction in sea ice extent has been conducted using passive microwave data (Comiso et al., 2008; Polyak et al. 2010). The loss of Canada's ice shelves along the northern coast of Ellesmere Island has been followed closely using active microwave sensors on satellites such as ERS-1 and ERS-2, JERS, ENVISAT, as well as RADARSAT-1 and RADARSAT -2 (Copland et al, 2007; Mueller et al., 2008; Mortimer et al., 2012; White et al., 2015, Jeffries 2002). This technology, known as Synthetic Aperture Radar (SAR), can image ice through clouds and during the polar night (Scheuchl et al., 2005). RADARSAT imagery is widely used by the Canadian Ice Service (CIS), for classifying and delineating sea ice characteristics (e.g., presence of sea ice,

concentration, stage of development and form) to produce navigational ice charts and monitor sea ice changes over time. The CIS relies primarily on manual image interpretation to fulfil its mandate, which is to provide the most precise and up-to-date information on ice in the navigable waters of Canada. In turn this contributes to the planning of safe shipping routes, supports offshore resource exploration in the North, and helps to establish Arctic sovereignty.

Recent novel applications of satellite SAR data include the detection of changes in ice type, in addition to the traditional monitoring of ice break-up and losses. For example, White et al (in revision) examined ice types across and around the Petersen Ice Shelf using a backscatter analysis of SAR imagery. This indicated that freshwater ice occurred at the rear of the ice shelf for at least 12 years (1992-2004), formed from a layer of freshwater floating over the ocean that was held in place by the ice shelf. This freshwater ice was replaced by sea ice following a break-up and drainage of this ice-dammed lake in 2005. Other similar research illustrates how the loss of these unique cryospheric environments, caused by environmental change, can have profound implications for aquatic species that depend on them. (Mueller et al., 2003 & 2006). For example, the losses of freshwater habitat (epishelf lake) in northern Ellesmere Island, that are known to support unique biological communities, has resulted in the loss of rare ice-dependent habitats in the Northern Hemisphere (Mueller et al., 2003)

In this period of rapid environmental change, more data is required to better understand the physical processes that are underway. However, fieldwork in these remote areas

remains costly and logistically demanding, and is typically unable to provide the regional perspective required. Remote sensing therefore provides a promising method to gather more data on environmental change in the Arctic, but this requires the improvement of existing measurement techniques and the development of new ones. The focus of this study concerns the interpretation and classification of ice types along northern Ellesmere Island using backscatter analysis from SAR imagery. Grenfell et al. (1998) argue that to properly identify and interpret various ice types through the observation of satellite imagery, it is important to understand their electromagnetic (EM) signature. It is therefore necessary to develop a quantitative description of the physical ice properties (ice texture and structure) and link them to satellite observations so that ice type classification and delineation can proceed with an understanding of what can influence the interaction of the EM radiation.

Several unique ice types exist along the northern coast of Ellesmere Island. These include ice shelves, which are formed by the seaward extension of glaciers and *in situ* accretion of basal and meteoric ice (Jeffries, 2002). These ice types have been characterized and differentiated with salinity and stable isotopic measurements as well as texture analysis from samples from the Ward Hunt Ice Shelf (WHIS) and Ward Hunt Ice Rise (WHIR) (Marshall 1955, 1960; Ragle et al., 1964; Jeffries & Sackinger, 1989). Sea ice and glaciers, as well as the perennial freshwater ice cover in lakes, are also found along this coastline. Some of these lakes are formed in fiords and bays from a layer of fresh, low density meltwater that floats on the ocean and remains impounded between the coast and thick ice further offshore (White et al. 2014; Mueller et al. 2003). Systems of this type are

referred to as shallow ice-dammed lakes if they are retained by multiyear ice and as deep ice-dammed or epishelf lakes if they are retained by ice shelves (Veillette et al., 2008). Both these lake types are perennially ice covered, which prevents wind mixing of the adjacent water column which maintains its stratification (Veillette et al., 2008).

Much of the previous work on SAR classification of ice types relates to sea ice measurements, monitoring, and identification (Barber & LeDrew, 1991). Various approaches have been used including radar signature (backscatter) analysis (Onstott, 1992; Haverkamp et al. 1993; Dierking et al. 1994; Grenfell et al. 1998, Veillette et al. 2008, Johnston and Timco 2008, Shokr 2009, Pope et al. 2012, White et al., 2015), tonal and texture analysis (Barber & LeDrew, 1991; Clausi, 2001), polarimetric analysis (Scheuchl et al. 2005), and other techniques that have been developed to combine multiple SAR variables into ice classifiers (Deng & Clausi, 2005).

These studies show that the total backscatter for sea ice arises from a combination of surface reflection (including specular reflection), volume scattering, and dihedral (double-bounce) scattering (Scheuchl et al. 2005; Barber & LeDrew, 1991; Deng & Clausi, 2005). The backscatter from each sea ice type is relatively distinguishable due to its pattern of surface roughness, as well as its dielectric constant (Onstott & Shuchman, 2004). Backscatter from first-year ice (FYI) is dominated by surface scattering. When FYI is smooth, it appears dark due to its relatively high salinity and high dielectric constant, which prevents the penetration of the radar (Scheuchl et al. 2005; Deng & Clausi, 2005). When the surface of FYI is rough, the ice appears brighter due to the

uneven surface causing scattering in many directions (Deng & Clausi, 2005). For multiyear ice (MYI) volume scattering dominates, due to the greater penetration of microwaves that comes with lower dielectric content in this relatively less saline ice type. This volume scattering is caused by an abundance of bubbles and sediments and makes the ice appear relatively brighter in SAR imagery than other sea ice types (Scheuchl et al. 2005; Deng & Clausi, 2005). High backscatter can also be due to dihedral reflection in areas where ice is ridged (Arkett et al., 2005).

Most of these previous studies relied on the filtering of SAR imagery, micro-scale modeling with macro-scale digital image classification, and algorithms for validation. However, although these studies show promising results, they cannot distinguish between all sea ice types due to difficulty in determining the ice-water boundary signatures under certain ice and environmental conditions (Arkett et al., 2005, Scheuchl et al. 2005). However, a useful finding from these studies is that dual polarization (HH/HV) mode, from RADARSAT-2 sensors, enhances the ability to extract sea ice information.

Some studies have examined the unique ice types that are found along the coast of Northern Ellesmere Island using remote sensing (Jeffries 1986, 1990(a, b), 1991; Dierking, 1994; Mueller et al, 2006; Veillette et al., 2008; Pope et al., 2012). However, not all these studies were validated by ice samples, and studies that did extract ice samples (Pope et al., 2012; White et al., 2015) did not statistically validate the return according to the ice type properties. Furthermore, most of the backscatter databases that are currently in use were compiled using early observations of backscatter from training

areas of hybrid ice types. For instance, a lookup table for sea ice classification created by Onstott (1992) was based on ERS-1 (European Space Agency's Remote Sensing Satellite), and JERS-1 (Japanese Earth Resources Satellite), and the NASA Earth Observing System satellite (EOS). Veillette et al. (2008) compiled information with RADARSAT-1 on only epishelf lake ice, which was then updated by White et al. (2015) with RADARSAT-2. Pope et al. (2012) used RADARSAT-2 imagery, though only compiled radar returns from first year sea ice and MLSI. All of the above mentioned studies have used only co-polarized SAR (C band HH polarization for RADARSAT-1 and -2; C band VV polarization at an incidence angle of  $23^\circ$  for ERS-1 and -2; L band HH polarization at an incidence angle of  $35^\circ$  for JERS-1; and X band HH polarization at  $25^\circ$  for EOS).

This research will examine ice types in two locations, Milne Fiord and Petersen Bay (Figure 1.1), which have had little (Jeffries 1985) to no formal ice type characterization, particularly at the microstructural level. This study will provide an updated backscatter database using RADARSAT-2 imagery from training areas of various ice types that have been sampled. It will examine the relationship between ice physical properties and SAR backscatter, which will improve the ability for future researchers to discriminate between ice types. This research may offer the potential to improve the ability to assess seasonal, interannual, and long-term changes (past and future) of the Ellesmere Island ice cover. Finally, this project may assist the CIS in their routine surveillance of floating ice in the entire Canadian Arctic region. An enhanced understanding of some of the unique ice

types of Ellesmere Island will assist in the production of more accurate ice charts and facilitate monitoring efforts.

### **1.1. Thesis objectives**

The aim of this study is to relate ice types of the northern coast of Ellesmere Island (82°30'N, 81°00'W) to backscatter obtained from RADARSAT-2 SAR imagery. This will be accomplished by characterizing ice types, determined *a priori*, using field and laboratory methods. Field work includes measuring snow depth, bulk salinity and temperature and the laboratory work consists of microstructural analysis of the ice covers by viewing thin sections under cross polarized light. SAR backscatter values taken from images acquired close to the sampling period were examined to explore the relationship between backscatter and geophysical measurements using qualitative and quantitative approaches.

To this end, this study has three main objectives:

- 1) To characterize the radar return (microwave backscatter) of the different ice types across the Milne and Petersen ice shelves, northern Ellesmere Island
- 2) To characterize the geophysical nature of these different ice types
- 3) To examine the relationship between the geophysics and backscatter in a qualitative and quantitative way and explore to what extent the ice type are distinguishable in SAR satellite imagery.

## **1.2. Thesis structure**

This thesis is presented in the traditional format: **Chapter 2** (Literature Review) outlines past research in the areas of ice texture, with a particular focus on the difference ice types found across the Ellesmere ice shelves, as well as SAR backscatter interactions with ice and past research on radar return and ice. **Chapter 3** (Methods) presents a detailed description of the methods and field/laboratory techniques employed for this study. **Chapter 4** (Results) describes the results of the study. **Chapter 5** (Discussion) presents an in-depth explanation of the results presented and **Chapter 6** (Conclusion) provides conclusions that may be drawn from this evidence. This is followed by References and Appendices.

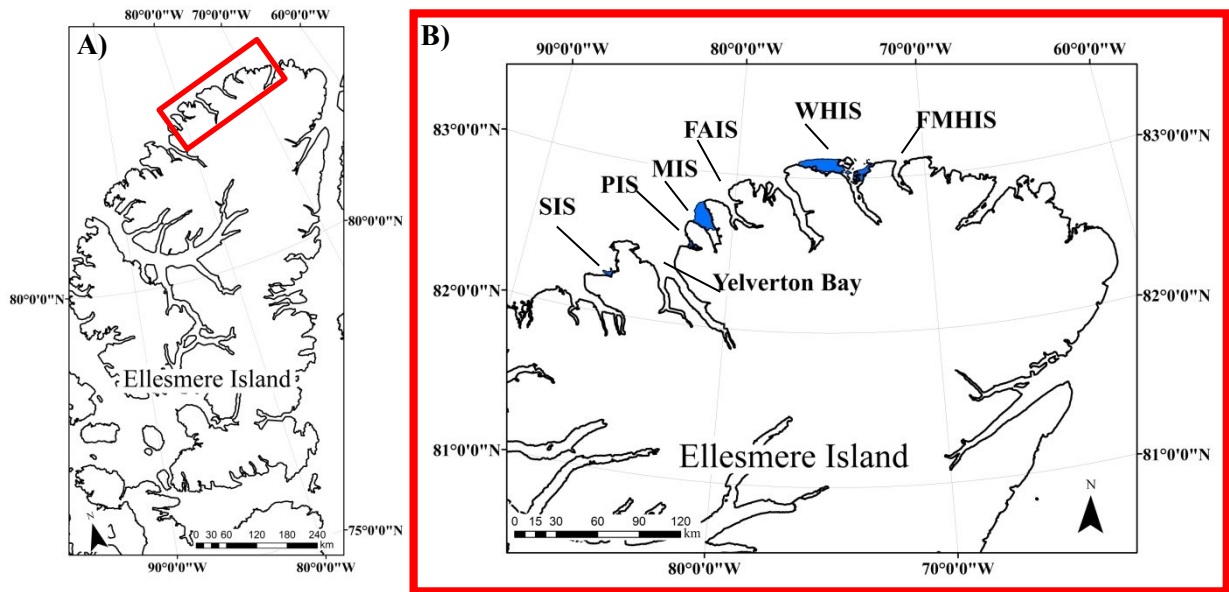


**Figure 1.1:** A) Location of the study site on northern Ellesmere Island. B) NW coast of Ellesmere Island showing the last remaining Canadian ice shelves (as of summer 2014) and location of recently collapsed ice shelves (from left to right): former Serson Ice Shelf (SIS), Petersen Ice Shelf (PIS), Milne Ice Shelf (MIS), former Ayles Ice Shelf (FAIS), Ward Hunt Ice Shelf (WHIS), and former Markham Ice Shelf (FMHIS).

## Chapter 2 Literature Review

### 2.1. Ice texture and microstructure

Together the Antarctic and Greenland ice sheets currently cover ~10% of the Earth's land area, while sea ice covers ~10% of the ocean surface seasonally (Schulson, 1999). If the entire Antarctic ice sheet were to melt it would raise global sea levels by 58.3 m, while the Greenland ice sheet would raise sea levels by 7.4 m (IPCC, 2013). Ice is a very important factor in global climate and can be used to reconstruct paleoclimates. The study of ice cores can provide climatic and biogeochemical information such as past temperature variations (revealed through isotopic data), atmospheric composition and circulation (through gas trapped in bubbles and impurity concentrations), and ice flow (through the analysis of ice texture) (Jouzel et al., 1987; Petit et al., 1999; Lüthi et al., 2008; Abram et al., 2013). Ice Ih (termed ordinary ice), under natural conditions on the Earth's surface, occurs in an ordinary hexagonal form and is a polycrystalline material (composed of many crystallites of varying size and orientation) (Schulson, 1999; Faria et al., 2014b) (Figure 2.1). The oxygen atoms in ice occupy points on a hexagonal lattice, which are strongly bonded to two hydrogen atoms, where each H<sub>2</sub>O molecule has four nearest neighbors at the points of a tetrahedron. Because ice Ih has a relatively open lattice, with a packing factor <34%, it is less dense than water (Schulson, 1999; Faria et al., 2014b). The microstructural characteristics of glacial ice can vary widely and depend on the conditions of their formation, the environmental and stress conditions that they experience, time/depth of burial, impurity content, as well as their thermal and deformation history (Cole, 2001; Azuma & Higashi, 1985; Alley, 1988; Budd & Jacka, 1989).

The *texture* of ice refers to the size, shape and arrangement of an assemblage of ice grains (or ice crystals) (Gow, 1986; Wilen et al. 2003). Ice texture is generally characterized as the average grain diameter in a sample, as well as the average elongation factor and/or the distribution of the elongations of the grains in an assemblage (Wilen et al., 2003). When all grains in a given sample are similar in size, the ice is termed equigranular. Seriate ice refers to a range of grain diameter for the majority of the primary crystals and porphyritic indicates there are two distinct grain diameters. Ice grain diameter classes include very coarse (>30 mm), coarse (15-30 mm), medium (5-15 mm), fine (1-5 mm) and very fine (<1 mm) (Ragle et al., 1964). The mean grain diameter typically increases with depth (age) in a glacier or ice sheet (Obbard, 2006). This is driven by the decrease in free energy caused by the reduction in grain boundary area (Obbard, 2006).

Typical terms used to describe ice grain shape include euhedral, subhedral, and anhedral as well as granular, columnar, and tabular (Ragle et al., 1964). Euhedral grains have sharp, well-formed faces and display ideal crystal morphology (hexagonal shape with all axes of the same length) which usually imply an homogeneous texture. Anhedral grains lack well-formed faces and have an amorphous shape, whereas subhedral grains lack smooth faces but still display an ideal crystal morphology both latter implying an inhomogeneous texture. A grain that has a granular shape will refer to crystals that are equally developed in all directions. Columnar shape refers to crystals that are developed preferentially in one direction and tabular refers to oblate crystals, which are preferentially developed in two directions (Challinor, 1973)

The fabric of ice refers to the distribution and orientation of the c-axis (vertically oriented crystal axis) of the ice polycrystal (Wilén et al., 2003; Durand et al., 2006). The structure of ice refers to impurities found within it such as bubbles, sediment layers, brine pockets, and fractures (Ragle et al., 1964). Bubbles are the most common structure found in ice cores, and according to Ragle et al (1964) the bubble shape, composition, pressure and frequency should be distinct and genetically related to the ice in which they form.

Note that the terminology used for the description of ice above and elsewhere in this thesis can vary, and that there is no single universally accepted set of standards. Other usages of these terms can therefore be found elsewhere in the literature.

## **2.2. Coastal ice types of Northern Ellesmere Island**

### **2.2.1. Ice shelves**

Ice shelves are composed of thick (>20 m) floating landfast sea ice and glacier tongues (Jeffries 2002; Lemmen et al., 1988b; Mueller et al., 2006). They are formed as a result of the seaward extension of glaciers, the *in situ* vertical accretion of ice to the bottom (sea ice freeze-on) or top (snow accumulation and firnification) of the ice shelf, the horizontal accretion of multiyear landfast sea ice (MLSI), or a combination of these processes (Mueller et al., 2006; Veillette et al., 2008). Ice shelves lose their mass via surface and basal melt, and by calving, which produces ice islands (Jeffries, 2002). In the Northern Hemisphere, ice shelves are only found along northern Ellesmere Island, Greenland,

Novaya Zemlya and Franz Josef Land in the Russian High Arctic (Dowdeswell et al., 1994). In contrast, in the Antarctic, they comprise ~47% of the coastline (Andrew, 1999).

The ice shelves of northern Ellesmere Island covered an area of ~563 km<sup>2</sup> in 2011 (Kealey et al., 2011). The Ellesmere ice shelves that are present today (Figure 1.1) appear to be late Holocene in age and are not relics of the last glaciation (Jeffries, 1992). With the use of driftwood radiocarbon dating, the formation of the present Ellesmere ice shelves has been dated to ~4000 to 5500 years B.P. (England et al. 2008). They were first described by Lieutenant Pelham Aldrich (Royal Navy) and Commander Robert Peary (U.S. Navy), who traveled along the coast in 1876 and 1906, as “*ridges and rollers, composed of ice under the snow and a series of rolling swells featured in this ice-foot*” (Peary, 1907).

Over the past decade, the ice shelves have undergone dramatic changes along the coastline of northern Ellesmere Island. In August 2005, there was the complete loss of the Ayles Ice Shelf (Copland et al., 2007), the complete loss of the Markham Ice Shelf in summer 2008 (Mueller et al., 2008), and a 90% loss of the area of the Serson Ice Shelf between 2008-2011 (Mueller et al., 2008; Kealey et al., 2011). Furthermore, the WHIS lost 32% of its area between 2000 and 2012 (Mueller et al., 2003; Mueller et al., 2008; Kealey et al., 2011, Copland et al., in revision), and the Petersen Ice Shelf lost 53% of its extent between 2005-2012 (Pope et al., 2012; White et al., 2015).

In addition to ice shelf changes, there have also been observations of the breakup of semi-permanent multi-year landfast sea ice (MLSI) along northern Ellesmere Island, which previously acted as a protective barrier for the ice shelves (Pope et al., 2012). Once this MLSI breaks away, it leaves the ice shelves exposed to ocean waves, collisions with mobile sea ice fragments, and offshore winds (Copland et al., 2007 & in revision). Previous studies have illustrated the connection between open water events and the breakup of the Ellesmere ice shelves. Such an example was the loss of the Ayles Ice Shelf in August 2005 after a 2 week period of open water in front of it (Copland et al., 2007). Prior to the Ayles Ice Shelf breakup, extensive open water increased to a width of ~10 km followed by the loss of MLSI in front of the Ayles and Milne ice shelves. MLSI is considered to be a physical barrier holding ice shelves in place and protecting them from wave impacts and thermal or mechanical erosion. After the loss of the protective barrier, fractures developed across the back of the Ayles Ice Shelf and, shortly after, the ice shelf calved away completely.

A number of studies have made measurements of the ice shelf thicknesses across the Ellesmere Island coastline. They are thought to be approximately 40 m thick on average (Jeffries, 2002), although thicknesses of >100 m have been measured at the fronts of tributary glaciers which feed into some ice shelves such as the Milne (Narod et al., 1988; Mortimer et al., 2012). The Petersen Ice Shelf was 29 m thick on average in 2011 (White et al., 2015) and the Milne Ice Shelf was 55 m thick on average in 2009 (Mortimer et al., 2012). The WHIS was 25-60 m thick (Braun et al., 2004) and the Ayles Ice Island was 45

m thick at a single point a year following its break away from Ayles Fiord (Copland et al., 2007).

There are several ways in which an Ellesmere Island ice shelf can be formed. According to several previous studies (Koenig et al., 1952; Jeffries et al., 1985; and Jeffries et al., 1991) there are two primary mechanisms:

1. The seaward extension of grounded glaciers, which form glacier tongues
2. The growth of thick sea ice, which forms landfast sea ice

Two genetic terms were proposed by Lemmen et al. (1988a) to describe ice shelves formed by these primary mechanisms: “glacial shelf ice” and “sea-ice ice shelf”. The term “composite ice shelf” is then used for parts of an ice shelf that originate by both of these primary mechanisms (Lemmen et al., 1988b). Once initially formed, secondary growth mechanisms for the ice shelves occur from accumulation of snow on their surface (iced firn) and basal accretion of brackish and sea ice (Jeffries 1987; Jeffries et al., 1991).

Jeffries et al. (1991) noted that with these multiple formation processes, the Ellesmere ice shelves can have a complex stratigraphy comprised of many different ice types. These different ice types will result in different physical properties and structural characteristics which reflect different initial growth processes and conditions (Jeffries et al., 1991). Due to these multiple formation processes, several studies have divided the Ellesmere ice shelf ice into two different stratigraphic units (Figure 2.2). These units are typically an

upper meteoric ice (iced firn) layer and a lower marine ice (basement ice) layer (Lyons et al., 1971; Jeffries, 1992; Mueller et al., 2006). However, either of these ice types may be found at the surface of the ice shelf depending on the local ablation and accumulation history.

The term iced firn is specific to the Ellesmere ice shelves, and describes the result of the rapid transformation of snow to ice by the percolation of melt water and refreezing during the course of a summer (Marshall, 1955, 1960; Jeffries et al., 1991; Jeffries, 1992; Mueller et al., 2006). They also consist of lake ice, from water melting and ponding in troughs on the ice shelf surface. Basement ice refers to old sea ice or brackish ice which accreted on the underside of the ice shelf, or MLSI (Lyons et al., 1971; Jeffries, 1992; Mueller et al., 2006). These ice types are often found to be stratified (with each other or other ice types, such as refrozen lake ice and iced firn; Lyons et al., 1971). Basement ice can be found at the surface of an ice shelf following long-term surface ablation which removes the overlying iced firn (over a period of ~400-500 years; Jeffries et al., 1988) (Figure 2.3). Stratified basement ice composed mainly of old sea ice has a typical salinity of 1.25 psu (practical salinity units, equivalent to ‰) whereas stratified brackish basement ice is an order of magnitude less saline (0.13-0.19 psu, depending on the depth) (Lyons et al., 1971). Iced firn and lake ice, consists of freshwater and has a very low salinity (<0.01 psu) (Table 2.1).

### **2.2.2. Epishelf lake ice**

Epishelf lakes occur where ice shelves block the mouth of fiords and embayments, retaining a layer of freshwater over marine water below (Jungblut et al., in press). This freshwater originates in the summer when meltwater from ice and snow in the drainage basin behind the ice shelf flows towards the fiord and becomes dammed behind an ice shelf. Measurements at the mouth of Disraeli Fiord of extremely negative  $\delta^{18}\text{O}$  values and high levels of tritium explained how snow-meltwater run-off from the surrounding land was the main contributor to the freshwater surface layer of epishelf lakes (Jeffries, 1985a, 1991). An epishelf lake is covered by thick perennial lake ice, which prevents the freshwater from being mixed by wind, thereby maintaining its stratified structure (White et al., 2015). However, if the ice shelf dam fails and/or the freshwater is subjected to wind mixing it would no longer maintain its stratified structure (Jeffries, 2002).

Epishelf lakes are found both in Antarctica (Gibson & Anderson, 2002) and northern Ellesmere Island (i.e., Ludlam, 1996; Van Hove et al., 2001; Jeffries, 2002; Mueller et al., 2006; Veillette et al., 2008; Mueller et al., 2009). They were first discovered in the early 1950s in Antarctica as a series of fresh, tidal lakes located between rocky, ice-free areas and floating ice shelves, often located many tens of kilometers away from open marine water (Gibson & Andersen, 2002). These lakes have drawn the attention of many researchers due to their unique ecology and because they are a strong indicator of climate change (Vincent et al., 2001; Gibson & Andersen, 2002). There have been two types of epishelf lake identified in Antarctica, compared to the one type described for the Arctic. Similar to the Arctic, a freshwater layer can float above saline marine water and the depth

of the lake is controlled by the thickness of the ice shelf (Wand et al., 1988; Vincent et al., 2001). A second type, which has not been described in the Arctic, is described by Gibson & Andersen (2002) as having an indirect hydraulic connection with the marine environment, presumed to occur at the land-ice contact, or through cracks in the ice shelf.

Epishelf lake ice has a coarse or very coarse texture with large columnar grains and dense bubble concentration (spherical, elongated, and tabular) (Jeffries et al., 1991). The perennial ice cover is usually characterized by a candled surface resulting from partial melting during the summer, causing strong surface scattering in synthetic aperture radar (SAR) satellite imagery. It also contains many internal melt features (Jeffries, 2002) which cause strong volume scattering in SAR imagery (Jeffries et al., 2013).

Epishelf lakes are strongly dependent on the presence of ice (Mueller et al., 2009) and have been changing rapidly following the atmospheric warming in recent decades and the associated retreat and collapse of ice shelves, both in the Arctic and Antarctic. Changes and losses in epishelf lakes have thus been used as an indicator of ice shelf loss in several studies (e.g., Vincent et al, 2001; Mueller et al., 2003, Smith et al., 2006; White et al., in revision). For example, the epishelf lake found in Disraeli Fiord, northern Ellesmere Island, experienced a decrease in freshwater layer thickness between 1967 and 1999. This was associated with the climate-induced thinning of the adjacent WHIS (Vincent et al., 2001) and major fracturing allowed for the drainage of the lake in 2000-2002 (Mueller et al., 2003).

In SAR imagery, epishelf lake ice has a bright signature due to volume scattering interacting with the ice volume (Jeffries, 2002). For example, in 2000 there were several bright SAR signatures found in fiords and inlets of the north coast of Ellesmere Island that were indicative of perennial lake ice (Figure 2.4A; West Arm Yelverton Inlet, Ayles Fiord, Taconite Inlet, and M'Clintock Inlet). When comparing a 2000 SAR image with one from 2009 (Figure 2.4B), many areas in fiords and bays where there was a bright SAR signature (epishelf lake ice) changed to a darker SAR signature, indicating that the freshwater had been replaced by seawater or brackish water (Jeffries, 2002; Veillette et al., 2008).

### **2.2.3 Other ice types on Northern Ellesmere Island**

#### ***2.2.3.1. Ice rises***

An ice rise is considered to be a non-floating ice feature formed by the grounding of an ice shelf on subjacent land (Lyons et al., 1972). An example of this is the Ward Hunt Ice Rise (WHIR) (Figure 2.3) which measures between 40-100 meters in thickness and was formed around 250-350 years ago when the WHIS thickened and grounded due to the isostatic uplift of the seafloor by 1.5 m north of Ward Hunt Island (Lyons et al., 1972; Braun et al., 2004). The WHIR is composed of iced firn and interstratified lake ice at the surface (to a depth of ~25-33 m), which overlie sea ice (Lyons et al., 1972). Other ice rises that surround the WHIS, Camp Creek and Discovery ice rises (Lyons et al., 1972), are comprised of iced firn almost to their bases.

### ***2.2.3.2. Sea ice***

Sea ice is frozen ocean water that forms, grows, and melts in the ocean (Weeks & Hibler, 2010). Since it forms from freezing of ocean water, sea ice has a relatively high bulk salinity which differentiates it from icebergs, glaciers, and lake ice. Sea ice typically grows during the fall and winter months and melts during the summer months. If sea ice does not survive a summer melt season then it is called first year ice (FYI). However, if the ice remains throughout the summer melt season it is classified as multiyear ice (MYI) (Johnston and Timco, 2008). When sea ice fringes a coastline it is referred to as landfast ice and should this survive more than one summer melt, it becomes multiyear landfast sea ice (MLSI). MLSI becomes a protective barrier for ice shelves because it physically holds the shelves in place, protecting them from wave impacts and associated thermal and mechanical erosion (Copland et al., 2007).

## **2.3 Texture and structure of the different ice types found across the Ellesmere ice shelves**

Since the Ellesmere ice shelves are created via a variety of growth mechanisms they typically have a complex stratigraphy and are usually comprised of several different ice types such as iced firn, sea ice, glacier ice, and lake ice (Koenig et al., 1952; Ragle et al., 1964; Jeffries et al., 1987; Lemmen et al., 1988a; Lemmen et al., 1988b; Jeffries et al., 1991). Each different ice type reflects its unique growth process and condition due to its particular physical properties and structural characteristics (Jeffries et al., 1991)

Several previous studies have documented the texture and structure of iced firn (Marshall, 1955, 1960; Koerner, 1968; Koerner, 1970; Jeffries et al., 1990). In addition to

the term “iced firn”, this ice type can also be referred to by other terms including “glacier ice”, which refers to the ice accumulated at the surface during periods of positive mass balance (Ragle et al., 1964), and “depositional ice”, which includes iced firn and superimposed ice (water percolating through the snow or firn directly and freezing at the ice surface) (Koerner, 1968). Iced firn is an ice type that is cloudy in appearance (due to the presence of many small bubbles), with generally medium grains (5-15 mm) and granular texture, although it can range from fine to coarse grained (Ragle et al., 1964). Ragle et al (1964) mentioned that a criterion for identifying “glacier ice” is its generally medium grained texture, equidimensional grains when viewed in thin section, and the occurrence of a large number of bubbles which are primarily spherical in shape. This was also confirmed by Jeffries et al. (1991), who referred to iced firn as having a medium size (5-10 mm) granular texture with a random c-axis orientation. Jeffries et al. (1991) also showed that there are two types of bubbles that occur, which are always found together: spherical bubbles which are typically around 0.1-1 mm in size (but occasionally up to 3 mm diameter), along with slightly elongated bubbles 2-3 mm long. There is also evidence of stratification throughout iced firn cores of thick (60 mm), relatively clear ice sandwiched between thin bubbly ice layers, as well as a few thin (5-30 mm) layers of very bubbly (low-density) ice which resembles firn (Ragle et al., 1964).

Ragle et al., (1964) cored lake ice from troughs on the WHIS, formed when summer meltwater freezes. They described that lake ice is easily recognized due to its medium (5-15 mm) to very coarse (> 30 mm) grain texture and long columnar grains with straight grain boundaries as well as long, linear, well oriented bubbles. This was also confirmed

by Jeffries et al. (1991) from a lake ice core drilled in a trough on Hobson's Choice Ice Island, which was described as having a coarse (10-20 mm) or very coarse (>20 mm) texture with large columnar grains and a horizontal c-axis orientation. In addition to having spherical and elongated bubbles, the lake ice also contained tubular bubbles 1-2 mm in diameter and as much as 300 mm long, perpendicular to the surface of the ice. Several other studies have also documented lake ice as having a columnar structure (Marshall 1955, 1960; Crary, 1958).

Sea ice consists of a heterogeneous mixture of pure ice grains, gas (air bubbles) primarily teardrop in shape, and brine pockets, which can be in liquid or solid form (Ragle et al., 1964; Shokr & Sinha, 1994). Due to its heterogeneous content, sea ice typically appears as a more cloudy ice type. Brine pockets are formed from the accumulation of salt, which are trapped between the ice grains. New sea ice is usually very salty due to the high number of brine pockets, but it becomes less saline with age as the brine eventually drains through the ice back into the ocean (Weeks and Gow, 1978). Sea ice can have a columnar and granular ice texture, with its grain orientation related to the dominant direction of water currents under the ice cover (Weeks and Gow, 1978) or wind direction, in new ice (Sinha, 1986). For example first-year ice in the western Canadian Arctic (Mould Bay, Prince Patrick Island) was observed to have vertically-oriented frazil ice crystals with a c-axis randomly oriented in the horizontal plane, which was attributed to the strong westerly wind present during the formation of the ice cover (Sinha, 1986; Shokr & Sinha, 1994). Similar studies by Weeks & Gow (1978) showed that the alignment of the oriented columnar ice in the northern part of Alaska, in landfast ice, was

related to the dominant water current orientation under the ice cover. The granular or columnar texture will also be determined by the wind. For example, Eicken & Lange (1989) showed that during low wind speeds, an undeformed ice cover forms and columnar ice is dominant. In contrast, under high wind speeds a heavily ridged and rafted ice forms and granular ice is most common.

## **2.4. Synthetic Aperture Radar (SAR) backscatter and ice**

### **2.4.1. Principles of SAR**

Although optical satellite imagers (e.g. Landsat) provide fine spatial resolution of the Earth's surface, they depend on solar illumination, limiting them to daylight observations, and are inhibited by clouds. By moving to the microwave portion of the spectrum and using an active microwave sensor, the limitation of cloud coverage and darkness is removed. However, the first generation of these systems had very poor spatial resolution (McCandless & Jackson, 2004). This was overcome by using a synthetic radar antenna (or SAR), which achieves better resolution in the azimuthal direction (direction of flight) by using a small antenna to transmit a relatively large beam. A special data processing technique is then used to synthesize the azimuthal resolution of a very narrow beam. These synthetic apertures are several orders of magnitude larger than the physical transmitting and receiving antenna, producing images with a resolution of a few meters. The beam width of the radar, which is directed off nadir and orthogonal to its direction of travel (also known as side-look view), will illuminate an area on the Earth's surface.

The SAR imaging technique works by transmitting microwave energy which propagates through the atmosphere and interacts with the Earth or Ocean surface. Through signal processing, the radar will collect phase and Doppler measurements that allow for an aperture to be constructed or synthesized, which is the basic concept behind SAR (McCandless & Jackson, 2004; Curlander & McDonough, 1991; McCandless, 1989; Raney, 1998; Tomiyasu, 1978; Sullivan, 2000). As the microwaves interact with the surface, part of that energy is bounced back to the SAR system and, this backscatter is measured and recorded by the radar receiver. The normalised measure of the radar return is known as  $\sigma^0$  (sigma nought), the radar scattering coefficient, the backscatter coefficient, or the normalized radar cross section, and is defined as the energy received per unit ground area. The amount of backscattered energy is determined by the properties of the target area or object (Bakker et al., 2004). The intensity of the backscatter varies according to the roughness of the surface along with the dielectric properties and local slope.

Radar is able to determine the distance between the transmitter and reflecting target (called range or slant range) by precisely measuring the time difference between when the pulses are transmitted and when the reflected energy is received back by the radar. The range resolution describes the capability to distinguish two different objects that are separated by some minimum distance (Bakker et al., 2004). If the radar system can sufficiently distinguish a separation between those two objects, then a different resolution cell will be assigned for each of them, making them distinguishable from one another in an image. If there is no discrimination between the objects the radar return will be a more

complex combination of the backscattered energy of two or more objects (McCandless & Jackson, 2004).

When analyzing a radar image, even for a single surface type, there will be a large amount of variation between adjacent cells, which creates a grainy texture called speckle that is characteristic to radar images. It arises from the constructive and destructive interference of backscatter energy at the pixel and subpixel scale. Speckle can be classified as a micro-texture of the image, which can degrade the image quality and make interpretation difficult. However, speckle can be statistically characterized and may be reduced by means of multi-look processing or spatial filtering methods (Bakker et al., 2004).

#### ***2.4.1.2. Frequency and wavelength***

In addition to the relative roughness and dielectric properties of a material, the frequency of the transmitted radar waves control the penetration depth (Bakker et al., 2004). In radar remote sensing, the microwave portion of the electromagnetic spectrum is used, with frequencies varying between 0.3-300 GHz. This equates to wavelengths between 0.5 and 100 cm for most common radar satellites (Bakker et al., 2004). Longer wavelengths penetrate to greater depths than shorter wavelengths, but with relatively lower image resolution (Figure 2.5). For example, X-band radar with a frequency range from 8-12.5 GHz (2.4-3.75 cm wavelength) will only penetrate through the first few cm of dry snow and/or be reflected away from the radar, but it will provide high resolution imaging. In contrast, an L-band radar with a frequency ranging from 1-2 GHz (~24 cm wavelength)

will provide lower resolution imaging, but the radar will penetrate through dry snow and far into the ice volume beneath. The penetration depth of C-band SAR into cold polar firn is typically  $9 \pm 2$  m, on exposed ice surfaces it is  $1 \pm 2$  m, and with temperate ice it is  $4 \pm 2$  m (Rignot et al., 2001). A saline-free profile in the upper-most layer allows more microwave energy to penetrate and interact with the internal structure of the ice (air bubbles, grain diameter and orientation). According to Shokr (1994), the penetration of C-band RADARSAT-2 imagery is 30 cm in multi-year sea ice. However, Fung & Eom (1982) estimated penetration to be around one meter in multi-year sea ice. SAR penetration is far less in sea ice, due to its higher salinity which absorbs the microwave energy. In freshwater ice, or into ice nearly free of impurities such as salts and air bubbles and a temperature of  $-5^{\circ}\text{C}$ , penetration depth can be up to 14 m (van der Sanden & Drouin, 2011).

By using the characteristics of different wavelengths it is therefore possible to discern information about the structure of the snow and ice interface. It is important to note when choosing a radar imaging wavelength that it needs to be matched to the characteristics of the surface being studied. For example, a small feature will be best recognized with X-band due to its shorter wavelength, while larger features such as geology, or large scale glaciology, will be best studied using L-band imagery (Parker, 2012). Furthermore, the penetration depth will depend on the moisture content of the surface, with dry surfaces allowing the radar wave to penetrate deeply, while penetration on wet surfaces will be no more than a few millimetres, if at all (Bakker et al., 2004).

### ***2.4.1.3. Polarization***

Polarization refers to the orientation of the electric field component of the electromagnetic wave. Many different polarization configurations are possible in radar imaging, although linear polarizations (HH, VV, HV, VH) are most commonly used, where “H” stands for horizontal and “V” for vertical. The first term in the polarization configuration corresponds to the polarization of the transmitted radiation, while the second term corresponds to the polarization of the received radiation (e.g., **HV** for horizontal transmitted and vertical received) (Parker, 2012). Channels HH and VV are referred to as like-polarized (co-pol), while HV and VH are referred to as cross-polarized, because they transmit and receive in orthogonal polarization to one another. There are four different combinations of polarization that radar systems typically have (Parker, 2012):

1. Single polarization (HH or VV) where the radar system operates with the same polarization for both transmitting and receiving;
2. Cross polarization (HV or VH) where the radar system uses a different polarization when transmitting and receiving
3. Dual polarization (HH and HV, VV and VH, or HH and VV), where the radar sends both horizontally and vertically polarized electromagnetic waves.
4. Quad polarization, also known as polarimetric (HH, VV, HV, and VH), where the radar system alternates the transmission pulses between H and V and receives the signal in both H and V polarization (Parker, 2012). This allows for measurement

of the terrain's polarization signature and can therefore allow for improved classification compared to the use of backscatter at a single polarization.

#### ***2.4.1.4. Incidence angle***

The incidence angle is referred to as the angle between the nadir and the radar illumination directions (where the radar intersects the surface) (Parker, 2012). The backscatter coefficient will vary according to the incidence angle. There is a complex interaction between the microwaves and the ground such that different reflections occur in different angular regions. SAR operates in a side-looking orientation, which results in tall objects and relief, such as mountains, being subject to displacement in the resulting imagery. According to Parker (2012) there are three factors to take into consideration when using SAR data:

1. Shadows on radar images, which appear dark in the imagery, are areas on the ground that are not illuminated by the signal, meaning that no return signal is received. However, shadowing can be important for relief interpretation because the height of an object can be derived from the radar shadow.
2. When objects are tilted toward the radar, the features can appear compressed, which is called foreshortening. This can be reduced when increasing the incidence angles. However, with the reduction of the incidence angle the shadow effect will increase. Thus the selection of the incidence angle to use is a trade-off between the acquisition's occurrence of foreshortening and radar shadowing.

3. The final factor is layover, which occurs when the reflected signal from a feature's upper portion is received before the return of the lower portions, displacing the upper feature in relation to its lower portion.

#### **2.4.2. Microwave interaction (scattering) with the Earth's surface**

Sigma nought ( $\sigma^0$ ) is an absolute measurement of the scattering behavior of the target or object observed, and refers to the amount of energy received in proportion to the transmitted energy. The backscattered energy will depend upon the characteristics of the illuminated object, which is controlled by a variety of factors such as its roughness, shape, orientation, dielectric constant and dielectric discontinuities (Bakker et al., 2004)

The *surface roughness* of the terrain is the most influential factor in controlling the strength of the radar return (Bakker et al., 2004). Surface scattering is the result of the transfer of energy across the boundary between two dissimilar features and strongly depends upon the transmission coefficient of that boundary. The surface roughness can be smooth, intermediate, or rough according to the classification of its reflective properties (Johnston and Timco, 2008). A smooth surface will reflect the energy away from the antenna without returning a signal, resulting in a darker image (Onstott & Shuchman, 2004). The amount of energy reflected away from the antenna is reduced when there is an increase in surface roughness of the terrain, which will increase the backscattered component. A greater amount of backscattered energy will result in a higher strength signal, which is represented by a brighter region on the image. An example of the effect of surface roughness can be observed in water bodies. During

periods of calm wind, the surface has a greater tendency to be smooth, which will cause most of the energy to be reflected away from the radar whereas a wind-stressed water body will have a higher surface roughness and backscatter will be relatively high. Some land surfaces are relatively rough, such as trees, mountains, or urban areas, which will scatter the energy across the surface and result in a brighter image (Bakker et al., 2004).

The interaction of microwaves and imaged materials is a function of the complex dielectric constant. Dielectric constant is a measure of the electrical properties of the surface materials and consists of both the permittivity and the conductivity of the material, both strongly dependent on the medium's moisture content. A material or terrain with a high dielectric constant will result in a strongly reflective surface. When comparing two surfaces with equal roughness, but with different radar returns, then we can conclude that their differences are due to their dielectric properties. For example, in the case of sea ice this can be due to differences in salinity, which is a major determinant of the dielectric constant (Bakker et al., 2004).

Scattering mechanisms can occur through many forms, such as reflection off a smooth surface and scattering off a rough surface. However, there are also several other possibilities such as double bounce, volumetric scattering, and absorption (or extinction) (Bakker et al., 2004). Volume scattering is the result of the microwave energy being transmitted across an interface where it interacts with inhomogeneities in a volume of material (Johnston and Timco, 2008). Double bounce refers to the interaction of radar with a smooth surface, such as water, which causes reflections away from the sensor

towards another object, such as a tree, which then reflects the energy directly back to the sensor (Onstott & Shuchman, 2004).

### **2.4.3. SAR interactions with ice**

Previous research into the interaction of SAR imagery and ice has used C-band SAR (RADARSAT-1 and -2, ERS-1 and -2 and ENVISAT) for the most part (Onstott & Shuchman, 2004). In the case of sea ice, RADARSAT imagery has been used to detect, locate, and identify a variety of sea ice forms and features that include: ice type; surface features; floe size distribution and concentration; ice edge; leads and polynyas; deformation; as well as ice edge eddies and open ocean phenomena associated with the ice pack (Onstott & Shuchman, 2004). Other features of interest may include detecting icebergs and ice islands (Lewis-Paley, unpublished).

SAR has been used to classify ice since 1984 (Canadian Intera STAR-1 airborne radar) and spaceborne SAR has proven to be an excellent tool for ice analysis for several reasons. Satellite orbits converge in the Polar Regions, which allows for frequent repeat imaging of the surface. SAR sensors also function at night and through clouds. Furthermore, SAR is sensitive to different ice types due to salinity gradient, and it is affected by the ice crystalline structure, particularly the grain shape, orientation, and the geometrical characteristics of inclusions (Shokr and Sinha, 1994). These aspects explain why satellites such as RADARSAT-2 are widely used for monitoring the ice cover of the High Arctic, because this region is shrouded in darkness during the winter and is covered by clouds ~70 to 90% of the time (NRC, 2013). Furthermore, the identification of

different cryospheric features benefits from multiple polarizations (HH, VV, HV, and VH) that are provided by RADARSAT-2. These different polarizations improve analyses such as ice-edge detection, ice-type discrimination, and ice topography and structure information.

Ice classification is best conducted with winter and early spring SAR scenes when the ice/snow surface is cold and dry. Summer melting of the snowpack increases microwave attenuation and reduces backscatter (Steffen et al., 2004). Johnston and Timco (2008) showed that multiyear sea ice has a relatively high backscatter, due to its relatively high concentration of bubbles and low-salinity (Figure 2.6, red outline). In addition, MYI floes typically contain ridges and hummocks of large grained, porous ice which also tend to increase volume scattering and double bounces (Shokr and Sinha 1994). Other ice types, such as iced firn and epishelf lake ice can also elicit high backscatter due to volume scattering, which is influenced by the granular/coarse texture of these ice types and a double bounce reflection between vertically oriented bubbles and the horizontal ice-water interface (Jeffries, 2002) (Figure 2.4, epishelf lake). In contrast, backscatter is relatively low in FYI. New sea ice with a smooth surface causes incident microwave energy to be reflected away from the radar receiver, resulting in a darker SAR signature (Figure 2.6, blue outline). The energy that is not reflected by the smooth surface will penetrate the ice surface to become absorbed by the brine pockets, which have a greater salinity concentration, again leading to a darker SAR signature (Johnston and Timco, 2008). These examples illustrate that, for a given ice type, the relative importance of surface and volume scattering depends upon the roughness of the air-ice or snow-ice interface, the

dielectric constant of the ice, the presence or absence of liquid water or brine, and the presence of volume inhomogeneities (Johnston and Timco, 2008).

Past research has provided insight into different ice types on Ellesmere Island based on differences in SAR returns. Table 2.2 illustrates the different  $\sigma^0$  values for epishelf ice, ice shelf ice, and different sea ice ages and thicknesses using several different satellite systems: RADARSAT 1 and -2, ERS-1, JERS-1 and EOS. This compilation reflects the fact that there has been more research conducted on the backscatter of sea ice than other ice types. The highest radar backscatter (in HH polarization) is epishelf lake ice with an average of  $>-6$  dB, followed by the ice shelf ice with an average of  $-13$  dB, with the sea ice with the lowest average radar return of  $\sim-17$  dB (Table 2.2). These results highlight the fact that freshwater ice provides a brighter radar return than saline ice. Freshwater ice along the northern coast of Ellesmere Island (in HH polarization) includes epishelf lake ice ( $>-6$  dB; Veillette et al., 2008), glaciers and ice caps ( $\sim-5$  dB; Casey & Kelly, 2010), and ice shelves ( $\sim-13$  dB; White et al., 2015).

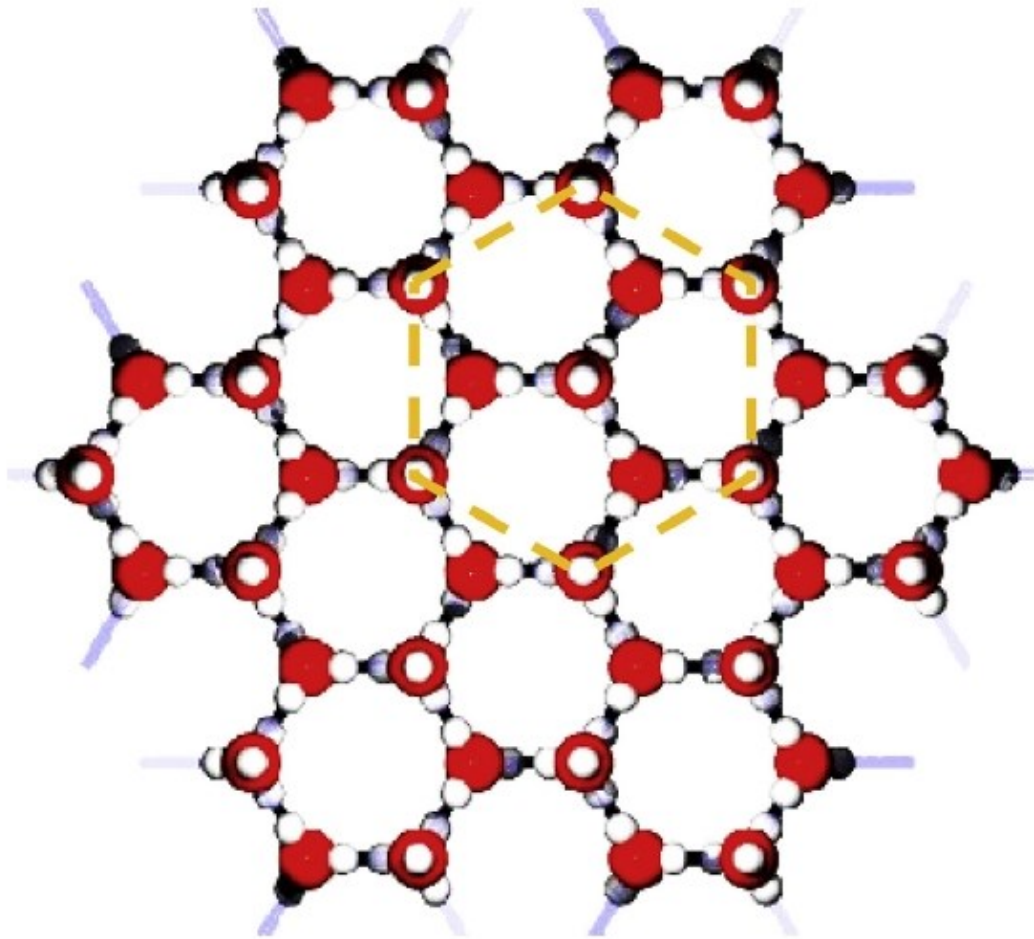


**Figure 2.1:** Representation of the crystal lattice of ice Ih. Spheres (red and white) represent oxygen and hydrogen atoms, respectively. Rods (grey) represent hydrogen bonds. The yellow dashed line symbolizes the hexagonal symmetry of the lattice (Faria et al., 2014b). The c-axis of the crystal is perpendicular to the plane shown here.

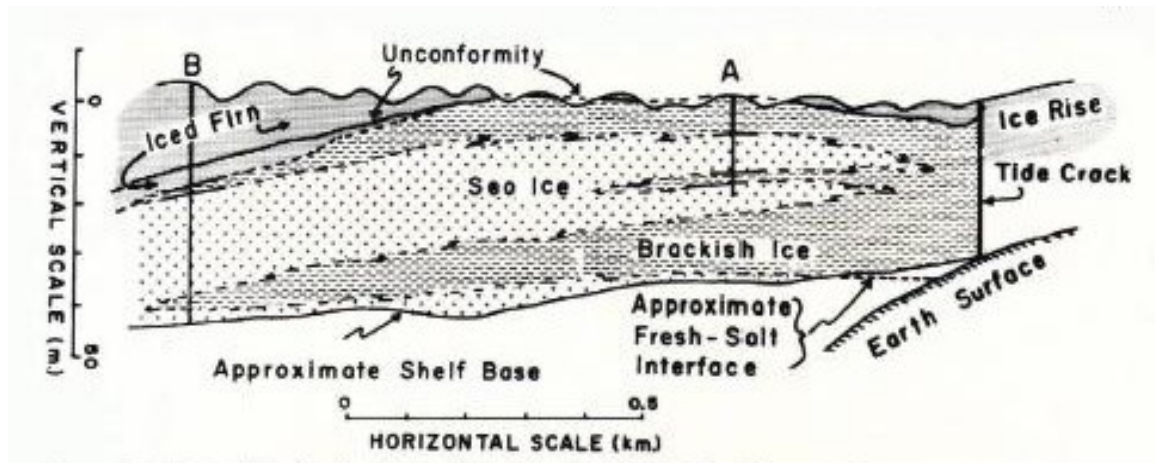


**Figure 2.2:** Interpretation of two distinct stratigraphic units found in part of the Ward Hunt Ice Shelf. This cross section was based on two ice cores (A, B) and laboratory analyses and shows alternating stratified basement ice (brackish ice) and old sea ice layers. After Lyons et al., 1971.

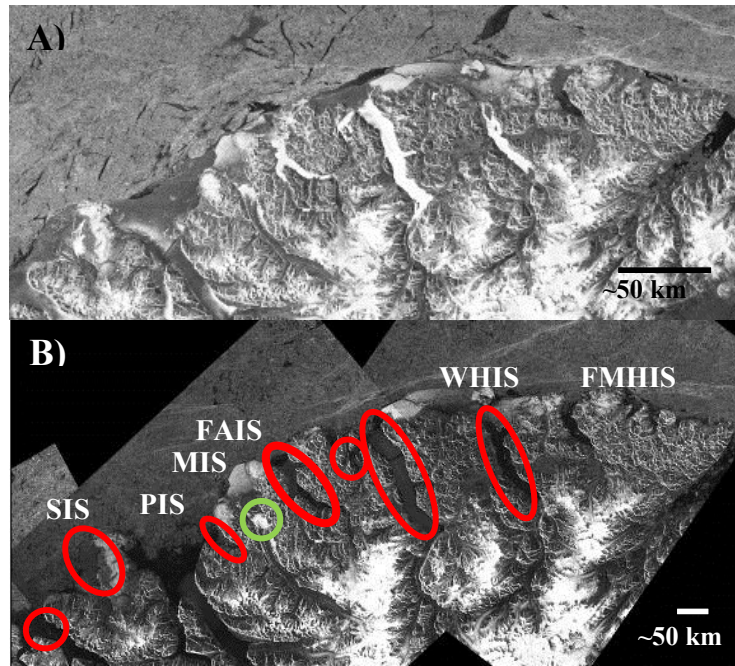


**Figure 2.3:** Backscatter of ice dammed lake ice and environmental change. A) RADARSAT-1 Wide Beam B Scan-SAR image of northernmost Ellesmere Island, February, 2002 (© CSA 2002). A bright SAR signature indicates the presence of an ice dammed lake (including epishelf lakes) (c.f., Jeffries. 2002; Veillette et al., 2008). B) RADARSAT-2 Wide Beam images, March, 2009 (©MDA 2009) with major remaining, and former ice shelves (from left to right): former Serson Ice Shelf (SIS), Petersen Ice Shelf (PIS), Milne Ice Shelf (MIS), former Ayles Ice Shelf (FAIS), Ward Hunt Ice Shelf (WHIS), and former Markham Ice Shelf (FMHIS). Areas of bright SAR return in 2002 appear darker with the exception of the Milne Fiord Epishelf Lake (green circle) which indicates the loss of the freshwater ice and the ice dammed lakes (Mueller et al., unpublished).

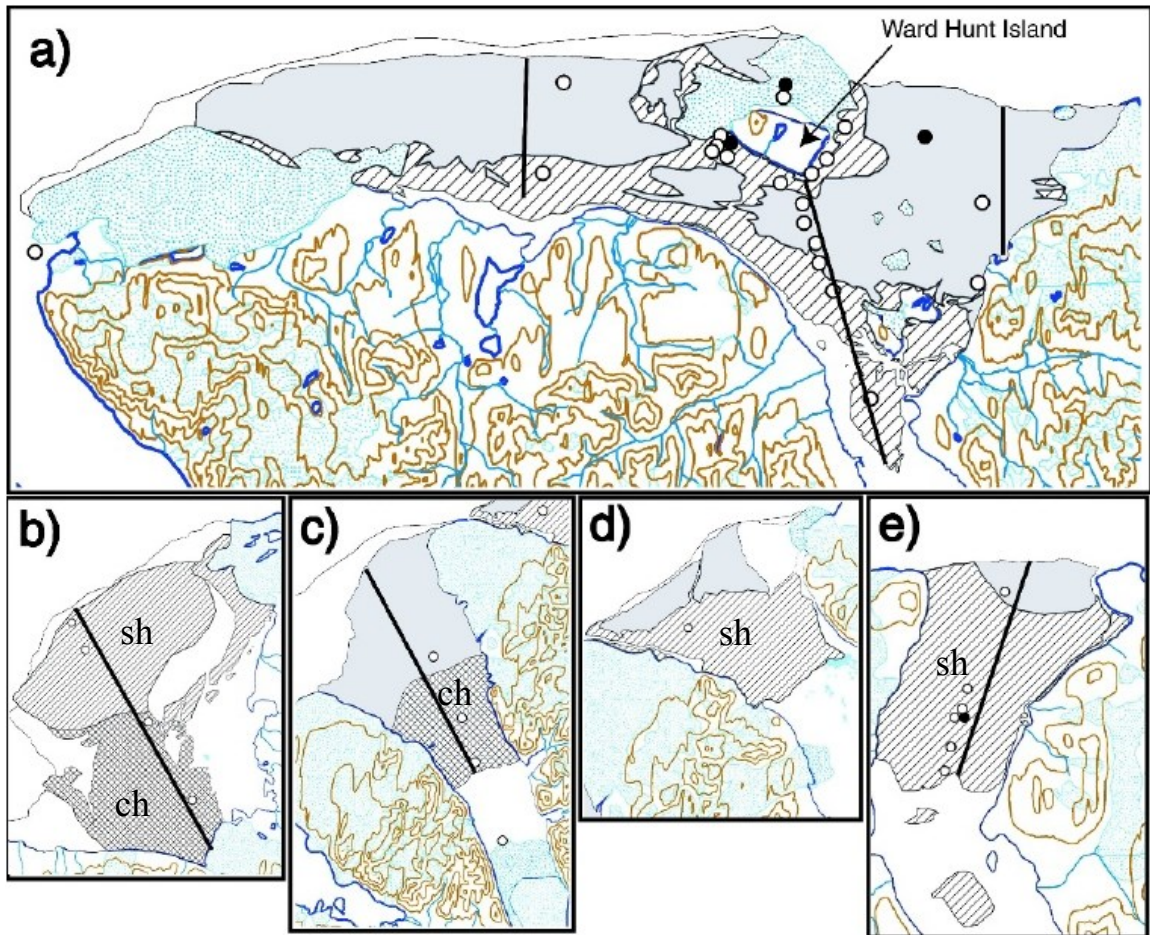


**Figure 2.4:** Different ice types found along the northern coast of Ellesmere Island. Stipple indicates ice rises and glaciers, a simple hatch (sh) indicates exposed basement ice (marine ice), solid grey indicates iced firn (meteoric ice) and cross hatch (ch) indicates floating glacier portions of ice shelves. A) Ward Hunt Ice Shelf, B) Serson Ice Shelf, C) Milne Ice Shelf, D) Ayles Ice Shelf, E) Markham Ice Shelf. After Mueller et al., 2006.

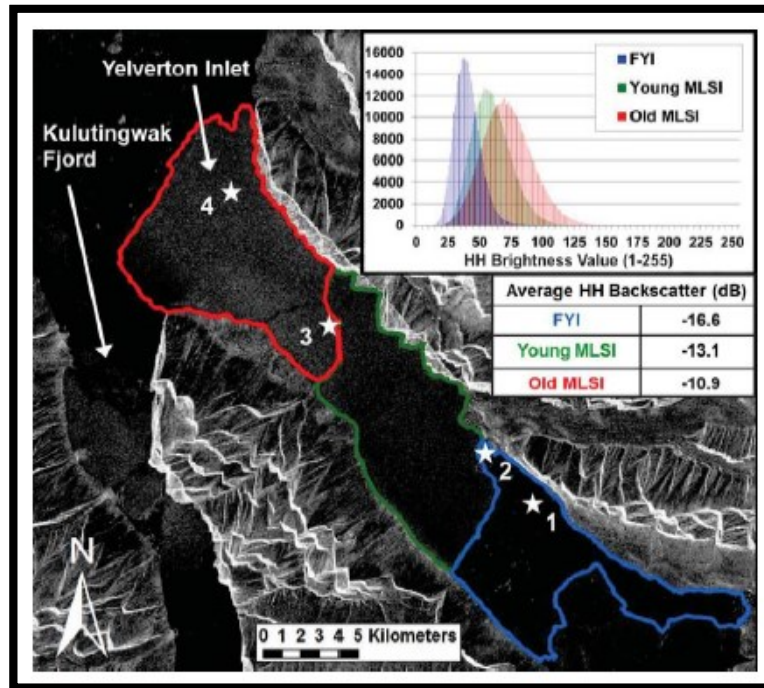


**Figure 2.5:** Examples of SAR backscatter (RADARSAT-2 wide beam mode (March, 5 2009), over different sea ice types. Multiyear Landfast Sea Ice (outlined in red) has a high backscatter due to low salinity and greater bubble concentration within the first meter below the surface, resulting in volume scattering. First year ice (outlined in blue) has a lower backscatter due to higher salinity concentration, resulting in the absorption of the radar (Pope et al., 2012). Stars show location of ice core extraction by Pope et al. (2012).

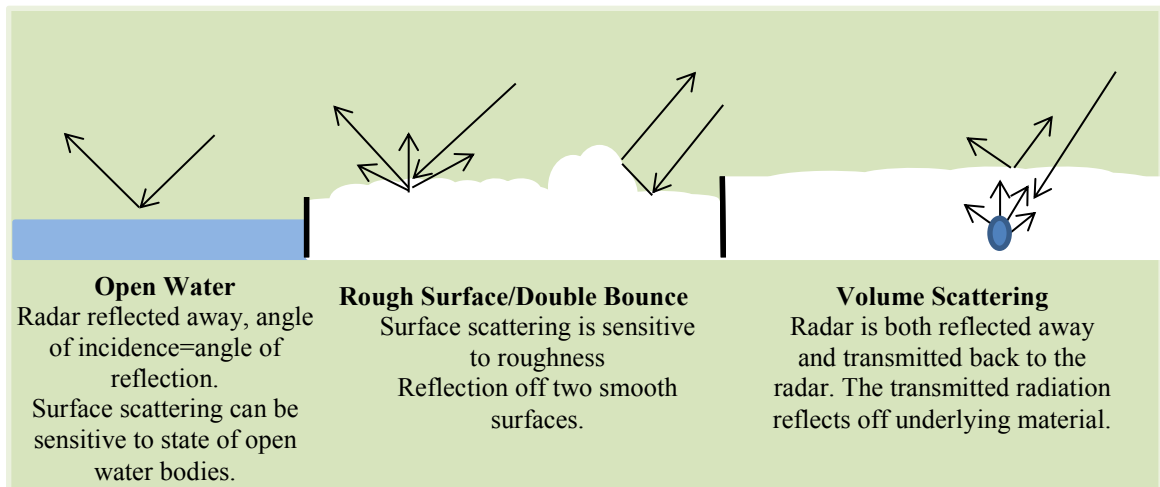


**Figure 2.6:** Examples of multiple SAR scattering mechanism across different surfaces. Smooth surfaces reflect the radiation away from the sensor without returning a signal, resulting in a dark tone. A rough surface yields surface scattering, resulting in a brighter toned image. Double bounce occurs when the radar interacts with two surfaces at right angles to each other, which enhances the amount of energy reflected back to the sensor. Volume scattering is the result of the radiation being transmitted across an interface and then interacting with inhomogeneities in a volume of material, resulting in a brighter toned image.

**Table 2.1:** Compilation of bulk salinity and temperature data from different ice types from Northern Ellesmere Island.

<b>Ice type</b>	<b>Bulk salinity (psu)</b>	<b>Ice temperature (°C)</b>	<b>Reference</b>
<b>FYI</b>	<1-2	-2.7 to -1.1	Pope et al., 2012
<b>Old MLSI</b>	<1 to >5	(-6 and -4) to -2	Pope et al., 2012
<b>Petersen Ice Shelf ridge [1]</b>	<1	-15 to -10	White et al., in revision
<b>Petersen Ice Shelf ridge [2]</b>	>2	-10- to -5	White et al., 2015
<b>Petersen Ice Shelf ridge [3]</b>	>79	NA	White et al., 2015
<b>Petersen Ice Shelf ridge [4]</b>	>4	~-5	White et al., 2015
<b>Brackish ice</b>	Mean 0.22±0.15	NA	Jeffries and Sckinger, 1989
<b>Sea ice</b>	Mean 1.26±0.65	NA	Jeffries and Sckinger, 1989
<b>Iced firn</b>	<0.01	NA	Jeffries et al., 1988
<b>Non-saline basement ice*</b>	<0.01	NA	Jeffries et al., 1988
<b>Non-saline basement ice**</b>	0.18±0.11	NA	Jeffries et al., 1988
<b>Combination basement ice***</b>	0.70±0.7	NA	Jeffries et al., 1988
<b>Saline basement ice**</b>	2.22±0.6	NA	Jeffries et al., 1988
<b>Stratified basement ice</b>	0.19	NA	Lyons et al., 1971
<b>Sea ice</b>	1.25	NA	Lyons et al., 1971
<b>Basement ice, transition type</b>	0.13	NA	Lyons et al., 1971
<b>Iced firn</b>	<0.01	NA	Lyons et al., 1971

[1] 0-5.5 m depth; [2] 5.5-13.24m depth; [3] slush ice layer; [4] 11-13 m depth; \* East Ward Hunt Ice Shelf; \*\* West Ward Hunt Ice Shelf; \*\*\* South Ward Hunt Ice Shelf.

**Table 2.2:** Compilation of the SAR backscatter (dB) in HH polarization of various ice types.

Ice type	$\sigma^0$ (dB)	Comments	Reference
<b>Epishelf lake ice</b>	>-6; -5.16	RADARSAT-1; RADARSAT-2	Veillette et al., 2008; White et al., 2015
<b>Ice shelf ice</b>	-12.5	RADARSAT-2	White et al., 2015
<b>Sea ice (all)</b>	-17.92	RADARSAT-2	White et al., 2015
<b>FY</b>	-16.6; -11.5; -14.2	RADARSAT-2; ERS-1; EOS	Pope et al., 2012; Onstott, 1992
<b>Thin FY</b>	-13.3; -23.4	ERS-1; JERS-1	Onstott, 1992
<b>Medium thickness FY</b>	-23.4	JERS-1	Onstott, 1992
<b>Thick FY</b>	-23.4; -11.45; -11.18; -12.52; -13.34	JERS-1; RADARSAT-1 20-30°*, 20-30°**, 30-40°*, 30-40°**	Onstott, 1992; Shokr, 2009
<b>SY</b>	-11.35; -14.1; -14.29	RADARSAT-1 20-30°*, 30-40°*, 30-40°**	Shokr, 2009
<b>MY</b>	-8.6; -7; -3.6; -12.4; -11.68; -12.8; -12.44	ERS-1; JERS-1; EOS; RADARSAT-1 20-30°*, 20-30°**, 30-40°*, 30-40°**	Onstott, 1992; Shokr, 2009
<b>MLSI</b>	-13.2	RADARSAT-2	Pope et al., 2012
<b>Old MLSI</b>	-10.9	RADARSAT-2	Pope et al., 2012

*First year sea ice (FY) / Second year sea ice (SY) / Multiyear sea ice (MY) / Multiyear landfast sea ice (MLSI); \* Average backscatter from homogenous polygons; \*\* Estimated backscatter from RADA (radiometric database algorithm).*

## **Chapter 3 Methods**

### **3.1 Study area**

The study area is located along the northern coast of Ellesmere Island, Nunavut, Canada, one of the largest and most northerly islands in the Canadian Arctic Archipelago. More than half of its surface (84,000 km<sup>2</sup>) is glaciated (Williamson et al., 2008) (Figure 3.1). The last remaining Canadian ice shelves and epishelf lakes are found along a ~94 km stretch of this coastline.

Fieldwork was conducted on the Petersen Ice Shelf (82°31'N, 81°45'W), and the Milne Ice Shelf (82°39'N, 81°26'W), which provided access to a variety of ice types (Figure 3.1). The Petersen Ice Shelf occupies Petersen Bay, which opens towards the west into Yelverton Bay. The ice shelf surface comprises a series of elongated troughs and ridges, which have mixed orientations at the seaward edge of the ice shelf, and a northwest/southeast orientation at the landward side (White et al., 2015). There are six glaciers that flow towards Petersen Bay, although only two are currently connected to the ice shelf on the northern side (White et al., 2015).

The Milne Ice Shelf is located at the mouth of Milne Fiord, between Cape Evans and Cape Egerton. An epishelf lake lies in the fiord between the Milne Ice Shelf and the floating tongue of the Milne Glacier (Mortimer et al., 2012). The Milne Ice Shelf is comprised of two distinct units (outer and central) which were classified based on differences in surface topography, ice thickness, and ice type by Jeffries (1986).

The outer unit has surface rolls that are almost symmetrical in shape and oriented parallel to the coastline (southwest to northeast) (Jeffries, 1986) (Figure 3.1, red outline). According to Jeffries (1986), the snow surface there is relatively hard due to strong winds, compaction and weathering and there is very little debris found on the surface. This unit was later described by Mueller et al. (2006) as having a near-surface comprised of iced-firn, with high RES (radio-echo sounding) returns of  $>-10$  dB (Narod et al., 1988). The middle section of the outer unit has a lower reflectivity,  $<-30$  dB, possibly as the result of brackish, basement ice freezing to the bottom of the ice shelf (Mueller et al., 2006; Narod et al., 1988; Mortimer et al., 2012). The ice thickness ranges from  $<10$  to  $>90$  m (Jeffries, 1986; Mortimer et al., 2012).

The central unit has SW to NE oriented rolls along its northern margin (Figure 3.1, green outline). There is a moraine across much of the central unit, which contains material accumulated in conical mounds up to 10 m high (Jeffries, 1982). An ice core collected in 1983 indicated that this ice was probably of glacial origin with medium and coarse grain diameter and even edges that did not interlock much (Jeffries, 1985a; 1986) (Figure 3.2). The ice thickness in this zone ranges from 10 to 100 m (Mortimer et al., 2012).

Jeffries (1986) also described an inner unit as having a confused surface ridging and trough pattern which follows a number of different directions and has a low surface relief compared to the other units (Figure 3.1, blue outline). The RES survey conducted in 1981 by Narod (1988) showed no bottom echo, likely due to the ice being thinner than the minimum 10 m depth that could be measured with the instrument. Jeffries (1985)

reported that the ice in this region was 3.2 m thick, implying that the inner unit was not ice shelf ice at that time, in spite of the characteristic surface undulations. Using remote sensing, Mortimer et al. (2012) showed that this area of thin ice subsequently expanded by 14.4% over the period 1984-1993. The inner unit is now recognized as the Milne Fiord epishelf lake (Mortimer et al., 2012; Mueller et al., 2006; Veillette et al., 2008).

An automatic weather station in Purple Valley (82°28.983'N, 80°59.983'W), which lies between the Milne and Petersen ice shelves, has been recording the surface air temperature (SAT) since June 3, 2009 (<http://tinyurl.com/milnewx>). The average SAT for this station was -18.1°C, over the period 2008-2013, with a minimum of -52.4°C (March 3, 2013) and a maximum of 20.3°C (July 18, 2012). There are two permanent Environment Canada weather stations located equidistant (~320 km) from the Milne and Petersen ice shelves, Alert (82°32'12"N, 62°16'08"W) and Eureka (79°58'08"N, 85°55'08"W). According to historical climate data ([www.climate.weatheroffice.ec.gc.ca](http://www.climate.weatheroffice.ec.gc.ca)) the average mean temperature at Eureka (1947-2012) and Alert (1950-2006) is -19.1°C and -17.9°C, and the total annual average precipitation was 75 mm and 153 mm, respectively (191-2000 Climate Normals).

### **3.2. Fieldwork**

Fieldwork was conducted in May 2012 and May 2013. To determine which ice types to sample, sampling locations were coarsely determined *a priori* by examining the SAR backscatter values in a RADARSAT-2 image acquired on April 17, 2012 along two transects in Milne Fiord (~28 km) and across Petersen Bay (~10 km). The  $\sigma^0$  was used to

determine distinct areas of relatively homogeneous backscatter, which were targeted for field sampling. Three ice types were identified (A, B, and C) according to the April 2012 backscatter results and previous studies of the Milne and Petersen ice shelves. The first ice type, type A, corresponds to what has previously been referred to as meteoric ice, or iced firn (Marshall, 1955, 1960; Jeffries et al., 1991; Jeffries, 1992; Mueller et al., 2006), found across the outer section of the Milne Ice Shelf. Type A had a mean  $\sigma^0$  of -6 dB (HH polarization). Type B corresponds to what has previously been referred to as glacially fed shelf ice (Mueller et al., 2006; White et al., 2015) which is found across the central section of the Milne Ice Shelf, and the entire Petersen Ice Shelf. The average  $\sigma^0$  for type B was -12 dB (HH polarization). The third ice type, type C, corresponds to what has been referred to as epishelf lake ice (Mueller et al., 2006; Mortimer et al., 2012), which is found behind the central section of the Milne Ice Shelf. Although the average  $\sigma^0$  of type C (-4 dB) is similar to type A (-6 dB) it was considered to be a separate ice type based on previous literature.

For fieldwork in May, 2013 three ice core sample sites were chosen for each ice type (A, B, and C). For ice type B, two ice cores were extracted from the central Milne Ice Shelf and two from the Petersen Ice Shelf, one of which was previously extracted in May 2012. At each sample site, a snow pit was dug to the ice surface and the snow stratigraphy, as well as the snow density, was documented. The temperature of each snow layer, as well as the ice/snow and snow/air interfaces, was recorded using a *Thermor* waterproof digital stem thermometer (accuracy  $\pm 0.5^\circ\text{C}$ ). Once the snow pit analysis was finished, the surface of the ice was photographed. During the month of July 2013 some of the core

locations were re-visited and pictures of the ice surface were taken. This information was combined with the spring photos to classify the ice surface roughness according to the Rayleigh criterion. According to the Rayleigh criterion, a surface is considered smooth if:

$$h < \frac{\lambda}{8 \cos \theta} \quad (1)$$

where  $h$  is the mean height of surface variations,  $\lambda$  is the radar wavelength, and  $\theta$  is the incidence angle of the radar (Onstott & Shuchman, 2004). Otherwise, the surface is considered to be rough.

Furthermore, photographs of the environment surrounding each ice core location were taken to classify the surface heterogeneity. An ordinal scale based on the descriptions ‘very heterogeneous’, ‘heterogeneous’ and ‘homogeneous’ was used according to the following criteria: a surface was considered to be homogeneous when the area surrounding the core site (within a 50 m radius) was a flat surface, with little to no debris or crevasses. An area was classified as heterogeneous when the surrounding area had a balance between a flat surface and disturbed surface (debris, crevasses, or changes in slope). Finally, an area was classified as very heterogeneous when debris, crevasses or changes in slope were more dominant than flat surfaces.

Ice cores were extracted using a Kovacs Mark II ice coring system, with an internal diameter of 8.8 cm. Cores were drilled in ~60 cm sections, with each piece extracted and placed on a platform that was shaded from direct sunlight. The internal temperature of the

ice was taken every 15 cm along the core with a *Thermor* waterproof digital stem thermometer after drilling half way through the core diameter. The temperature was recorded after it had stabilized, usually after 30-60 s.

The core was photographed next to a ruler, and then the ice was sectioned into 10-15 cm segments. The segments were sealed in plastic bags and the up direction was carefully noted. Once each core section was processed, the coring resumed and another section was recovered until the total ice thickness was penetrated or 2 m depth was reached. Once the ice core extraction was completed, coordinates of the site were taken using a Garmin eTrex GPS (Global Positioning System), which has a horizontal accuracy of <15 m. The core segments were transported back to base camp for further analysis surrounded by snow in coolers so they would be protected from breakage. All coring was undertaken in sub-freezing temperatures (typically <-10°C).

At the field camp, a detailed visual assessment of each core segment, in natural light, was completed. This provided a descriptive analysis of its structure (bubble inclusions, fractures, sediment layers, and cloudiness) by visually determining the differences (layers, bubbles, sediment, clarity of the ice) and documenting the results. The first 60 cm of each ice core and the entire type C cores were all returned frozen to Carleton University. A 1 cm long piece of every second ice core segment from the remaining ice samples was melted completely in the field and a YSI Pro Plus multi-parameter sonde was used to record the temperature and conductivity of the sample. The remaining segments were transported frozen to Carleton University for the remainder of the

analyses. Conductivity of the uppermost 60 cm of each core, as well as the type C samples was obtained as described above. Conductivity and temperature were converted to salinity ( $\pm 0.1$  psu) using the calculation by Fofonoff and Millard (1983).

### **3.3. Survey of surface conditions**

A visual survey of surface conditions was conducted on the Milne Ice Shelf on May 13, 2013 by photographing surface anomalies such as ridges and troughs, debris covered areas, fractures, and snow drifts along a 39.7 km transect. The survey started at the northwest edge of the Milne Ice Shelf on the sea ice at  $81^{\circ}56'17.309''\text{W}$ ,  $82^{\circ}43'3.9''\text{N}$  and ended at the Purple Valley Base Camp at  $80^{\circ}47'15.455''\text{W}$   $82^{\circ}29'2.619''\text{N}$ . Each photograph was georeferenced using a Nikon GP-1 GPS (10 m horizontal accuracy) to provide a qualitative interpretation of the variable surface scattering across the Milne Ice Shelf where ice core extraction was not possible.

### **3.4. Laboratory work**

#### **3.4.1. Sample preparation**

The sample preparation was conducted in a walk-in freezer at Carleton University (Ottawa, ON) that was set to a mean temperature of  $-10^{\circ}\text{C}$ . Ice segments were selected for textural analyses based on a visual assessment of the ice cores and changes in salinity profiles. This was based on any obvious changes in ice structure (i.e., changes in bubble diameter, or visual appearance) down each core. A thin section was then taken segments that were representative of the visually different ice types. Zones of different ice

structures also coincided with changes in the salinity profiles. Thin sections were taken every ~50-100 cm below the ice surface, which provided information for the top, middle and bottom of each ice core. Most of the ice textural analyses followed the procedure detailed in Langway (1958) in the preparation of thin sections, supplemented by improvements proposed by Durand et al. (2006):

Horizontal (perpendicular to the core axis) thick sections, ~1 cm in thickness, were cut from selected ice core segments (Table 4.1) using a Makita radial arm saw, which were then photographed under natural and polarized light. Vertical (parallel to the core axis) ~1 cm thick sections were also cut from selected ice core segments (Table 4.1) and photographed under natural and polarized light. The base of each thick section was slightly melted on a hot plate and then glued (frozen) on a glass plate. To ensure that the thick section was properly glued to the glass plate a few drops of water were added around the sides. Subsequently, the thick sections were planned using a microtome blade mounted on a Leitz 1300 sledge base. To accelerate the process of the planning, the surface was melted with a hot plate (Thorsteinsson, 1996; Negi & Kumar, 2004).

The section was reduced to a thickness to between 0.3 and 0.4 mm by using the microtome knife and/or the melting technique. The thinner the section, the sharper the colour transitions are between grains (Durand et al., 2006).

### **3.4.2. Ice texture analysis**

The ice texture was viewed by mounting each thin section on a Rigsby stage. A Rigsby stage is a 4-axis universal stage including both an inner vertical and an outer vertical axis (Wilén et al., 2003). At the bottom, a polarizing filter is oriented in one direction (along E-W in a local reference frame), and the second polarizer, found above the sample, is oriented perpendicular to the first polarizer (along N-S). Each thin section that was prepared, which was bonded to a glass plate using the above technique, was placed between the two polarizing filters on the Rigsby stage. A diffuse light illuminated the samples from beneath the lower polarizing filter for viewing the grain texture (Wilén et al., 2003). When the light passes through ice grains they will appear coloured, with the colour depending on their orientation and/or the rotation angle of the thin section in relation to the polarizers (Wilén et al., 2003). If the grain is oriented parallel to its c-axis, extinction will occur and the grain will appear dark because it is transparent against the dark background of the cross polarizers. It is important to note that it is possible that two grains side by side can appear as a single grain in certain orientations. By rotating the stage, the separate grains will be resolved. To avoid this problem, multiple images were taken of the thin sections during the rotation of the axes.

The grains were oriented with the universal stage using the following procedure (Langway 1958):

- (1) The horizontal axes were set to zero.

- (2) Grains that were selected for measurement were rotated on the axis until extinction was reached (when light is parallel to the c-axis) to ensure that the proper measurements of the grains were taken.
- (3) To test the extinction, the axes were rotated by 45° multiple times, to ensure that the full length and width of each grain was captured.
- (4) At each angle a photograph was taken with a Nikon D7100 camera with a 105 mm focal length macro lens.

Each thin section photograph was used to measure the grain length and width. For each thin section, approximately 10-15 ice grains were measured but this depended on the amount of grains per thin section. Both the length and width of each grain were measured to measure the diameter, which was taken as the mean of the length and the width of the grain. The length and width were decided according to the 0°/180° angle starting point, or parallel to the line of sight (normal to the thin section) (Langway, 1958), of the universal stage, and were measured according to the full extinction of the grain to provide the proper measurement. No c-axis orientation measurements were made.

### **3.4.3. Remote sensing/SAR backscatter analysis**

Two fine quad wide beam mode (FQW13) RADARSAT-2 images were acquired on April 27, 2013 with a near range incidence angle of 32.4°, a resolution of 5.2 m (range) x 7.6 m (azimuth) and pixel size of 4.7 m (range) x 5.1 m (azimuth). These provided HH, VV, HV, and VH polarizations, and were calibrated to produce a  $\sigma^0$  image in a linear power scale for quantitative analysis. Only the first three polarizations were used in this

analysis as VH and HV yield the same information, according to the principle of reciprocity. The satellite images were projected to an Albers Equal Area Projection with a WGS 1984 ellipsoid and georeferencing was confirmed against the 1:250,000 scale National Topographic Database vector layer of the coastline of Ellesmere Island (CanVec, Geogratis, NRCan).

The location of each ice core was mapped onto the RADARSAT-2 images in ArcGIS 10.0. A square polygon of 100 x 100 m was created around each sample location and  $\sigma^0$  values within that area were extracted for further analysis.  $\sigma^0$  values for each polarization (HH, VV, HV; VH was ignored assuming reciprocity) from ~245 pixels were exported to generate statistics on the backscatter for each ice type.  $\sigma^0$  values were left in a linear power scale for statistical analyses but are reported in log scale (dB units). The standard deviation in the backscatter along with the co-polarization (co-pol; HH/VV) and the cross-polarization (cross-pol; HV/HH & HV/VV) ratio were also determined.

#### **3.4.4. Statistical analysis**

All statistical analysis for this study was carried out using R scripting and statistical software (R version 3.1.1 (2014-07-10)). All data were aggregated to the core/sampling site level by averaging individual textural observations to represent each thin section; averaging each bubble and thin section to represent every segment and then taking aggregate measurements of each segment, or SAR pixel to provide a dataset on a sampling site basis. Descriptive statistics were tabulated to characterize each variable by ice type. Due to non-normally distributed variables (most of the ice property variables

and the two cross-pol variables), the Kruskal-Wallis test was conducted to examine difference in the medians of each ice type. This tested the hypothesis ( $H_1$ ) that not all ice types had the same distribution. Analysis of Variance (ANOVA) was used to examine difference of means for normally distributed variables (SAR backscatter, co-pol ratio, vertical thin section grain length, width and size and horizontal bubble diameter). This tested the hypothesis ( $H_1$ ) that not all ice types were drawn from the same population. Scatterplot and correlation matrices were analysed to determine which variables were related to each other, with an emphasis on relating SAR variables to ice property variables. Promising correlations were evaluated using Pearson's or Spearman's  $r$  depending if they were normally or not-normally distributed, respectively. These results can then be interpreted to better understand the interaction between SAR microwave energy and the ice.

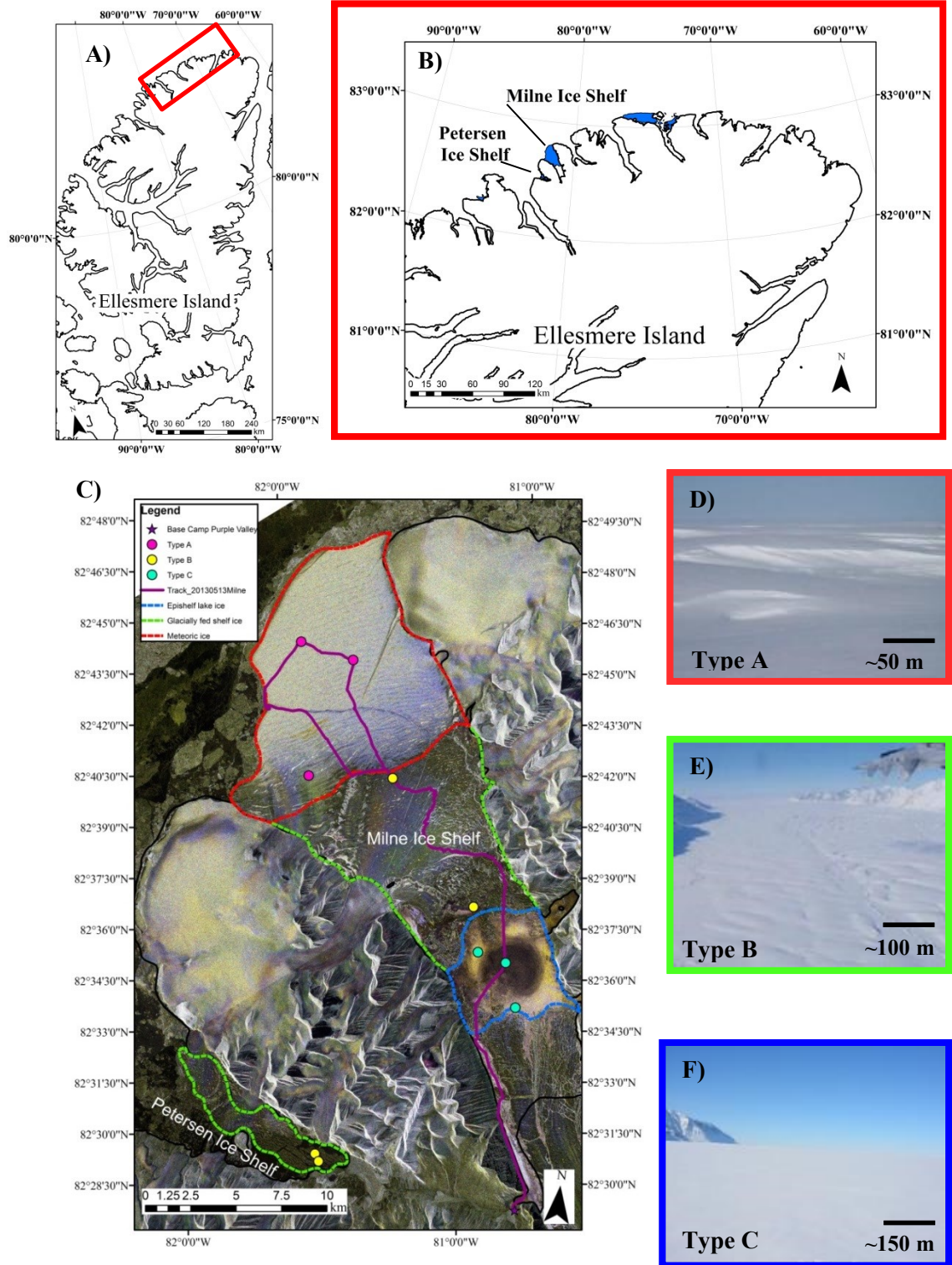


**Figure 3.1:** A) Location of study site on northern Ellesmere Island, B) NW coast of Ellesmere Island showing location of the Milne and Petersen ice shelves. C) RADARSAT-2 image (wide beam mode, April 27, 2013) of the Milne and Petersen ice shelves showing the ice core extracted for each ice type. D-F) Snow covers across ice type A, B, and C, respectively, taken during the May 2013 fieldwork. 55



**Figure 3.2:** Photograph of ice core thin section, under cross-polarized light, drilled in a ridge from the central unit of the Milne Ice Shelf providing supporting evidence of the texture of glacially fed shelf ice showing grains with even edges which do not interlock, grid lines 1 cm apart (Jeffries, 1985a).

## **Chapter 4 Results**

In this chapter a description of the different ice types is presented. This includes a description of the snow cover and the ice surface characteristics; the ice macrostructure and bulk salinity; the backscatter extracted from each ice core location representing each ice type; the general description and interpretation (surface condition survey) of the Milne Ice Shelf; and the statistical relationship between the ice type properties and the 2013 SAR backscatter. The list of ice cores extracted across the Milne and Petersen ice shelves (2012-2013) is found in Table 4.1. In presenting the results, it was sometimes useful to distinguish Type B as originating from either Petersen Ice Shelf (subtype Bp) or Milne Ice Shelf (subtype Bm).

### **4.1. Surface condition survey**

The RADARSAT-2 imagery of both the Milne Fiord and Petersen Ice Shelf showed variability in backscatter that can be explained by the survey of surface conditions. The Milne Fiord SAR transect traversed three major ice types, while the Petersen Ice Shelf transect only traversed one ice type (Figure 4.1). The surface conditions along the Milne Fiord transect ranged from smooth and flat ice across the region occupied by ice type C, rough across ice type B, and rough in ice type A. The surface conditions on the Petersen Ice Shelf within the study region were gently rolling ridges and troughs with and rough surface similar to the ice and surface across ice type B.

The survey results explained much of the local variability along the SAR backscatter transect. Ice type A was represented by a bright SAR signature with a linear pattern

perpendicular to the transect associated with surface undulations. Areas with extremely bright returns (Figure 4.2A, yellow square) were associated with cracks (Figure 4.2C) and troughs viewed from the surface conditions survey transect. A crack across the Milne Ice Shelf from northwest to southeast is represented by a darker SAR return due to the sea ice formed in the crack (Figure 4.2A, green square) (Jeffries, 2002; Mortimer, 2013). Ice type B had a relatively dark SAR signature. The surface of ice type B is very heterogeneous, particularly across the Milne Ice Shelf (Figure 4.2E, F). According to the surface condition survey results, the areas with brighter SAR returns are within areas with many fractures or surface debris (Figure 4.1B (black arrows) & 4.2A, pink and orange square). The surface condition survey did not reveal any notable changes across the flat region with ice type C. The April 27, 2013 SAR image clearly shows a large circular region in the middle of this area with uniformly dark signatures. This was surrounded by a region with a uniformly bright signature (Figure 4.2A, red square; Figure 4.2G). This difference was not visible in the April 17, 2012 SAR image.

#### **4.2. Snow cover and ice surface**

In May 2013, the mean snow thickness across ice type A was 38 cm, while in July the snow thickness varied between 20 and 30 cm. The snow profile consisted of a basal layer of low density depth hoar crystals overlain by wind-blown snow. The ice surface was fractured with grooves up to 6 cm wide and 8 cm deep (Figure 4.3A), which was considered to be rough according to the Rayleigh criterion. The areas surrounding the ice type A sample sites were classified as homogenous.

Ice type B sample sites had a mean snow thickness of 36 cm (Milne Ice Shelf: 31 cm; Petersen Ice Shelf 46 cm) in May 2013, while in July 2013, the snow thickness ranged from 0 to 12 cm (Milne Ice Shelf only). The snow profiles for ice type B sample sites were similar to ice type A. The ice surface across type B on the Milne Ice Shelf was similar to ice type A, while the Petersen Ice Shelf core sites also had similar ice conditions from ice type A and C. According to the Rayleigh criterion, the type B ice surface was rough. The local topography surrounding ice type B sample sites was homogeneous in spite of the heterogeneity across much of this ice type.

The May mean snow thickness at ice type C core sites was 60 cm, and roughly 0-12 cm in July. The snow profiles in May 2013 revealed a loose granular layer in place of the depth hoar observed for the other ice types. The ice surface was smooth at all three core sites according to the Rayleigh criterion (Figure 4.3B). The ice surface at site C1 was consistent with the morphology of refrozen candle ice, whereas sites C2 and C3 had relatively smooth surfaces (Figure 4.3C). All sample sites in ice type C had a homogeneous surface topography

### **4.3. Ice structure**

The different structures that can be found within the ice can be used to differentiate ice types (Ragle et al., 1960). The structures described here are bubbles, sediment layers, brine channels and fractures (Figure A, Appendix). Sediment layers, brine channels and fractures were only found in a limited number of samples, whereas bubbles were found in every core sample. The ice cores of ice type A had a cloudy appearance due to an

abundance of very small (<1 mm) bubbles found throughout (Figure 4.4). Clusters of rounded bubbles, layers of lenticular bubbles (consisting of rounded clusters of bubbles) and occasionally elongated bubbles were found throughout the length of the cores. Sediment layers were found within some of the deeper segments of each ice core (Figure F1). For example, A1 and A2 sediment layers were found at the surface and at ~100 cm, while in core A3, sediment layers were found at 0-1, ~60 and 140 cm. The ice structure in the top first 45 cm of core A3 was different from A2 and A1. The ice was clear in this sample, with a different bubble structure compared to A2 and A1, such as rounded bubbles at the surface followed by elongated bubbles with rounded bubbles. The remainder of core A3 was similar to the other samples in ice type A. Ice type A had small bubbles which varied somewhat horizontally but were consistent in size vertically (Table 4.2, Figure 4.5). Ice type A also had the largest bubble concentration among all ice types (Table 4.2, Figure 4.5). The aspect ratio of the bubbles was near one and relatively invariant, indicating symmetrical, round bubbles. Fractures were found within two of the three ice cores (A1 & 3) and only near the bottom of the 2 m cores.

Ice type B samples differed markedly based on their provenance (Bp and Bm). Samples of type Bm did not have an abundance of tiny bubbles throughout, but had either a clear (e.g., B1) to somewhat cloudy (e.g., B2) appearance caused by a larger abundance of tiny bubbles (Figure 4.4), however not to the extent of type A. Type Bp contained elongated inclusions, which did not occur in type Bm samples. These inclusions had a marked resemblance to brine pockets (Eicken & Lange, 1989). Sediment layers were visible in ice type B, however they were only in the top 15 cm (B1 and B2) and 30 cm (B3) of the

cores (Figure F1, Appendix). The bubbles in ice type B were smaller than the other two ice types (Table 4.2) and more numerous than in ice type A. The bubble aspect in type B cores was more varied than in ice type A, yet still indicated a relatively symmetrical shape. Fractures were limited and only found at the ice surface of core B2.

Ice type C was relatively clear, which made it easier to view the bubble properties. There was a presence of elongated bubbles which varied in size. Core C3 was extensively broken, meaning that visual interpretation of the structure was impossible. Both C1 and 2 were clear throughout (Figure 4.4); however, C1 was heavily populated with a large diversity of bubbles ranging in size from 1-20 mm wide to 20-120 mm long, whereas C2 contained only a few bubbles. There were no sediment layers present in any of the ice cores extracted from ice type C, and neither were there any fractures. Ice type C had the largest bubbles, both vertically and horizontally, but also had the fewest bubbles. The bubble aspect ratio was greater in ice type C than in ice types A and B, which is indicative of elongated bubbles. Type C cores were all shorter than the nominal 2 m core lengths taken at the other sites C1, C2 and C3 were 112, 73 and 74 cm long, respectively. Although the bubble diameters were not significantly different between each ice type (due to high variability in ice type C), they were easily distinguishable with a visual inspection (Figure 4.4).

Figure 4.5 provides visually a general pattern of the bubble structure for each ice type. The pattern shows that bubbles in ice type A, and B are rounded and don't deviate much in size (with the exception of core B3, which has more variability in bubble size,

especially vertically), while ice type C are more elongated and variant in size. Furthermore, ice type B was statistically found to have the smallest average bubble diameter; however it can be seen that they varied more in size (due to the Petersen Ice Shelf sample), than ice type A, which overall had the smallest bubbles. While statistically the bubble diameters were drawn from the same population ( $p$ -value  $>0.4$  for all the bubble variables), visually it is possible to differentiate the bubbles from each ice type due to the overall shape and formation which were significantly different (Figure 4.4).

#### **4.4. Salinity and temperature**

The average bulk salinity of all three ice cores of type A was  $<0.1$  psu (freshwater ice, with salinity below the limit of detection) (Table 4.2) and was relatively stable throughout the entire length of the cores (Figure 4.6A). The average bulk salinity of the top 2 m of ice type B was 0.28 (SD = 0.47) psu. B1 was fresh to brackish ranging from  $<0.1$  to 0.2 psu, B2 was fresh ice ( $<0.1$  psu), while B3 was more brackish ( $\sim 0.9$  psu; ranging from 0.4 to 1.5 psu) (Figure 4.6B, C). Core B1 was further extracted down to  $\sim 7$  m and the bulk salinity of the segment at 681-696 cm was 0.2 psu. Core B4 on the Petersen Ice Shelf was extracted to  $\sim 13$  m in 2012, and a slushy layer was found at  $\sim 11$  m with an extremely high salinity (79 psu). The first 5 m of this core ranged from  $<0.1$  to 0.5 psu and the  $\sim 5$  to 11 m average bulk salinity was 1.4 psu (range: 0.7-2.3 psu), then below this the average bulk salinity was 2.5 psu (range: 1.1 to 5 psu) (Figure 4.7). Finally, the bulk salinity of ice type C was  $<0.01$  psu throughout. The bulk salinities of the ice types were not significantly different from each other, according to the Kruskal-Wallis test ( $p$ -value: 0.2).

The temperature profiles of ice type A were the coldest and most variable with temperatures between  $\sim -17^{\circ}\text{C}$  and  $\sim -21^{\circ}\text{C}$  (Figure 4.8A). Ice type B had a relatively constant temperature profile and the average temperature was  $-15$ ,  $-18$ , and  $-14^{\circ}\text{C}$  for cores B1, B2, and B3, respectively (Figure 4.8B, C), resulting in an average temperature of  $-15^{\circ}\text{C}$ . The warmest of the ice types was type C, with an average temperature of  $-0.8^{\circ}\text{C}$ . The temperatures were colder at the ice surface and rose towards the bottom of the core sample, reaching  $\sim 0^{\circ}\text{C}$  above the water surface (Figure 4.8D). The results of the Kruskal-Wallis test indicate that the ice types were significantly different from each other ( $p$ -value: 0.03). Based on the boxplot, it is likely that this represents the difference between warmer ice type C and the other ice types.

#### **4.5. Ice texture**

Ice type A had a homogeneous, medium-grained texture of equant-shaped grains (euhedral) and a granular shape, with sharp edges and corners. Most of the grains were equigranular and varied in length from 9 to 12 mm (Figure 4.9). From the surface down to  $\sim 200$  cm the grain diameter increased, with the exception of A1 which varied somewhat down-core but remained relatively the same size (Figure 4.10A). Qualitative observations of regular symmetry and equigranular shape were corroborated by the grain diameter aspect ratio in ice type A (Figure 4.11).

Although ice type B consisted of two sub-types that differed from one another, they both had inhomogeneous grain morphology and ranged more in size than ice type A. Ice type Bm had similarities with type A, but with somewhat different grain morphology. The ice

was inhomogeneous, with a medium to coarse grain texture and subhedral grains with either a granular or tabular shape. The edges and corners of the grains were rounded (Figure 4.9). The grains were inequigranular varying in length from 9 to 17 mm. Grain diameters decreased with depth, from ~17 mm at the surface to ~7 mm at the bottom of the core (Figure 4.10B). The ice extracted from ice subtype Bp was markedly different from the Bm ice samples. The ice grains were inhomogeneous varying from very fine to very coarse, with mixture of euhedral, subhedral and anhedral grain shape and they had granular, tabular and columnar shapes (Figure 4.9). The grains were porphyritic, varying from 1 to ~88 mm in length. The grain diameter also decreased with depth, varying from ~60-80 mm at the surface to 10 mm towards the bottom of the core (Figure 4.10C). The segment from 134-149 cm in core B3 contained the only thin section that had similarities to Bm ice (interlocking grains; Figure 4.12, red circle). In general, the grain aspect ratio of ice type B was relatively variable and B3, which was extracted from the Petersen Ice Shelf, stood out from the Milne Ice Shelf samples of ice type B (Figure 4.11).

The average grain diameters of cores of ice type C were larger and varied far more than the other ice types. The ice grains within core C1 were inhomogeneous and were either euhedral or subhedral. The ice grains in C2, however, were homogeneous and anhedral, due to their very large grain diameter. The ice had a coarse to very coarse grain texture varying from 22 to >88 mm, which was the maximum size of the core width (Figure 4.9). From the surface down to the base of the ice core, the grain diameters became larger, from ~25-30 mm at the surface to >88 mm towards the bottom of the core (Figure

4.10D). Although core C1 showed greater variability in the grain diameter, e.g. smaller at the surface and larger towards the bottom of the core, the general grain aspect ratio were constant (Figure 4.11). The Kruskal-Wallis test indicated that the average grain diameters from horizontal thin sections were different among ice types ( $p$ -value: 0.04). Furthermore, the grain widths from the horizontal thin sections were also significantly different among the three ice types ( $p$ -value: 0.04).

#### **4.6. Backscatter analysis**

Backscatter followed the same general pattern for each polarization and is presented along with the incidence angle for each ice type (Table 4.3 and 4.4). Ice type A had the highest return in VV and HV and ice type C had the highest return in HH. Ice type B had the lowest average backscatter among all polarizations (Figure 4.13, Table 4.3). Ice type B was also more variable than the other ice types (Figure 4.14, Table 4.2). Ice type B areas on the Milne Ice Shelf had somewhat higher backscatter than on the Petersen Ice Shelf (Figure 4.13, 4.14, Table 4.2), which may explain the larger variability for ice type B. Ice type C SAR variables were also variable, generally due to site C2, which had much lower backscatter than the other two sample sites (Figure 3.1). For example, ice type C had a range of.  $\sim 10.8$  dB in  $\sigma^{\circ}_{HH}$  (Table 4.2). Ice type A was the least less variable, within each sample area, (see the standard deviation in Table 4.2) as well as between sample sites (e.g.,  $\sim 3.5$  dB range in  $\sigma^{\circ}_{HH}$  in Table 4.2).

An ANOVA of backscatter was significantly different ( $p$ -value: 0.04) for HV backscatter, marginally significant for HH backscatter ( $p$ -value: 0.07) and non-significant for VV

backscatter ( $p$ -value: 0.1). The co-pol and cross-pol ratios were not significantly different among the ice types; however, the cross-pol H ratio has potential for distinguishing ice type A from the typical high backscatter sites from ice type C. (Figure 4.14).

#### **4.7. Relationship between SAR variables and ice properties**

There were very few significant linear relationships between SAR and ice property variables. Bubble diameter had a significant association with  $\sigma^{\circ}_{HH}$  and  $\sigma^{\circ}_{VV}$ . The co-pol ratio was marginally significant ( $p$ -value: 0.09; Figure 4.15). No significant associations were found between  $\sigma^{\circ}_{HV}$  and ice properties.

Cross-pol ratios (both HH/HV and VV/HV) were also significantly to marginally significantly related to the bubble variables (horizontal and vertical size, aspect, and bubble diameter), and the grain variables from vertical thin sections (grain length and diameter) (Figure 4.15, 4.16). The cross-pol ratio VV/HV also appeared to be related to grain width, aspect and size in horizontal thin sections as well as grain aspect in vertical thin sections (Figure 4.16).

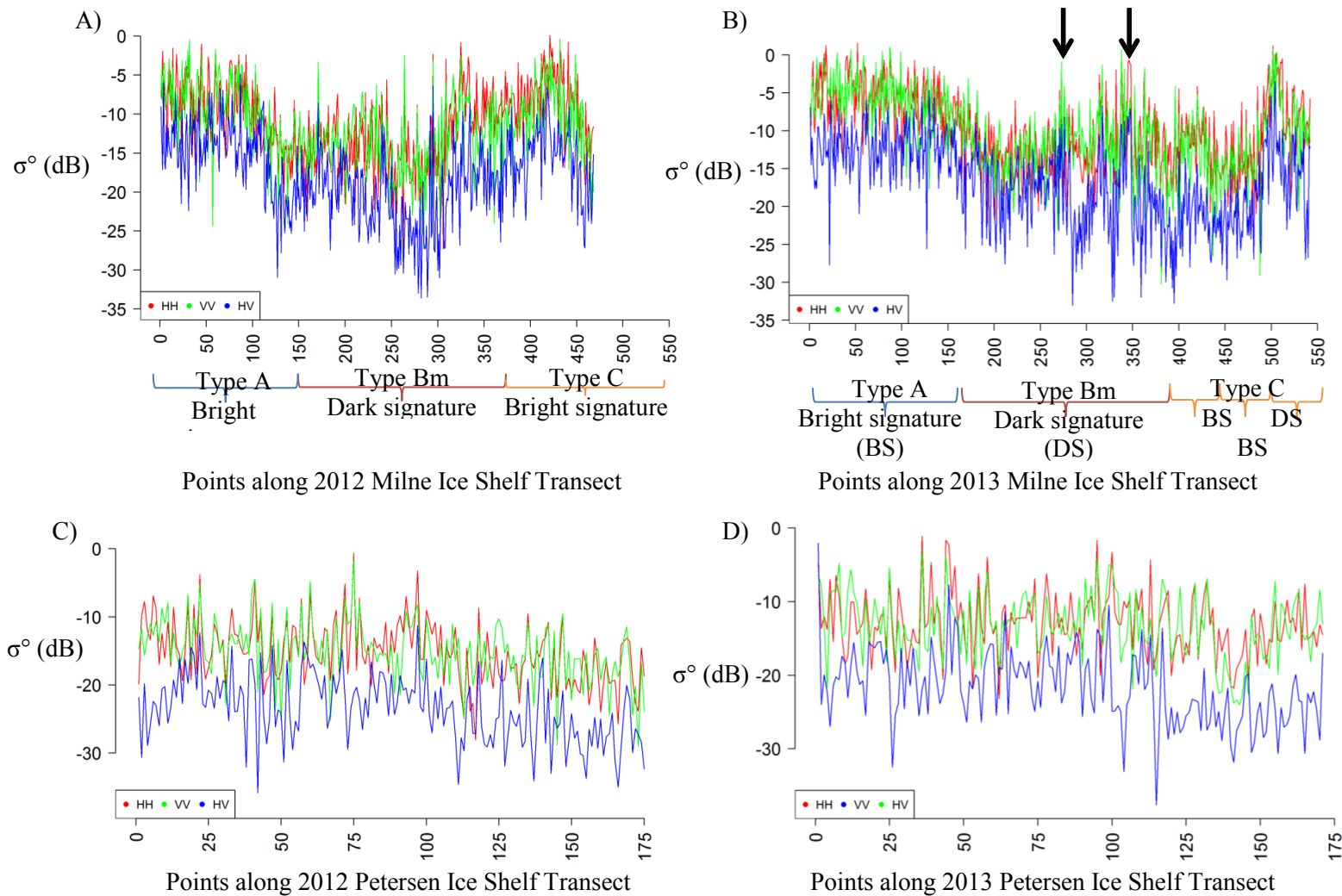


**Figure 4.1:** SAR transects showing the backscatter variability across the different ice types extracted from RADARSAT-2 fine-quad wide beam mode images acquired on April 17, 2012 (A & C) and April 27, 2013 (B & D), respectively. A,B) Milne Fiord transect; arrows indicate areas of higher backscatter (moraine, conical mounds, surface crevassing) across ice type Bm. C, D) Transect along the Petersen Ice Shelf.

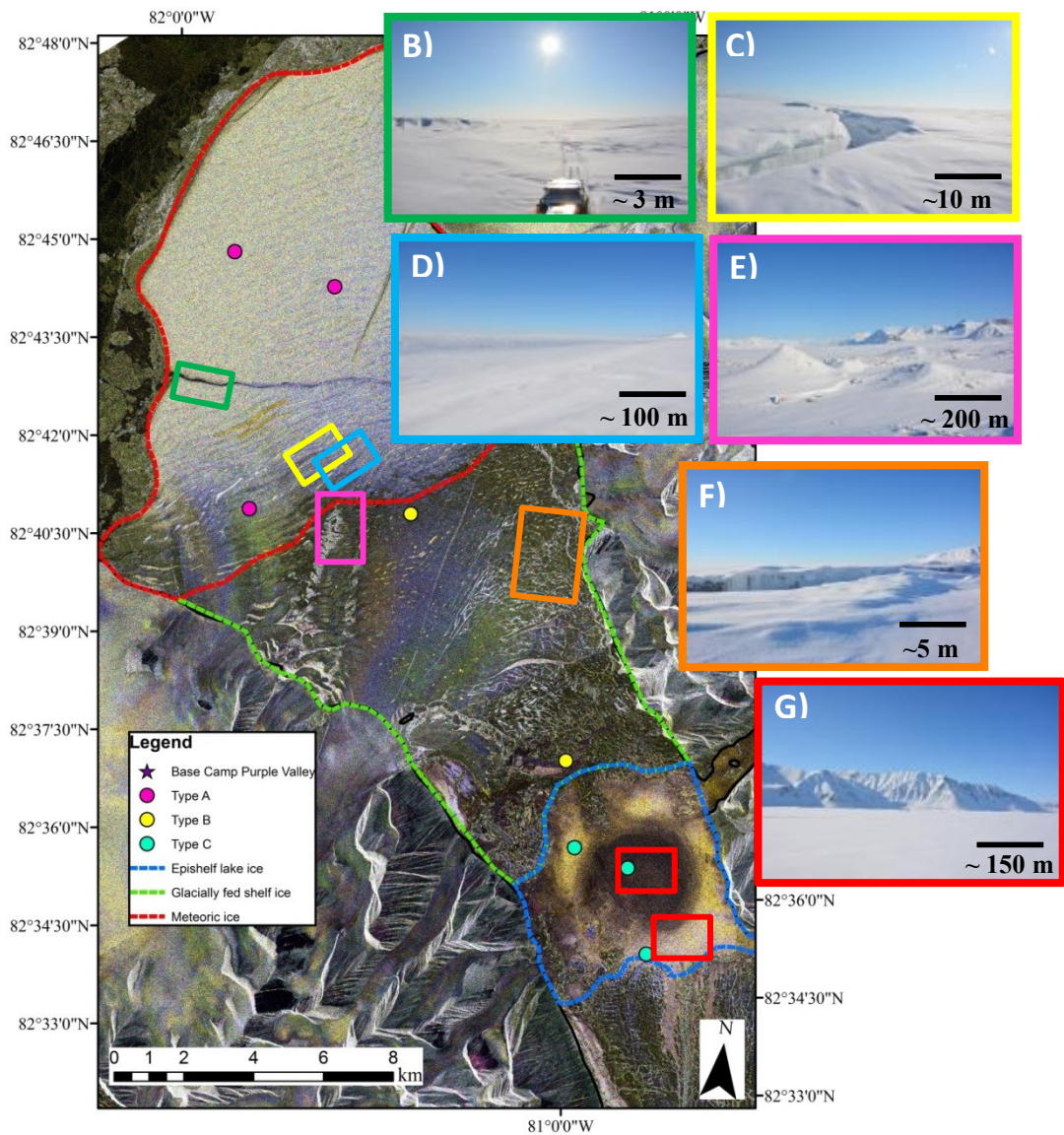


**Figure 4.2:** A) RADARSAT-2 image (fine quad wide beam mode, April 27, 2013) of the Milne Ice Shelf. Red: HH, Green: VV, Blue: HV. B) Photograph of the ice with a dark signature where presumably sea ice is filling a crack in the ice shelf (green square). C) Photograph of one of the numerous extensive cracks found across the ice shelf that has a bright SAR signature (yellow square). D) Photograph of a trough with a dark signature taken from the top of an adjacent ridge (blue square). E) Photograph of moraine material and conical mounds that have a bright SAR signature (pink square). F) Extensive surface fracturing that is associated with lineaments with a bright signature (orange square). G) A smooth ice surface with both a bright and dark SAR signature (red square). RADARSAT-2 image © MDA 2013. Images B-G were taken during the May 2013 fieldwork.

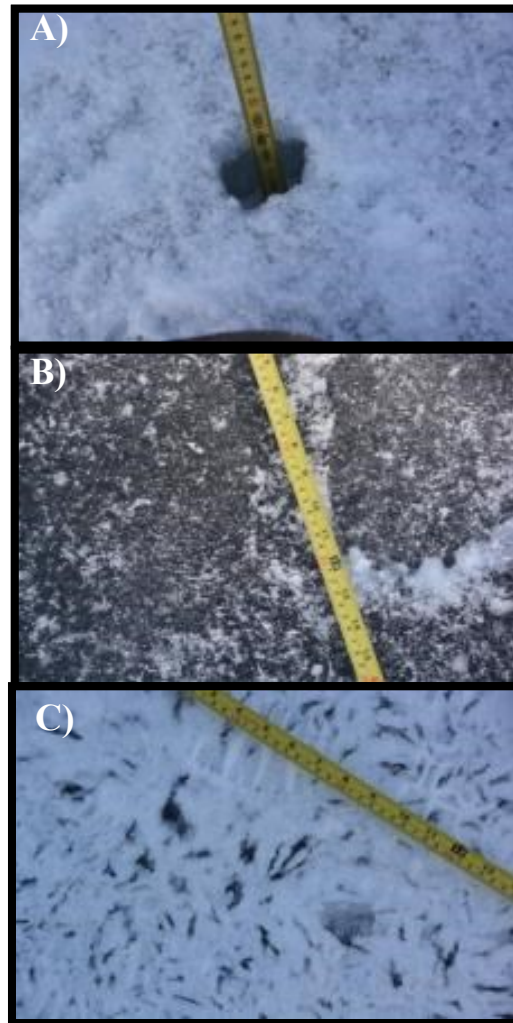


**Figure 4.3:** Images of the ice surface A) Ice surface across the meteoric ice found on the outer section of the Milne Ice Shelf showing areas of fractured surface. B) Ice surface across the Milne Epishelf Lake found on the inner section of the Milne Ice Shelf, showing the dark and smooth surface. C) Ice surface across the Milne Epishelf Lake at core site CME3 showing the candle ice surface. Images A-C were taken during the May 2013 fieldwork.

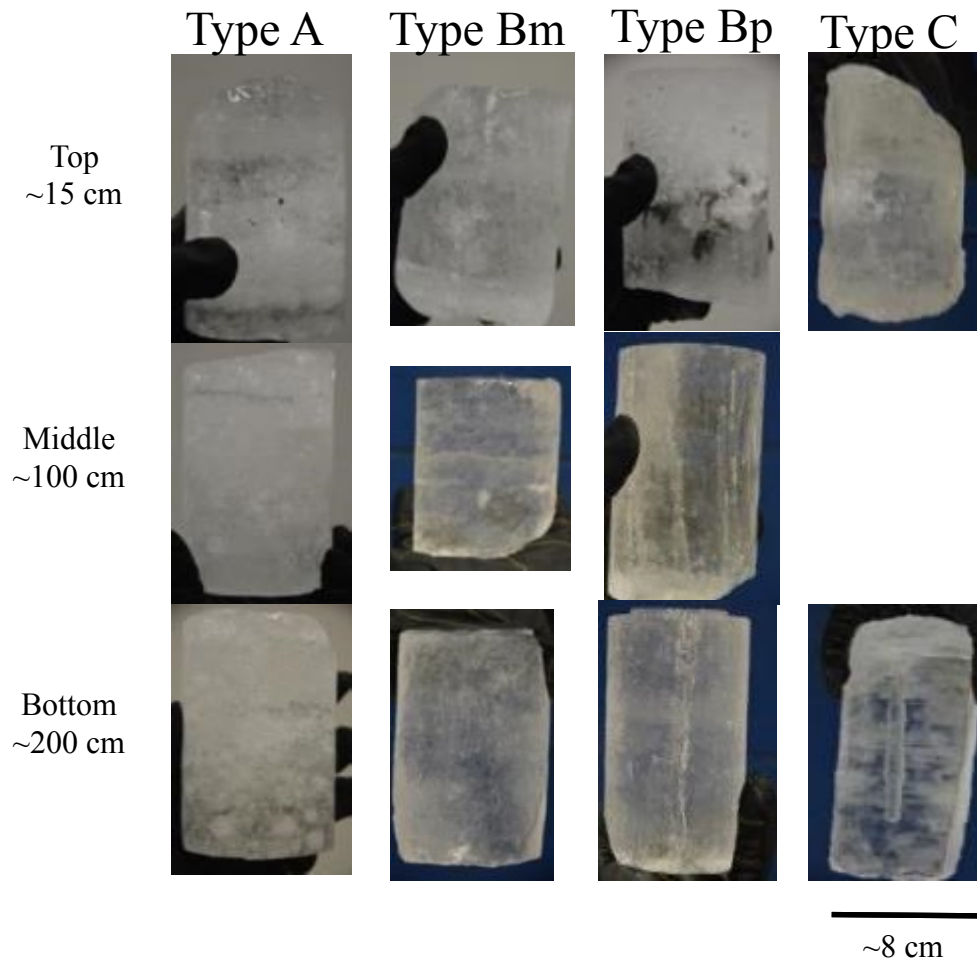


**Figure 4.4:** Ice structures viewed in the field in natural light. Ice type A had a cloudy appearance due to an abundance of tiny bubbles and rounded bubble clusters. Ice subtype Bm had a cloudy appearance and few bubbles, and ice subtype Bp had a cloudy appearance and elongated bubble structures. Ice type C was clear with long elongated bubbles.

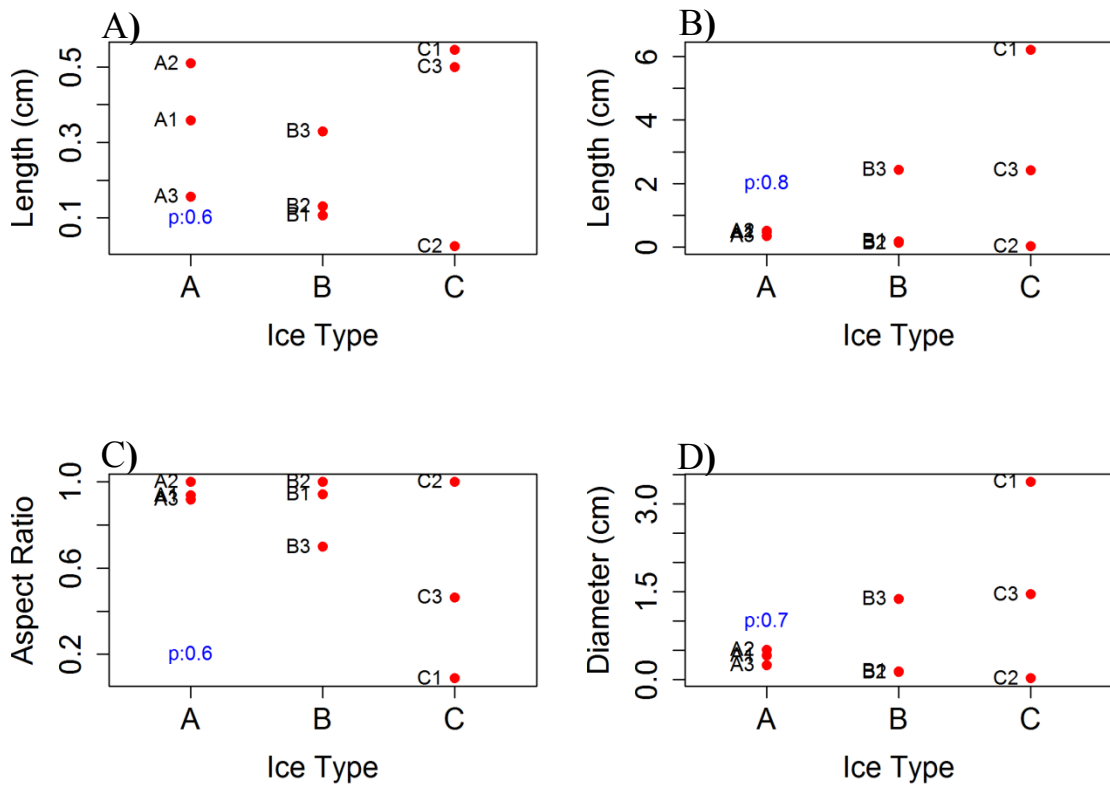


**Figure 4.5:** Boxplot of the bubble dimensions by ice type. A) Horizontal size. B) Vertical size. C) Aspect ratio (horizontal/vertical). D) Bubble diameter. The Kruskal-Wallis test or ANOVA  $p$ -value is listed in each plot.

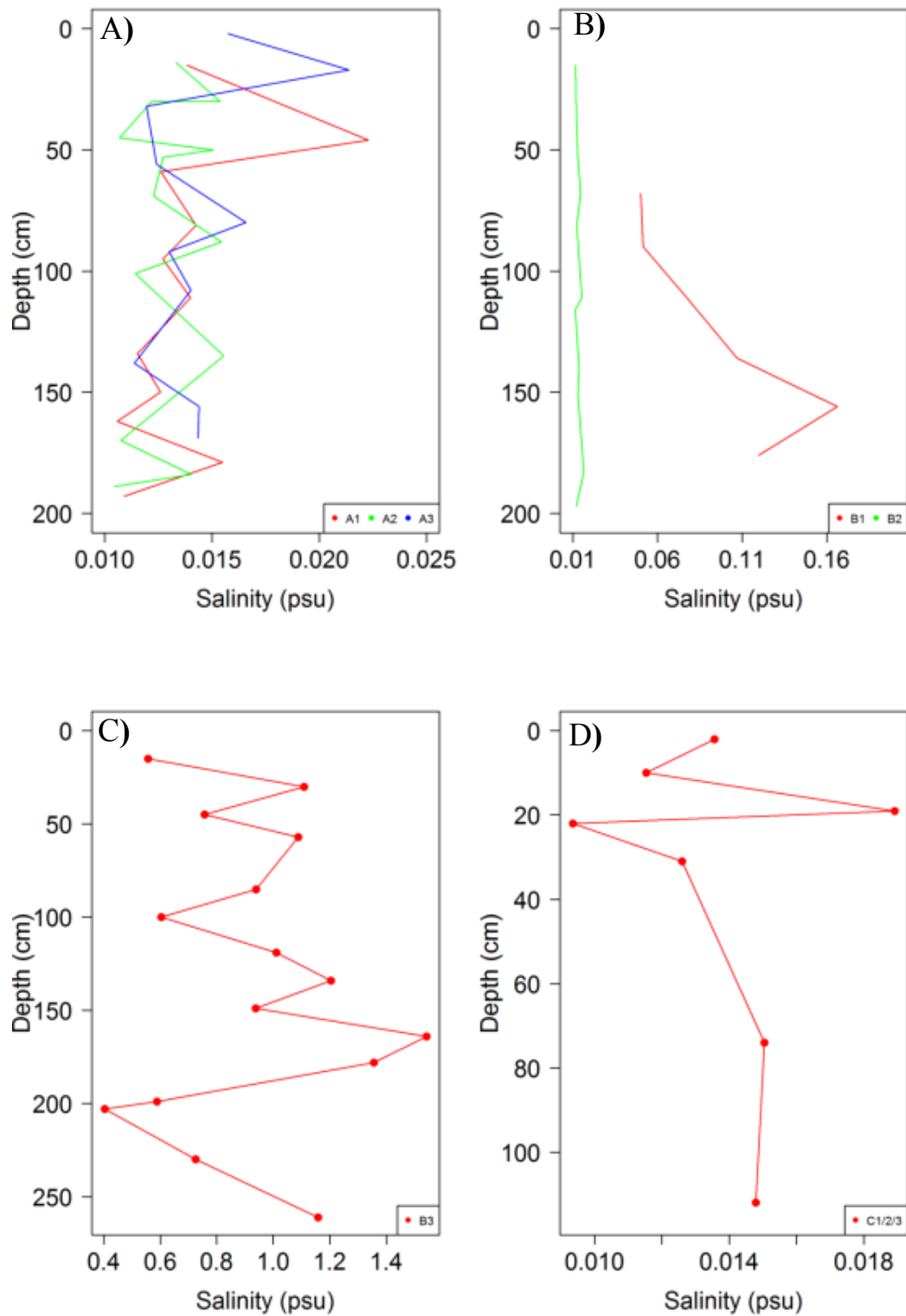


**Figure 4.6:** Typical bulk salinity profiles for each ice type (accuracy of  $\pm 0.1$  psu). A) Type A. B) Type Bm. C) Type Bp. D) Type C. Because ice type C did not have many salinity profiles taken all three cores were plotted into the one profile (each profile are recorded for each ice core extracted).

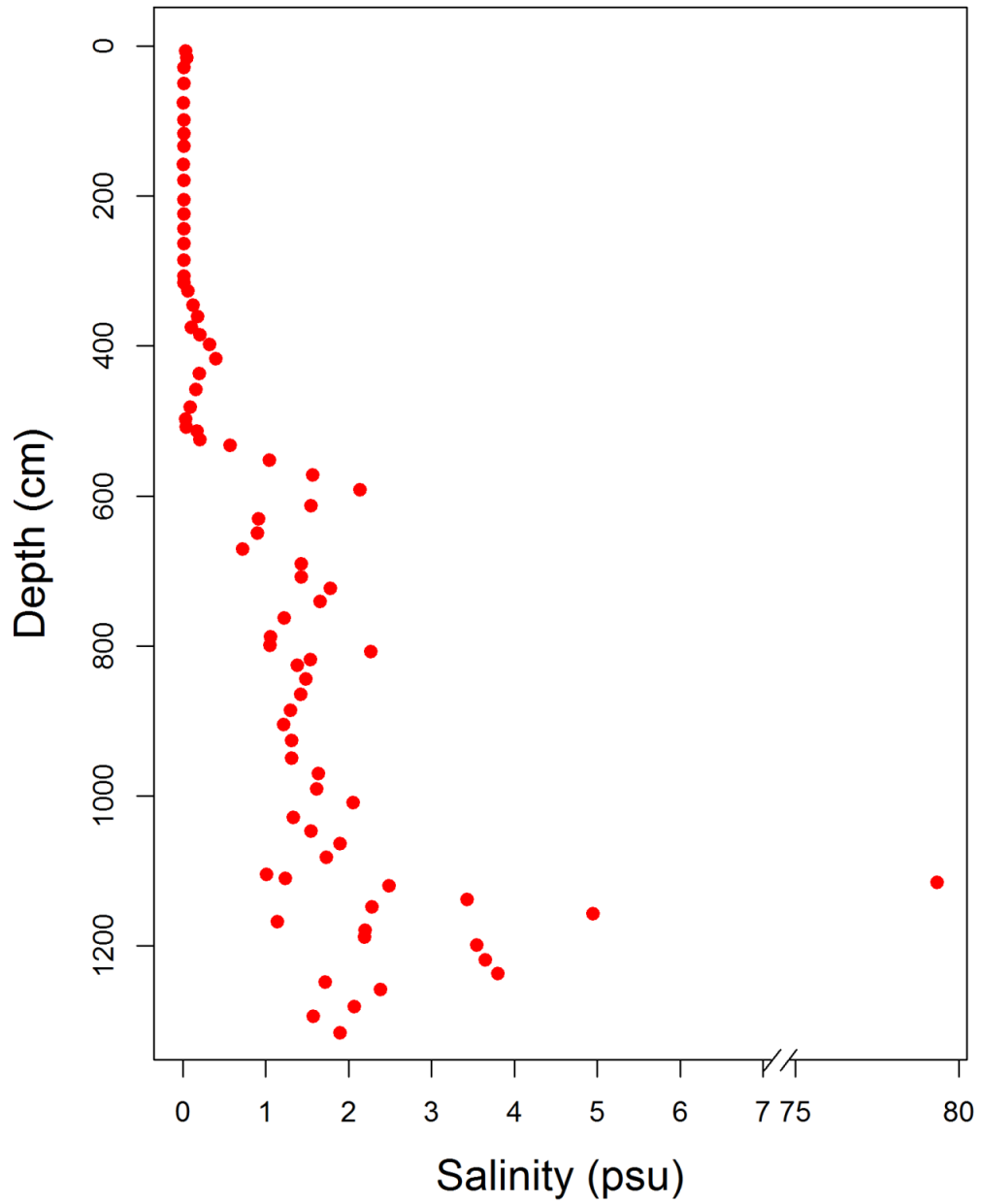


**Figure 4.7:** Bulk salinity profile for core B4 (ice type Bp) with break in the x-axis (Salinity (psu)) at high values.

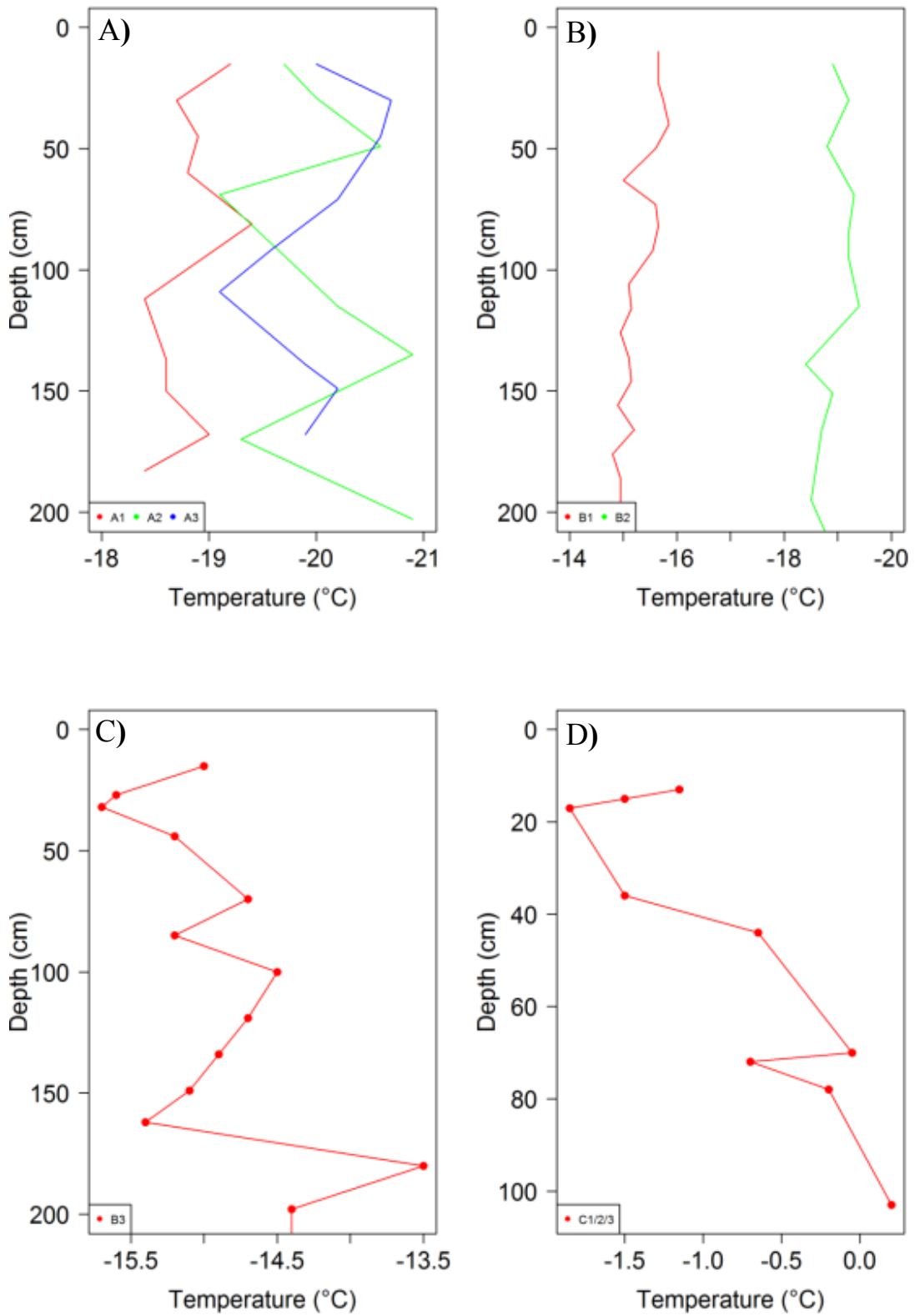


**Figure 4.8:** Internal ice core temperatures taken every ~15 cm (accuracy  $\pm 0.5^\circ\text{C}$ ) during field measurements. A) Type A. B) Type Bm. C) Type Bp. D) Type C. 74

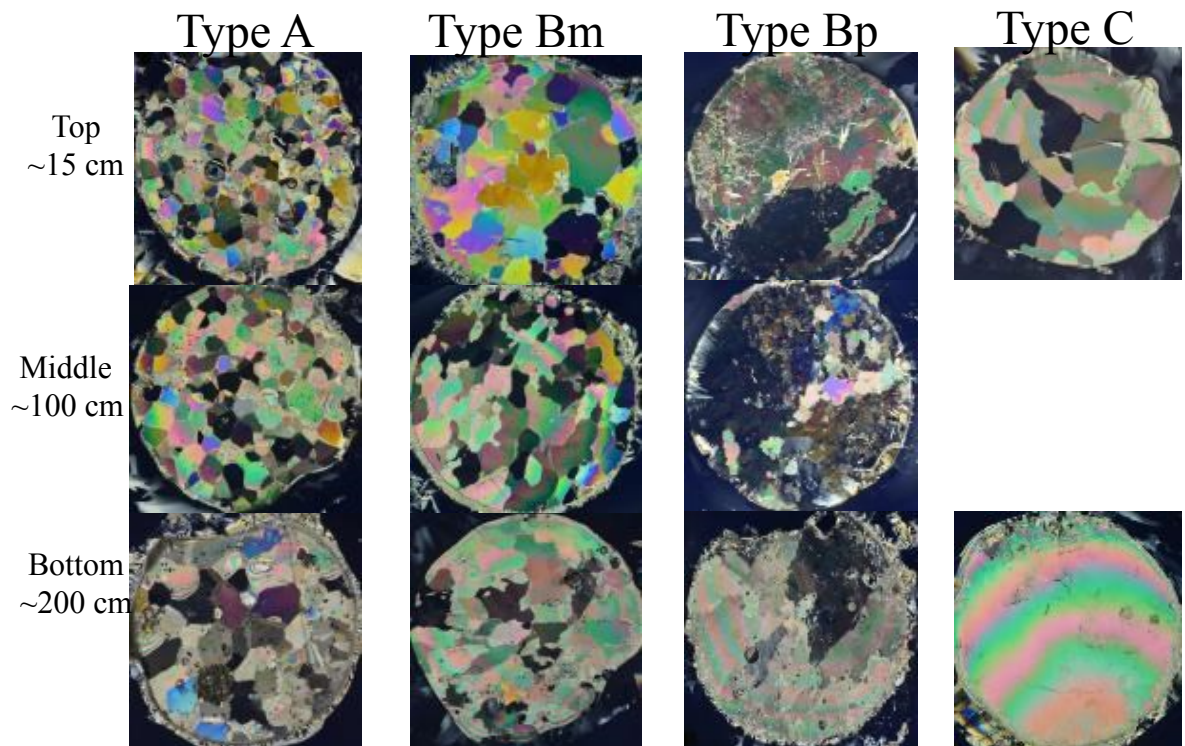


**Figure 4.9:** Typical ice texture for each ice type viewed in polarized light. Ice type A had homogeneous, medium-grained texture of equant-shaped grains (euhedral) and granular, with sharp edges and corners. Ice subtype Bm had an inhomogeneous, medium to coarse grain texture with subhedral grains, a granular and tabular shape, and rounding of the edges and corners of the grains (jigsaw pattern). Ice subtype Bp had an inhomogeneous grain texture varying from very fine to very coarse, with mixture of euhedral, subhedral and anhedral grain shape and had granular, tabular and columnar shapes. Ice type C at the surface had an inhomogeneous texture and was both euhedral and subhedral (top), while at the bottom of the core the ice was homogeneous and anhedral, due to the very large grain diameter.

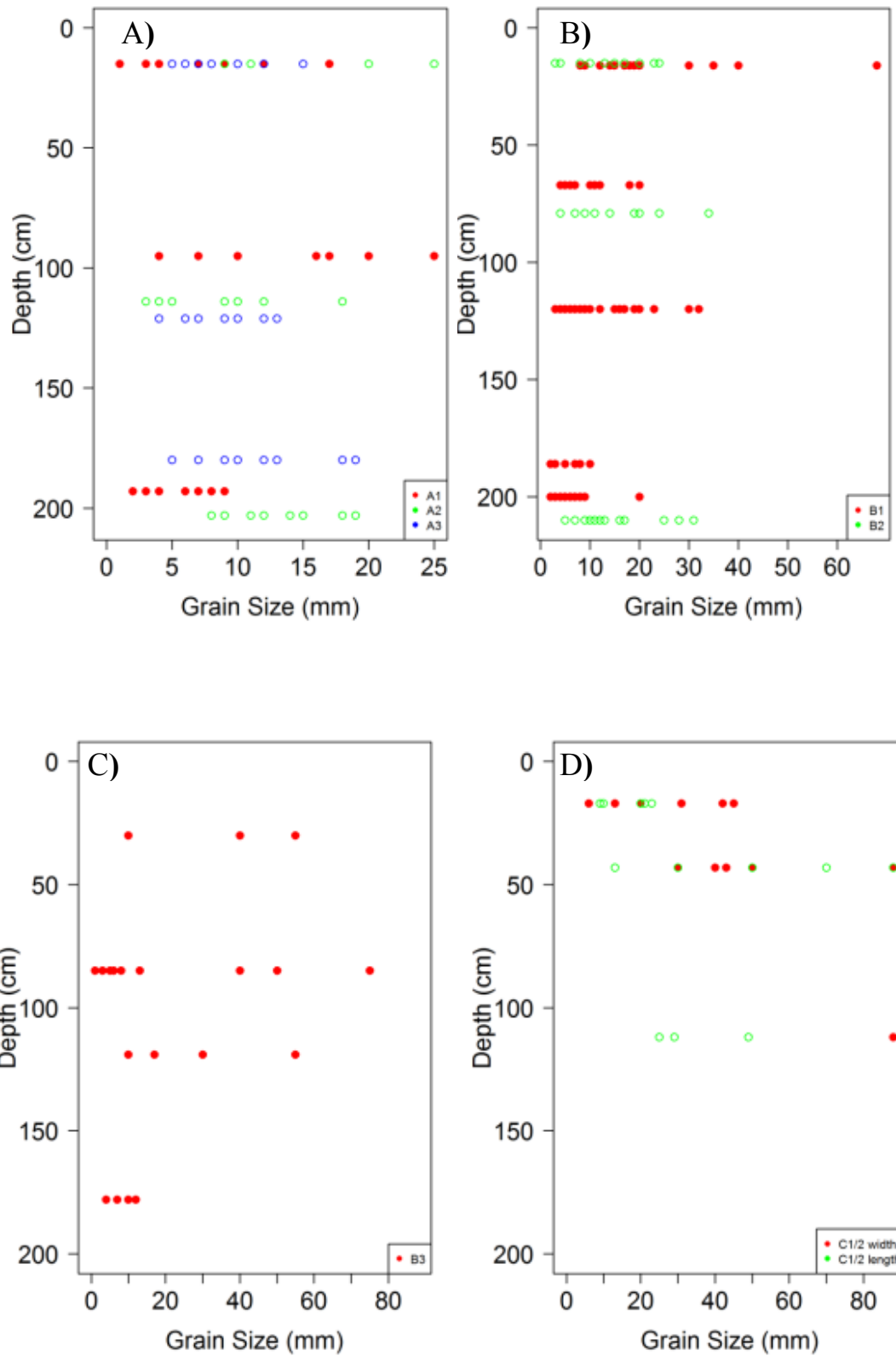


**Figure 4.10:** Grain diameters from laboratory measurements of prepared thin sections between cross-polarized light for each ice type. A) Type A. B) Type Bm. C) Type Bp. D) Type C.

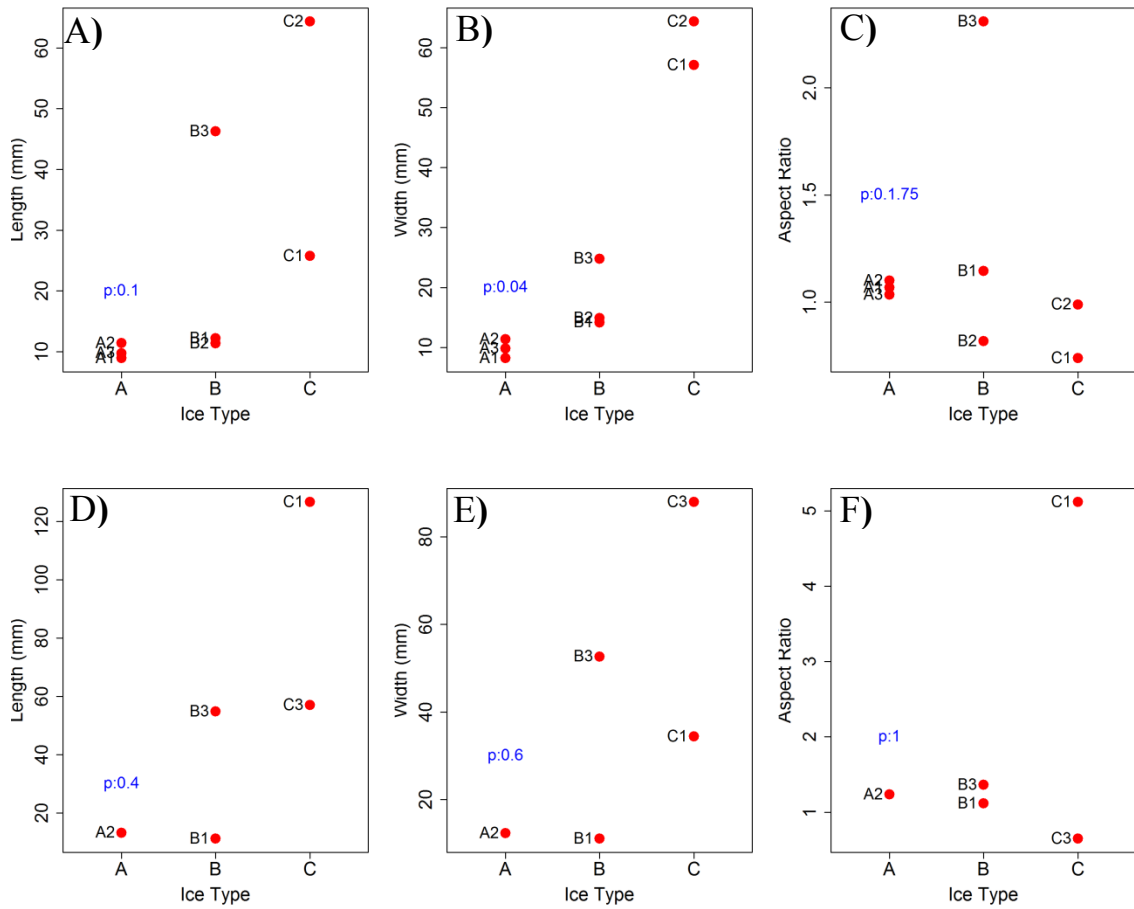


**Figure 4.11:** Boxplot of the grain dimensions by ice type for horizontal (A-C) and vertical (D-F) sections. A, D) Length. B, E) Width. C, F) Aspect ratio (Length/Width). The Kruskal-Wallis test  $p$ -value is listed in each plot.

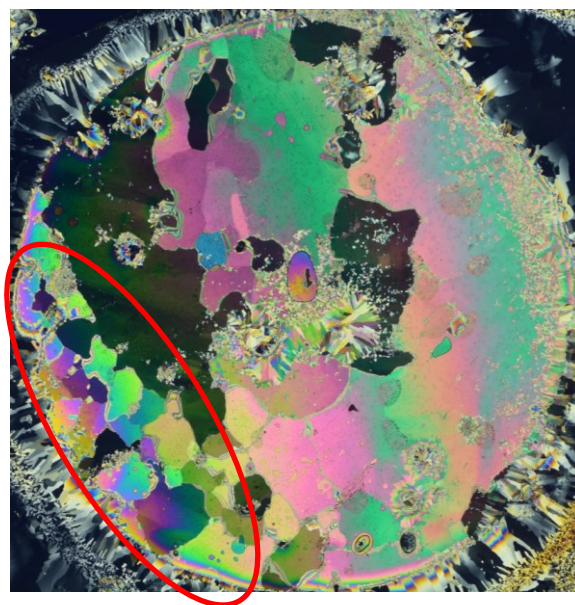


**Figure 4.12:** Ice core segment 134-149 cm from core B3 showing possible evidence of glacier ice texture (Red Circle). However a bulk salinity of 0.94 psu and rounding of the grains implies it is old sea ice (Jeffries et al., 1989).

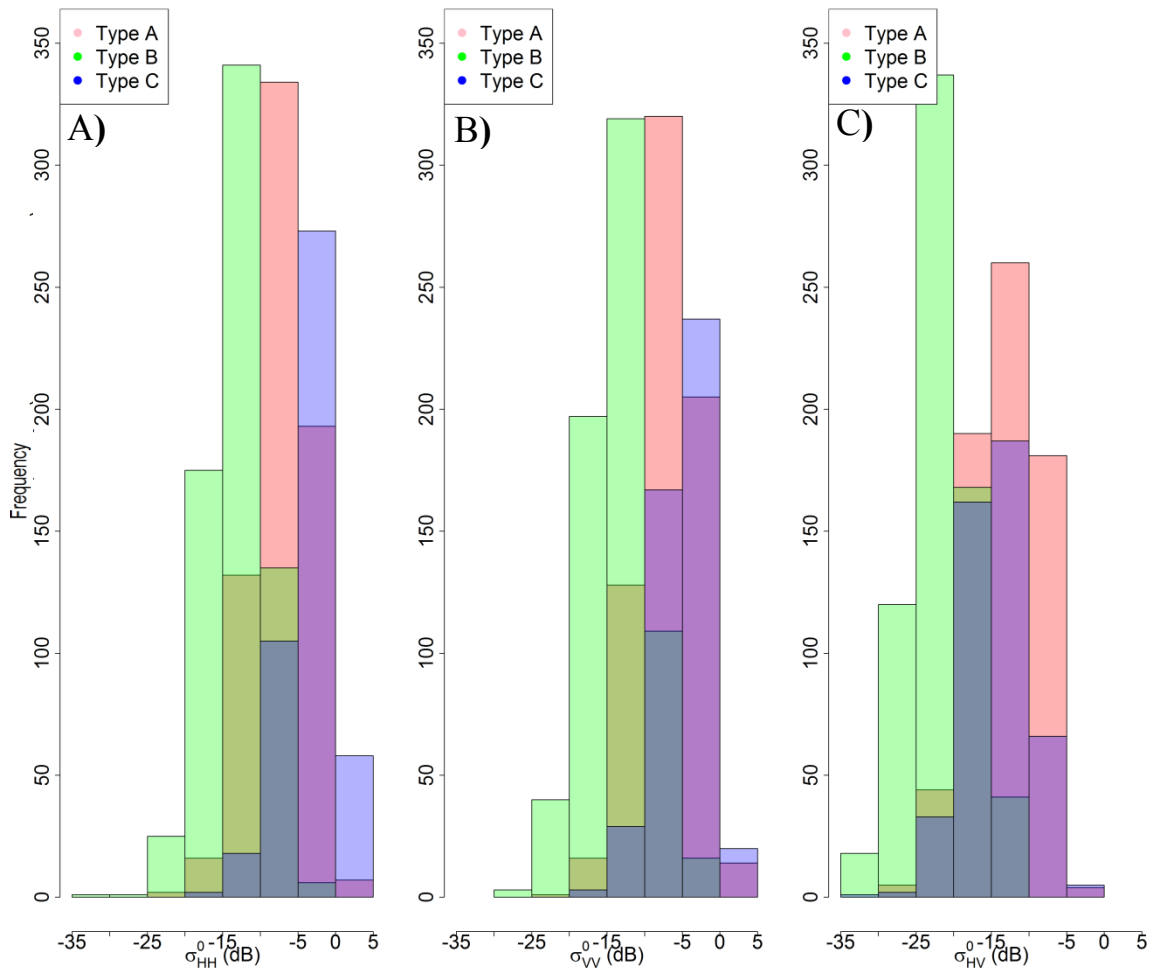


**Figure 4.13:** Histogram of the backscatter by ice type. A-C)  $\sigma_{HH}^{\circ}$ ,  $\sigma_{VV}^{\circ}$ , and  $\sigma_{HV}^{\circ}$ , respectively. Type A (pink), type B (green) and type C (cyan) overlap as follows: both type A & B (dark green), both type A & C (purple), overlap of all ice types (dark blue).

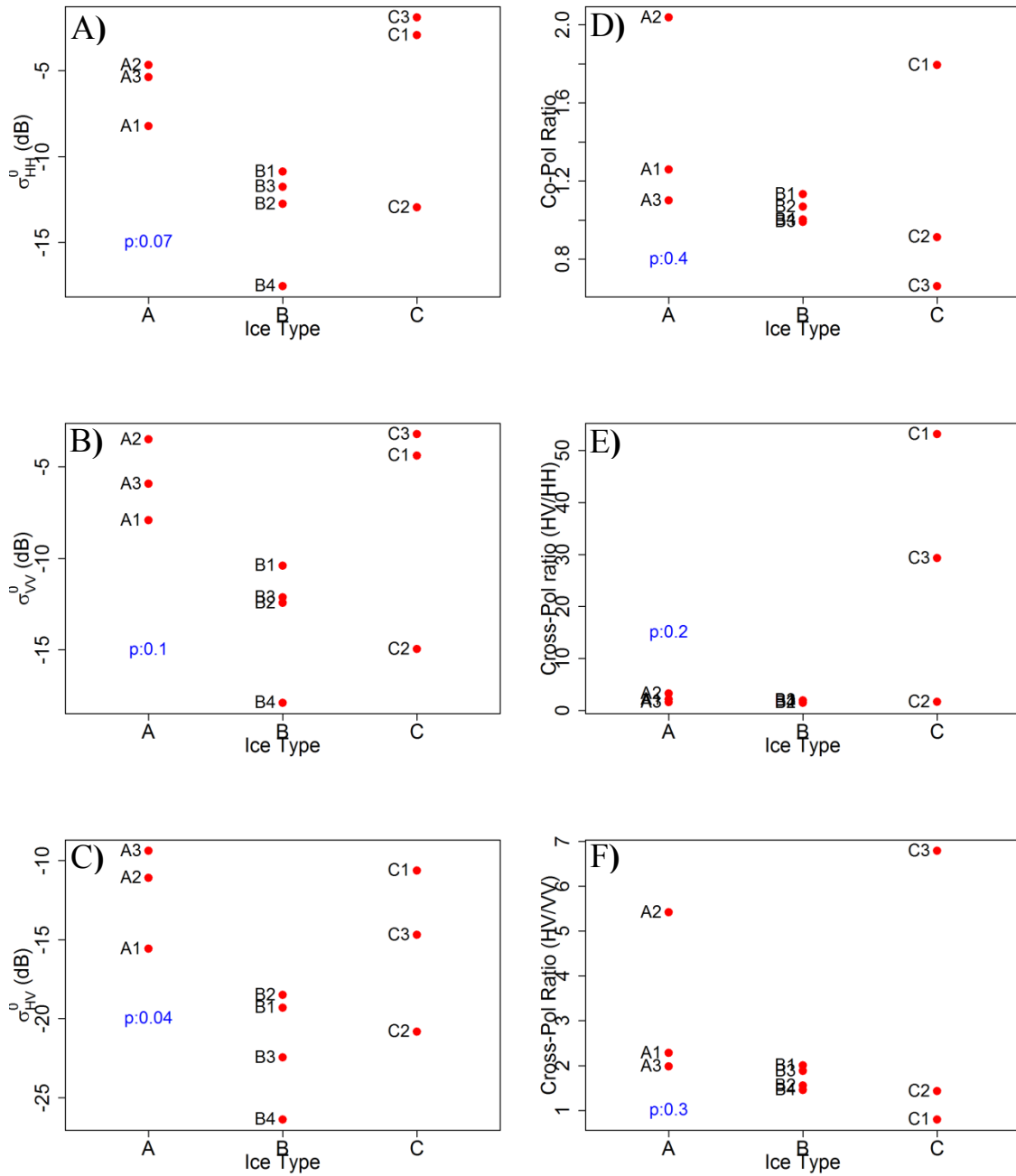


**Figure 4.14:** Boxplot of the different polarization and polarization ratio according to each ice type. A-C)  $\sigma_{HH}^0$ ,  $\sigma_{VV}^0$ , and  $\sigma_{HV}^0$ , respectively D-F) Co-pol ratio ,cross-pol ratio (HV/HH), and cross-pol ratio (HV/VV), respectively. The  $p$ -value from the Kruskal-Wallis Test indicating if each data set is drawn from the same population.

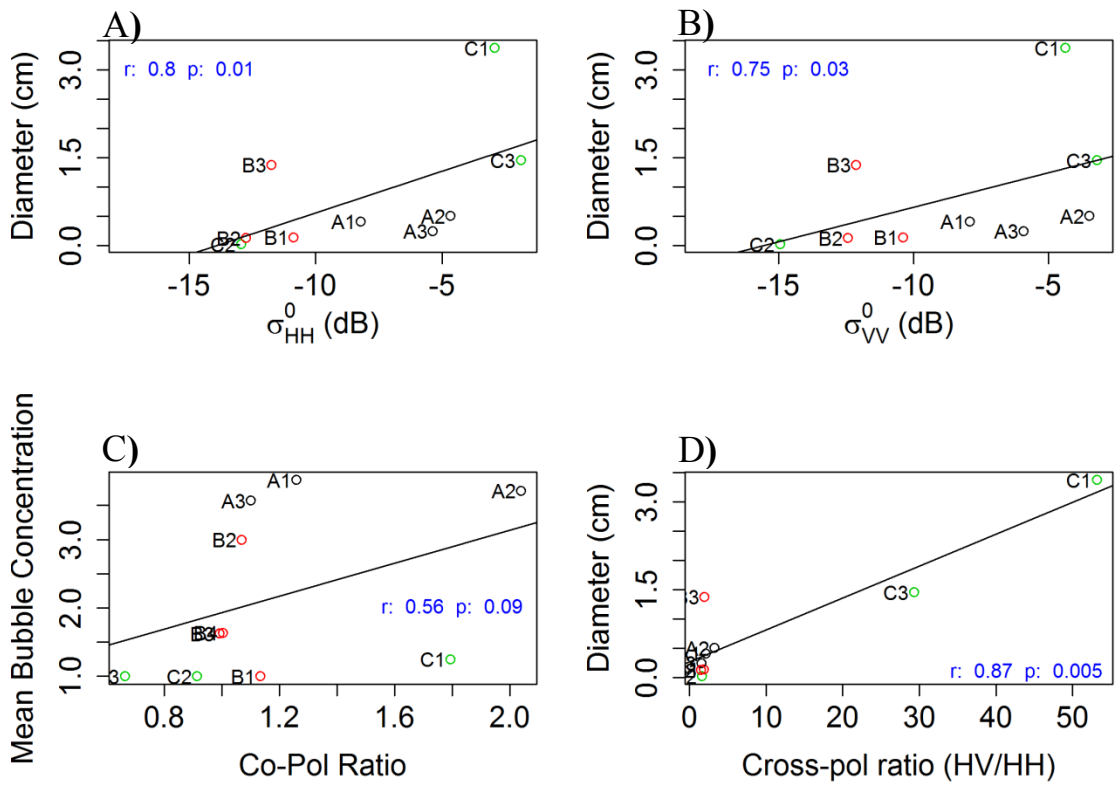


**Figure 4.15:** Relationship between SAR and bubble variables. A) HH backscatter vs bubble diameter. B) VV backscatter vs bubble diameter. C) Co-pol ratio vs bubble concentration. D) Cross-pol ratio (HV/HH) vs bubble diameter. The Spearman  $r$  and  $p$ -value are listed in each scatterplot and a line of best fit is provided.

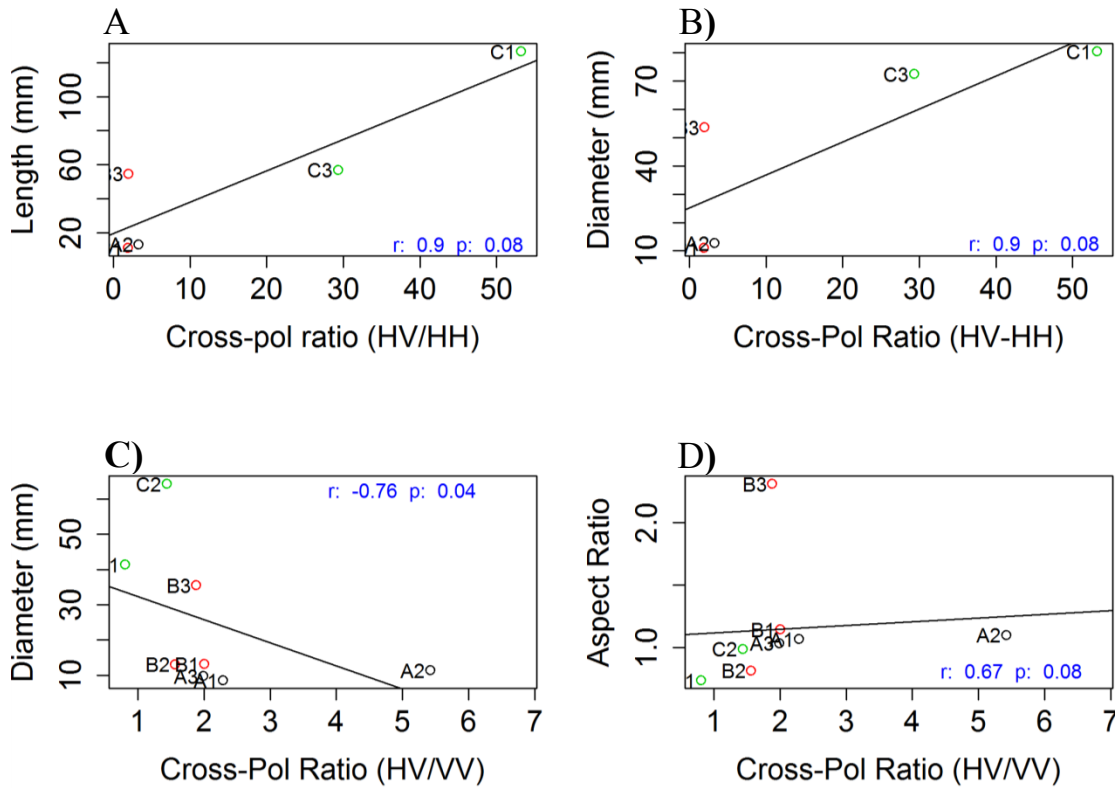


**Figure 4.16:** Relationship between SAR and grain variables. A) Cross-pol ratio (HV/HH) vs grain length from vertical thin sections. B) Cross-pol ratio (HV/HH) vs grain diameter from vertical thin sections. C) Cross-pol ratio (HV/VV) vs grain diameter from horizontal thin sections. D) Cross-pol ratio (HH/VV) vs grain aspect ratio from horizontal thin sections. The Spearman  $r$  and  $p$ -value are listed in each scatterplot and a line of best fit is provided.

**Table 4.1:** Detail of ice cores extracted across the Milne Ice Shelf (MIS), the Milne epishelf lake (MEL), and Petersen Ice Shelf (PIS) in May 2013. Ice core B4 was extracted in May 2012.

<b>Core Name</b>	<b>Core Location</b>	<b>Coordinates (long., lat.)</b>	<b>Ice Core Length (cm)</b>	<b>Depth (cm) of Horizontal Thin Sections</b>	<b>Depth (cm) of Vertical Thin Sections</b>
<b>A1</b>	MIS	-81.755215, 82.686337	193	15, 95, 193	NA
<b>A2</b>	MIS	-81.830151, 82.751005	203	15, 88, 203	15, 88, 203
<b>A3</b>	MIS	-81.629343, 82.746523	180	15, 121, 180	NA
<b>B1</b>	MIS	-81.066353, 82.631021	200	2.5, 57, 120, 696	16, 120, 186
<b>B2</b>	MIS	-81.417312, 82.690019	210	15, 79, 210	210
<b>B3</b>	PIS	-81.559469, 82.501390	261	30, 85, 119, 178	30, 119, 178
<b>B4</b>	PIS	-81.544069, 82.497609	1300	NA	NA
<b>C1</b>	MEL	-80.859536, 82.584267	112	17, 103	17, 103
<b>C2</b>	MEL	-80.912937, 82.605689	73	43, 73	NA
<b>C3</b>	MEL	-81.030108, 82.608819	76	NA	60

**Table 4.2:** Descriptive statistics of the ice properties for each of the ice types sampled in this study.

	<b>Ice Properties</b>	<b>Standard</b>				
		<b>Mean</b>	<b>Median</b>	<b>Deviation</b>	<b>Minimum</b>	<b>Maximum</b>
<b>Ice Type A</b>	<b>Salinity (psu)</b>	0.014	0.014	0.001	0.013	0.015
	<b>Temperature (°C)</b>	-19.6	-20.0	0.7	-20.1	-18.8
	<b>Bubble diameter Horizontal (mm)</b>	0.34	0.36	0.18	0.16	0.51
	<b>Bubble diameter Vertical (mm)</b>	0.44	0.47	0.09	0.35	0.51
	<b>Grain diameter Length (mm)</b>	10.01	9.73	1.27	8.90	11.40
	<b>Grain diameter Width (mm)</b>	9.80	9.83	1.58	8.20	11.37
<b>Ice Type B</b>	<b>Salinity (psu)</b>	0.28	0.06	0.47	0.01	0.97
	<b>Temperature (°C)</b>	-12.9	-15.2	7.3	-19.0	-2.3
	<b>Bubble diameter Horizontal (mm)</b>	0.19	0.13	0.12	0.11	0.33
	<b>Bubble diameter Vertical (mm)</b>	0.91	0.18	1.32	0.13	2.43
	<b>Grain diameter Length (mm)</b>	23.27	12.21	19.91	11.35	46.25
	<b>Grain diameter Width (mm)</b>	17.96	14.90	5.94	14.18	24.81
<b>Ice Type C</b>	<b>Salinity (psu)</b>	0.014	0.014	0.003	0.011	0.017
	<b>Temperature (°C)</b>	-1.1	-1.2	0.2	-1.3	-0.9
	<b>Bubble diameter Horizontal (mm)</b>	0.36	0.50	0.29	0.03	0.55
	<b>Bubble diameter Vertical (mm)</b>	2.89	2.42	3.12	0.03	6.21
	<b>Grain diameter Length (mm)</b>	45.06	45.06	27.31	25.75	64.38
	<b>Grain diameter Width (mm)</b>	60.73	60.73	5.16	57.08	64.38

**Table 4.3:** Descriptive statistics of the SAR backscatter (April 27, 2013) for each of the ice types sampled in this study

<b>Polarization</b>	<b>Ice type</b>	<b>Mean <math>\sigma^\circ</math> (dB)</b>	<b>Median <math>\sigma^\circ</math> (dB)</b>	<b>Standard Deviation <math>\sigma^\circ</math> (dB)</b>	<b>Minimum <math>\sigma^\circ</math> (dB)</b>	<b>Maximum <math>\sigma^\circ</math> (dB)</b>
<b>HH</b>	<b>A</b>	-6	-7	3	-22	2
	<b>B</b>	-13	-14	4	-33	-4
	<b>C</b>	-4	-5	3	-24	3
	<b>Bm</b>	-12	-13	3	-24	-4
	<b>Bp</b>	-14	-15	4	-33	-4
<b>VV</b>	<b>A</b>	-5	-7	3	-23	2
	<b>B</b>	-12	-15	5	-28	-1
	<b>C</b>	-5	-7	3	-26	2
	<b>Bm</b>	-12	-14	5	-28	-1
	<b>Bp</b>	-14	-17	5	-25	-4
<b>HV</b>	<b>A</b>	-12	-13	3	-28	-4
	<b>B</b>	-20	-22	4	-33	-10
	<b>C</b>	-14	-17	4	-37	-2
	<b>Bm</b>	-20	-20	5	-33	-10
	<b>Bp</b>	-22	-24	3	-32	-15

**Table 4.4:** RADARSAT-2 (fine quad wide beam mode, April 27, 2013) incidence angle at each ice core location

<b>Ice Type</b>	<b>Core Name</b>	<b>Incidence Angle</b>
<b>A</b>	<b>A1</b>	33.21
	<b>A2</b>	33.41
	<b>A3</b>	33.53
<b>B</b>	<b>B1</b>	33.45
	<b>B2</b>	33.44
	<b>B3</b>	32.57
	<b>B4</b>	32.57
<b>C</b>	<b>C1</b>	33.39
	<b>C2</b>	33.44
	<b>C3</b>	33.38

## Chapter 5 Discussion

This study has enabled the identification of several distinct ice types across the Petersen and Milne ice shelves, northern Ellesmere Island. Based on the *a priori* classification of the backscatter patterns in a 2012 RADARSAT-2 image and review of previous literature, it was initially thought that there were three ice types:

- (1) Type A, consisting of meteoric ice (*in situ* iced firn), located across the outer section of the Milne Ice Shelf;
- (2) Type B, consisting of glacially fed shelf ice found across the central section of the Milne Ice Shelf and the Petersen Ice Shelf; and
- (3) Type C, consisting of epishelf lake ice located behind the Milne Ice Shelf.

However, when analyzing the structure and textures of ice type B from samples collected in the field, both in natural and polarized light, it quickly became apparent that they differed from glacially fed ice and that their bulk salinity and grain texture characteristics indicate two subtypes. Ice subtype Bm (extracted from the Milne Ice Shelf) was similar to brackish and old sea ice found in the WHIS (Jeffries et al. 1989). Ice subtype Bp (from Petersen Ice Shelf) is consistent with sea ice interleaved with brackish ice.

By utilizing the qualitative data obtained from the structure and texture of field samples, which serve as criteria for distinguishing the different ice types, it was possible to gain greater understanding of the backscatter interactions with the ice. This enables a critical

evaluation of the use of Synthetic Aperture Radar (SAR) satellite imagery (e.g., RADARSAT-2) to identify ice types in Arctic ice shelves.

### **5.1. Ice identification**

Ice type A was found across the outer section of the Milne Ice Shelf. The results from this study showed that ice type A was characterized by having a medium grain texture (~10 mm), which was equigranular, a distinctive structure with lenticular bubble layers, as well as clusters of rounded bubbles, as well as a majority of rounded bubbles. These findings correspond to previous research (Jeffries et al., 1991; Ragle et al., 1964) on iced firn from the WHIS which was recorded as being granular in texture, of medium grain diameter (5-10 mm), showing evidence of stratification of clear ice sandwiched between thin, bubbly ice layers, and containing bubble clusters (Figure 5.1A). Furthermore, the bulk salinity values (<0.1 psu) are also consistent with previous research on freshwater iced firn (Lyons et al., 1971; Jeffries et al., 1988).

Ice subtype Bm, found across the central section of the Milne Ice Shelf, exhibited similar texture to type A; however, there were some dissimilarities. The grain texture varied from medium to coarse (between 5-30 mm), which overlaps substantially with type A, but it also contained a mixture of granular and tabular grains with rounded grain edges and corners which was not observed in type A ice. Although one of the Bm core segments had a few grains that resembled glacier ice (e.g., core B2), there was evidence of interlocking ice grains that resembled the “jigsaw” pattern of interdigitating grains typical of a transition zone (glacier ice with old sea ice; Figure 5.1B), as described by Ragle et al.

(1964). This transition zone ice was typical of the grain texture found within ice type Bm. This implies that ice type Bm is more of a marine ice than a glacial ice type. Research conducted by Ragle et al. (1964) suggested that the rounded grains can be caused by brine migration through younger ice, with concomitant melting of the grain edges until there is sufficient dilution to allow the brine to freeze at the ambient temperature of the ice.

Although previous research suggested that much of the central unit of the Milne Ice Shelf is comprised of superimposed glacier ice (Jeffries, 1985b; Mueller et al., 2006; Mortimer et al., 2010), Jeffries (1985) stated that it does not exclude the possibility of bottom ice accretion or the presence of landfast sea ice in Milne Fiord prior to glacier advances during the formation of the ice shelf. Furthermore, the results from this study make it probable that it is actually composed of stratified basement ice, consisting of both glacier ice and old sea ice.

According to Jeffries et al. (1989), the bulk salinity profiles of sea ice and brackish ice, from ice cores sampled from the WHIS, were 0.08-2.15 psu and 0.03-0.74 psu, respectively. The variability in the salinity profile of core B1 (0.05-0.20 psu) provides evidence of the presence of stratified basement ice (a brackish ice type) in the central section of the Milne Ice Shelf. However, core B2, with bulk salinity of <0.01 psu, did not fall into the brackish/old basement ice category, but rather into the non-saline or glacial basement ice category (Lyons et al., 1971). The frequency distribution of salinity values in brackish ice and old sea ice (Figure 5.2) show that 75% of brackish ice is found in the

0-0.25 psu category, while sea ice occupies all 9 classes, with only 5% in the 0-0.25 psu category (Jeffries et al., 1989). This suggests that the stratified basement ice found in the top 2 m of the central section of the Milne Ice Shelf is likely brackish ice, which is an order of magnitude less saline than the old sea ice (Jeffries et al., 1989). In addition to salinity profiles, Jeffries et al. (1989) provided the first published thin section photographs of brackish ice from the WHIS. These images are similar in texture to the thin sections generated from ice type Bm (Figure 5.1B), with variable grain diameter and shape as well as rounding of the grains (Jeffries et al., 1989; Ragle et al., 1964).

The characteristics of segment 681-696 cm from core B1 provides further evidence that type Bm is a saline basement ice. The texture of this sample was similar to that obtained from thick first-year sea ice from the Alaskan Beaufort Sea near Prudhoe Bay in April 1983 (Tucker et al., 1984) (Figure 5.1B). The heterogeneous mixture of very-fine/fine granular ice and columnar ice, provide further evidence of stratification of the Milne Ice Shelf. The bulk salinity of segment 681-696 cm was 0.2 psu, which is at the threshold between old sea ice and brackish ice samples from the WHIS (Jeffries et al 1989). Because the structural characteristics and salinity profile are similar to those found in old sea ice, a logical conclusion is that the central Milne Ice Shelf is composed mainly of stratified old sea ice with brackish ice. Further confirmation that basement ice has been present across large portions of the Milne Ice Shelf, is the very low reflectivity (less than -30 dB) that were recorded with an 840 MHz pulsed radar system in 1981 (Narod et al, 1988, Figure 5.3). This signal loss was attributed to the presence of brackish ice by Narod et al. (1988) and coincides with core site B2, which had the lowest bulk salinity ( $\bar{x} < 0.1$

psu) of all four cores extracted in ice type B. Ice core B1 had a texture and salinity profile ( $\bar{x}=0.1$  psu) which was not consistent with glacial origin ice, but was found within an area of relatively high backscatter (-10 to -20 dB). This site corresponds with the morphological unit identified by Jeffries (1989) as glacially-fed ice shelf.

Ice subtype Bp (from Petersen Ice Shelf in 2013) differed markedly from subtype Bm. Ice Bp had a mixture of all three grain shapes (granular, tabular, and columnar), which varied from fine to very coarse. Furthermore, when viewing the ice in natural light vertical veins (possible brine inclusions), were visible which were not found in ice type Bm. It is possible that differences between Bm and Bp are caused by the higher salinity found in Bp ( $\sim 0.9$  psu). A CTD profile made adjacent to Petersen Ice Shelf in 2009 showed that surface waters had a salinity of  $\sim 30$  psu in the bay, and that the ice shelf was surrounded by sea ice (White et al., 2015). The salinity profile from the top 2 m of Petersen Ice Shelf (core B3) varied between 0.4-1.5 psu (mean 0.9 psu), which was the highest recorded between all ice types in this study. However, similar to segment 681-696 cm on the Milne Ice Shelf, core B4, of the Petersen Ice Shelf, continued past 2 m and the average bulk salinity was 2.1 psu from 2-13 m depth in this core. In the top 2 m, the bulk salinity profile is consistent with salinity profiles of the alternating layers of old sea ice and brackish ice found in the WHIS (mean  $1.26 \pm 0.65$  psu) by Jeffries et al. (1989). Furthermore, the texture exhibited in core B3 samples is similar to the texture of old sea ice layered in the WHIS (Figure 5.1C), with a mixture of grain shape (granular, tabular and columnar), porphyritic grain diameters varying from fine to very coarse, as well as brine inclusions (vertical veins) (Wadhams, 2000). A detailed analysis of the texture of

core B4 was not possible due to recrystallization following partial melting during storage. This made it impossible to visually determine if the ice consisted of old sea ice and brackish ice. However, the salinity profile of B4 confirmed the presence of these ice types. The top 2 m of core B4 (within this study's sampling frame) had a mean bulk salinity of 0.02 psu; however, the average salinity of the entire core (to a depth of 13 m) was 2.1 psu and the last 2 m of the core had a salinity of >5 psu including a slush layer at ~11 m of 79 psu (Figure 4.7). These results confirm the marine origin of this ice and imply that there is some process that is concentrating salt at depth to exceedingly high levels that are not normally observed (e.g. FYI <1-2 psu, or MLSI <1 to >5 psu; Pope et al., 2012).

Ice type C, which was found behind the Milne Ice Shelf, had the typical structure and texture expected of frozen freshwater lake ice and was considerably different from the remainder of the ice types. Lake ice was identified as having a medium to very coarse grain texture, columnar grains that have straight boundaries, long linear and well-oriented bubbles, and low salinity (Ragle et al., 1964; Jeffries et al., 1991). These characteristics were found in all cores of ice type C. The salinity values of the cores of this ice type were amongst the lowest measured (<0.1 psu), the grain diameter varied from medium to very coarse, there were long columnar straight grains, and elongated bubbles (Figure 5.1D). These results provide sufficient evidence that ice type C was epishelf lake ice. The only exception was core C2, which had some impurities such as small rounded bubbles at the ice surface, but retained typical lake ice characteristics for its other properties.

## 5.2. Radar signature of the ice and SAR visual interpretation

Previous studies have shown that iced firm has a bright SAR signature, probably due to volume scattering (Dierking et al., 1994; Jeffries, 2002), so it was expected that ice type A would also have a high backscatter. Radar penetration into pure ice or slightly impure ice (salinity up to 0.03 psu according to Dierking et al., 1994) is scattered by the multiple air bubbles in the host medium. The average  $\sigma^{\circ}_{HH}$  extracted from ice type A was -6.1 dB. Furthermore, ice type A did have a large concentration of spherical bubbles (bubble clusters) and lenticular layers of tiny bubbles, which would enhance volume scattering of the radar (Figure 4.4). At the same time, its low salinity promotes greater radar penetration. The results presented here corroborate the previous research and also imply that iced firm has a bright signature that is caused by volume scattering against the multiple rounded bubbles found within the host medium. Furthermore, statistical analysis showed that there was a significant association between backscatter and bubble variables in HH and, at times, VV polarizations. The backscatter of ice type A does overlap with the backscatter of ice type C (Figure 4.13). However, the cross-pol ratio HH/HV appears to be a promising way to distinguish these ice types for high backscatter regions of the epishelf lake (Figure 4.14). The technique of identifying different ice types with polarization ratio has proven to be useful for distinguishing multiyear ice from rough thin ice and open water (Thomsen et al., 1998).

Glacier ice, which consists predominantly of freshwater ice, should exhibit a higher backscatter than more saline ice types (Jeffries, 2002). Although analysis was not conducted on glacier ice, this assumption is based on the fact that freshwater ice allows

deeper microwave penetration and volume scattering (Jeffries, 2002). For example, Cape Evans Icefield, which is adjacent to both the Milne and Petersen ice shelves, has an average  $\sigma^{\circ}_{\text{HH}}$  of -5 dB, which is similar to iced firn (ice type A). This corroborates the interpretation that iced firn is derived from meteoric input (Mueller et al., 2006). However, there are other regions with glacier ice that do not exhibit the same bright SAR signature as iced firn and nearby ice fields. The average  $\sigma^{\circ}_{\text{HH}}$  of the terminus of the Milne Glacier was -12 dB and several glacier termini that merge with the Milne and Petersen ice shelves, had mean  $\sigma^{\circ}_{\text{HH}}$  of -10 dB and -9 dB, respectively (Figure 4.2A). These lower backscatter values may be related to the debris-rich surfaces of the glaciers which would reduce ice penetration and induce surface scattering. For example, the conical mounds and moraines near the glacier terminus from the central unit of the Milne Ice Shelf had a mean  $\sigma^{\circ}_{\text{HH}}$  of -10 dB. This is a similar signature to type B ice which also has sediments on the surface and uppermost 30 cm of ice (Figure 5.4). However, the backscatter of type B ice is significantly lower than the backscatter on debris glacier termini and this is likely due to the difference in salinity between glacier ice (which must be very low salinity) and the brackish and old sea ice identified in type B. It is also plausible that the radar penetrates deeper into the ice volume and becomes absorbed by even more saline ice below.

The epishelf lake ice (ice type C), from cores C1 and C3, had similar radar return values with an average of -2.9 dB and -1.9 dB ( $\sigma^{\circ}_{\text{HH}}$ ), respectively. These results fall above the -6 dB threshold that indicates the presence of an ice-dammed lake (Veillette et al. 2008; White et al., in revision). However, the backscatter from core site C2 was well

below this threshold with an average  $\sigma^{\circ}_{\text{HH}}$  of  $-12.9$  dB, which is uncharacteristic of ice-dammed lake ice. In spite of this, the ice texture and salinity of C3 were consistent with lake ice (long columnar grains and a salinity of  $<0.1$  psu). CTD measurements in the water column beneath ice type C indicate that the halocline was at a depth of 8.04 m in May 2013, which is close to what it was in 2012 (Hamilton et al., unpublished). Therefore, the depth of the epishelf lake cannot explain the discrepancy in SAR signature between the three sites in ice type C. Furthermore, Veillette et al (2008) recorded haloclines at depths of 2 to 5 m on northern Ellesmere Island (in Serson Bay, Taconite Inlet, Ayles and Markham Fiord) which were associated with high backscatter SAR imagery, which corroborates this assumption. C1 and C3 cores had large elongated bubbles throughout whereas C2 did not exhibit bubble development to the same extent. This is likely the reason for the difference in SAR signature, given the lack of double bounce between the vertical bubbles and the ice-water interface (Jeffries 2002), but the ultimate causal mechanism for the lack of bubbles remains unknown.

### **5.3. Relating radar return with ice properties**

Bubble presence, size and shape were associated with  $\sigma^{\circ}_{\text{HH}}$  and  $\sigma^{\circ}_{\text{VV}}$ . Previous research (Dierking et al., 1994; Jeffries, 2002) suggested that bubbles in iced firn caused volume scattering and that elongated bubbles in epishelf lake ice caused a double bounce in conjunction with the ice/water interface (once off the bubbles and then off the ice-water interface, according to Jeffries et al. (1994)), both of which increase backscatter. Accordingly, ice type B and core C2 of ice type C which had fewer and/or smaller bubbles had lower  $\sigma^{\circ}$  values. Low backscatter in ice type B may also be related to other

ice properties. One possibility is that bulk salinity below 2 m may increase and absorb microwave energy that penetrates to this depth. There is some evidence from both the Milne (B1) and Petersen (B3, B4) ice shelves that salinity increases with depth (Figure 4.5 and 4.6) and this is consistent with the presence of brackish/saline basement ice. It is also possible that sediments on or within the ice are absorbing microwave energy. For example, this may be occurring on glacier termini in the region that exhibit low backscatter relative to higher elevation sites. These areas tend to be debris-covered similar to ice type B (Figure 5.4). With the small sample size in this study, a sampling scheme that did not consider ice below 2 m in depth and the lack of quantitative data on sediment concentration, it is not possible to infer which, if any, of these mechanisms may be influencing ice type B backscatter besides bubble properties.

The grain diameter and shape was also associated with SAR variables, in particular the cross-pol ratios. The length and diameter of grains in the vertical thin sections were associated with the cross-pol ratio (HV/HH), while horizontal thin section grain width, aspect and diameter was associated with the cross-pol ratio (HV/VV). Again, this provides greater insight and confirmation that volume scattering is at play and is induced by the double bounce reflection between the vertical, and horizontal, ice texture (Jeffries, 2002).

#### **5.4. Ice shelf structure and origins**

Prior to the extensive ice shelf break-up events from 2005 onwards, three glaciers flowed into the Petersen Ice Shelf which were likely important for its mass balance (White et al., 2015). Similarly, Jeffries (1985), Mueller et al. (2006) and Mortimer et al. (2012) noted

glacier inflow into the Central Unit of the Milne Ice Shelf and concluded that this section of the ice shelf was glacial in origin and that reduced input from glaciers was consequential (Mortimer et al. 2012). The interpretation that glacier inflow is an important contributor to the mass balance of these ice shelves would imply that a large proportion of the two ice shelves must be glacier ice. The results of this study, however, show that there actually may be very little glacier ice in the eastern portion of the Petersen Ice Shelf and across large sections of the Central Unit of the Milne Ice Shelf.

On the Petersen Ice Shelf, only one segment of core B3 (134-149 cm) showed possible evidence of glacier ice texture (Figure 4.10), although this also resembles examples of brackish ice from the WHIS, which has a very freshwater-like appearance. Furthermore, the bulk salinity of this segment was 0.94 psu, which implies it is old sea ice (Jeffries et al. 1989). Based on this new evidence and the very low and infrequent ground penetrating radar return over much of the easternmost Petersen Ice Shelf (White et al., 2015), it is likely that the eastern portion of the Petersen Ice Shelf is composed almost exclusively of old sea ice and brackish ice, not glacier ice.

This new evidence suggests that either glacial ice was, at one point, a dominant ice type but was recently replaced by marine ice or that marine ice has always been a dominant ice type in these regions. The former explanation invokes a rapid increase in surface ablation to enable stratified basement ice to migrate from the bottom of the shelf to the surface. Jeffries et al. (1989) imply that this process might be accomplished over a period of ~400-500 years. There is no way to confirm the latter explanation, except to point out

that the SAR signature of the regions covered by ice type B have been apparently stable since the early 1990s when the first SAR imagery is available (D. Mueller, unpublished). Regardless of the mechanism, these findings suggest that the both the Milne and Petersen ice shelves are composite ice shelves (containing both marine and meteoric ice; c.f., Lemmen et al., 1988b), and cannot be considered only glacial ice shelves, as previously suggested by some studies,, particularly for the Milne Ice Shelf (Jeffries, 2002; Mueller et al., 2006; Mortimer et al., 2012). Furthermore, this would suggest that glacier inflow is localized and may thicken restricted portions of the ice shelves (Mortimer et al., 2012; White et al., 2015), but is not currently contributing significantly to the maintenance of ice shelf thickness. This has implications for the interpretation of ice shelf growth and the long term decline in ice shelf extent due to climate change.

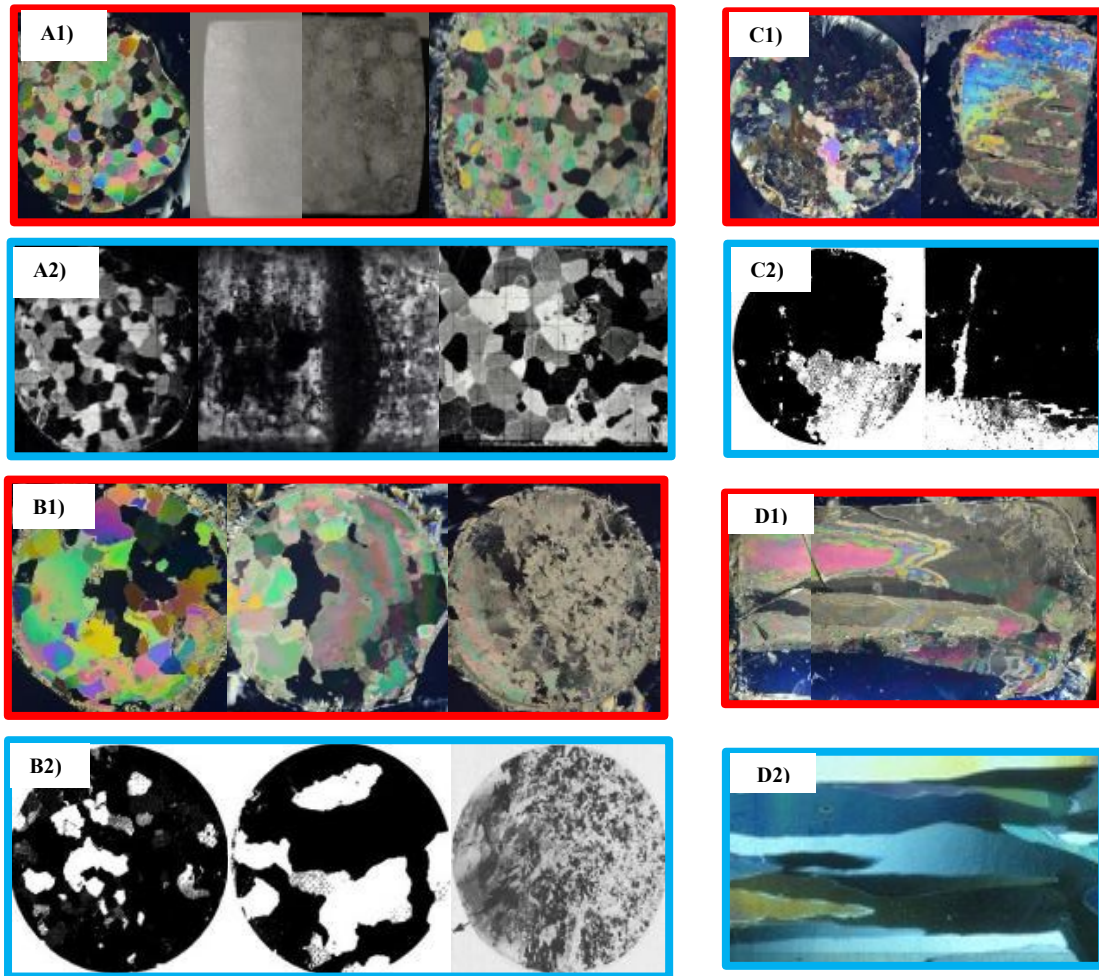


**Figure 5.1:** A1) The structure and texture of ice type A, both in natural and polarized light, consisting of meteoric ice, or iced firn, bottom. A2) Supporting evidence of the meteoric ice structure and texture (Ragle et al., 1964). B1) The texture, in polarized light, of ice type B, from the Milne Ice Shelf (Bm) consisting of brackish and sea ice (marine ice). B2) Supporting evidence of the texture of marine ice (Far left and middle: brackish ice (Jeffries et al., 1989) and far right: FY sea ice (Tucker et al., 1984)). C1) The texture, in polarized light, of ice type B, from the Petersen Ice Shelf (Bp) providing of old sea ice (marine ice). C2) Supporting evidence of the texture of old sea ice (marine ice) (Jeffries et al., 1989). D1) The texture, in polarized light, of ice type C consisting of congelation epishelf lake ice. D2) Supporting evidence of the texture of congelation ice (Alaska Satellite Facility, 2014).

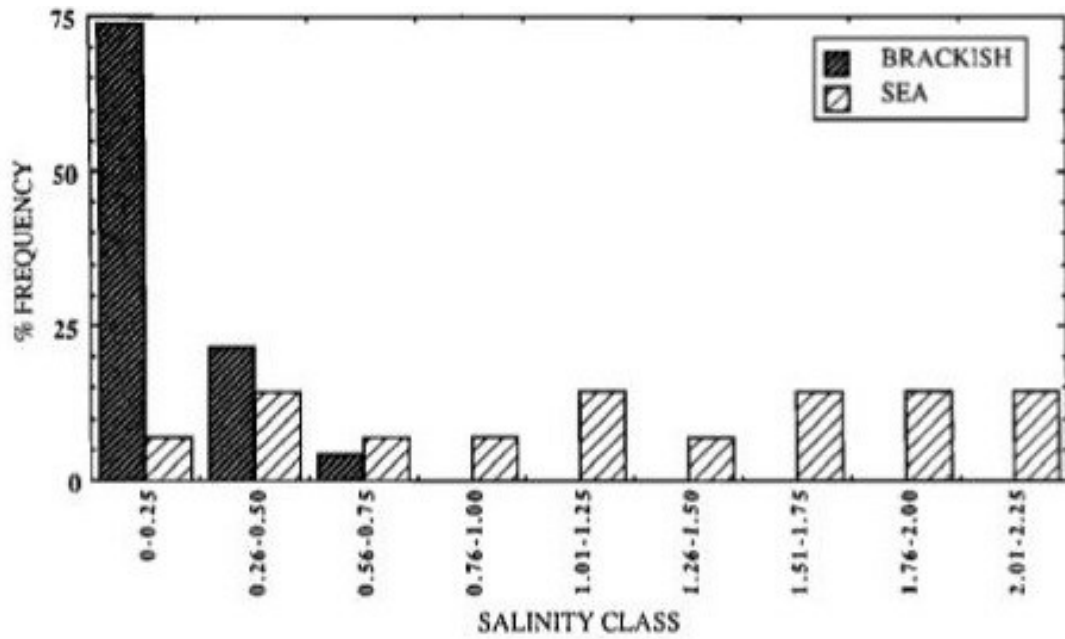


**Figure 5.2:** The frequency distribution of salinity values in brackish ice and sea ice extracted from the Ward Hunt Ice Shelf, showing that 75% of the brackish ice samples were found in the 0-0.25 psu category, while sea ice occupied all 9 classes, with only 5% in the 0-0.25 psu category. After Jeffries et al. (1989).

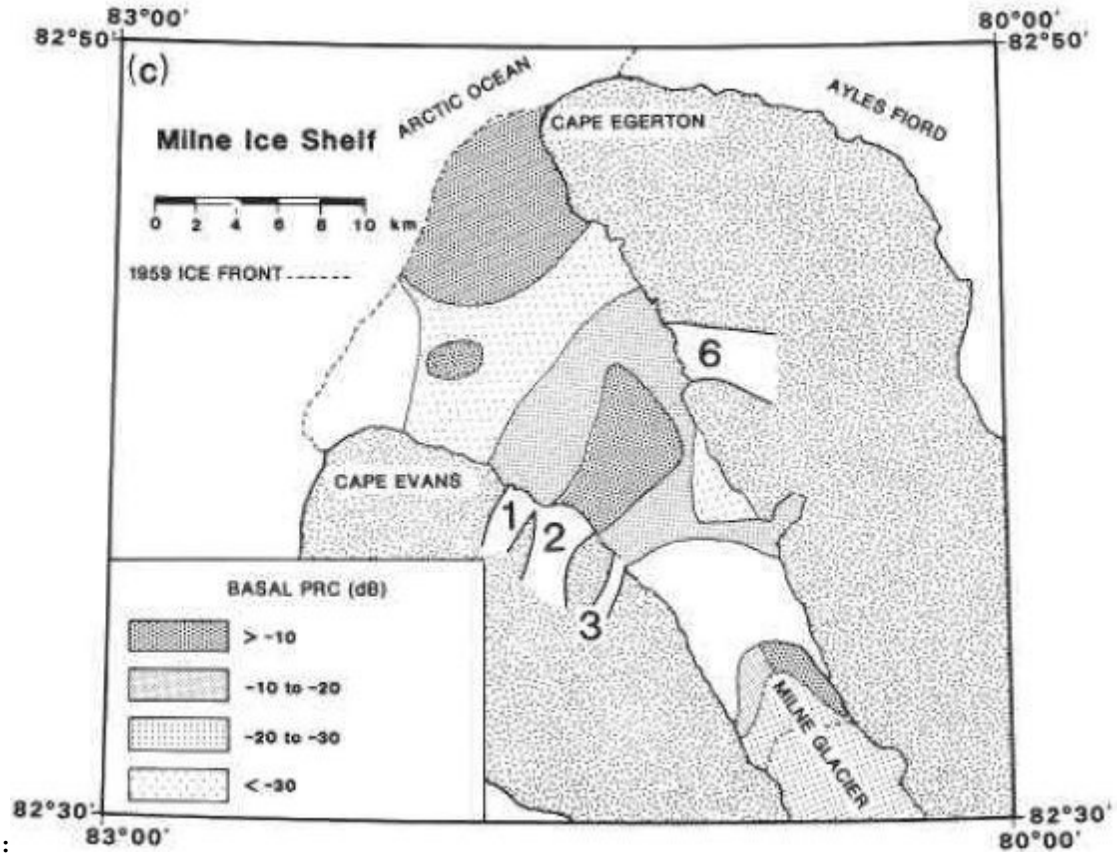


**Figure 5.3:** Basal power reflection coefficient (PRC) interpretation across the Milne Ice Shelf where regions less than -30 dB implies the possible presence of brackish ice. After Narod et al. (1988).



**Figure 5.4:** Ice surface showing the debris rich surface across the central Milne Ice Shelf from June, 2012 (Photo taken by helicopter courtesy of Andrew Hamilton).

## Chapter 6 Conclusions

This study provides new descriptions of three different ice types across two remaining ice shelves along the northern coast of Ellesmere Island. Both the geophysical characteristics and SAR backscatter of the meteoric ice (type A) were anticipated and similar to previous studies (Jeffries, 2002). The same can be said for the lake ice extracted from the Milne Fiord epishelf lake, with the exception of the SAR backscatter surrounding core site C2. Although the texture and salinity of C2 were consistent with freshwater lake ice, it fell well below the  $\sigma^{\circ}$  threshold for perennial freshwater ice (Veillette et al. 2008; White et al., in revision). The cause of this discrepancy is not well understood and should be investigated in future studies. Likewise, the use of SAR backscatter to identify type B ice was confounded by the difference between subtype Bm and Bp. In this case, the same backscatter values represented brackish basement ice and old sea ice basement ice, respectively. These findings illustrate that the interpretation and delineation of ice types in satellite SAR imagery solely based on SAR backscatter is at times ambiguous and that further field validation from ice cores and associated laboratory analyses is necessary. However, examining the cross-pol ratio may provide a way to distinguish iced firn from epishelf lake ice due to the larger variability within the epishelf lake ice signal.

Ice cores from the central section of the Milne Ice Shelf provided new evidence that the ice shelf is comprised of stratified layers of glacier and brackish ice, with brackish ice close to the surface. It is therefore possible that the observed ice texture and structure in this region represent both the original growth conditions and processes found at the base of the Milne Ice Shelf. This implies that the Milne Ice Shelf is a composite ice shelf,

composed of both marine and meteoric ice (Lemmen et al. 1988b). This contrasts with previous research which has categorised the Central Unit of the Milne Ice Shelf as glacier ice (Jeffries et al. 1985; Jeffries, 2002; Mueller et al., 2006; Mortimer et al., 2012). This could indicate that surface ablation over time has enabled stratified ice from the bottom of the shelf to rise to the surface, or that the glacial input to the Milne Ice Shelf was always restricted to localized glacier termini. The structure and texture of the Petersen Ice Shelf cores were consistent with layered sea and brackish ice, which suggests that the eastern portion of the Petersen Ice Shelf is not predominantly glacier fed.

More geophysical ice property data is still needed to provide a larger dataset of the different ice types that are found across the ice surface of the northern coast of Ellesmere Island. This will further address the objective of examining the relationship between the geophysics and backscatter to properly distinguish the ice using SAR satellite imagery. Nonetheless, this work was the first to elucidate quantitatively the influence of bubbles (presence, size and shape) on  $\sigma^{\circ}$  in multipolarized SAR imagery. Furthermore, several deeper ice cores across the ice surface are needed to properly assess the present state of the Milne Ice Shelf and to determine the extent of basement ice within the ice shelf. The present state of the Petersen Ice Shelf would render this task almost impossible due to its extensive recent break-up (White et al., 2015).

This research provides a step toward the improvement of our ability to assess inter-annual and long-term changes (past and future) of a variety of ice cover types. This will also

allow for improved understanding of the physical changes that are occurring across the ice cover along the northern coast of Ellesmere Island.

## Chapter 7 References

- Alley, R.B. (1988). Fabrics in polar ice sheets: development and prediction. *Science*, 240(4851), 493-495.
- Anisimov, O.A., Vaughan, D.G., Callaghan, T.V., Furgal, C., Marchant, H., Prowse, T.D., Vilhjálmsson, H., and Walsh, J.E. (2007). Polar Regions (Arctic and Antarctic). *Climate Change 2007: Impacts, Adaptation and Vulnerability. Contribution of Working Group II to the Fourth Assessment Report of the Intergovernmental Panel on Climate Change*, M.L. Parry, O.F. Canziani, J.P. Palutikof, P.J. van der Linden and C.E. Hanson, Eds., Cambridge University Press, Cambridge, 653-685.
- Azuma, N. and Higashi, A. (1985). Formation processes of ice fabric pattern in ice sheets. *Annals of Glaciology*, 6(130), 130-134.
- Barber, D.G., and LeDrew, E.F. (1991). SAR sea ice discrimination using texture statistics: a multivariate approach. *Photogrammetric Engineering and Remote Sensing*, Vol. 57, No. 4, pp. 385-395.
- Bakker, W.H., Grabmaier, K.A., Hunneman, G.C., Van Der Meer, F.D., Prakash, A., Tempfli, K., Gieske, A.S.M., Hecker, C.A., Janseen, L.L.F., Parodi, G.N., Reeves, C.V., Weir, M.J.C., Gorte, B.G.H., Horn, J.A., Kerle, N., Pohl, C., Van Ruitenbeek, F.J. and Woldai, T. (2004) *Principles of remote sensing, an introductory textbook*. The international institute for geo-informational science and earth observation (ITC), Enschede, the Netherlands.
- Berthier, E., Vadon, H., Baratoux, D., Arnaud, Y., Vincent, C., Feigl, K.L., Rémy, F., and Legrésy, B. (2005). Surface motion of mountain glaciers derived from satellite optical imagery. *Remote Sensing of Environment*, 95(1), 14-28.
- Braun, C., Hardy, D.R., Bradley, R.S., and Sahanatien, V. (2004). Surface mass balance of the Ward Hunt Ice Rise and Ward Hunt Ice Shelf, Ellesmere Island, Nunavut, Canada. *Journal of Geophysical Research-Atmospheres*, 109(D22), D22110.
- Budd, W.F. and Jacka, T.H. (1989). A review of ice rheology for ice sheet modeling. *Cold Regions Science and Technology*, 16(2), 107-144.
- Casey, J.A., and Kelly, R.E.J. (2010). Estimating the equilibrium line of Devon Ice Cap, Nunavut, from RADARSAT-1 ScanSAR wide imagery. *Canadian Journal of Remote Sensing*, 36(sup1), S41-S55.
- Challinor, L. (1973). *A dictionary of geology*. Cardiff. University of Wales Press.
- Clausi, D. (2001). Comparison and fusion of co-occurrence, Gabor and MRF texture features for classification of SAR sea-ice imagery. *Atmosphere-Ocean*, 39(3), 183-194.

- Cole, D.M. (2001). The microstructure of ice and its influence on mechanical properties. *Engineering Fracture Mechanics*, 68(17), 1797-1822.
- Comiso, J.C., Parkinson, C.L., Gertsen, R., and Stok, L. (2008). Accelerated decline in the Arctic sea ice cover. *Geophysical Research Letters*, 35(1), L01703.
- Connor, L.N., Laxon, S.W., Ridout, A.L., Krabill, W.B., and McAdoo, D.C. (2009). Comparison of Envisat radar and airborne laser altimeter measurements over Arctic sea ice. *Remote Sensing of Environment*, 113(3), 563-570.
- Copland, L., Mueller, D.R., and Weir, L. (200). Rapid loss of the Ayles Ice Shelf Ellesmere Island, Canada. *Geophysical Research Letters*, 34(21), L21501
- Copland, L., and Mueller, D. (eds). (In press). *Arctic Ice Shelves and Ice Islands*. Springer-Verlag.
- Crary, A.P. (1958). Arctic Ice Islands and Ice Shelf studies, Part I, *Arctic*, 11(1), 3-42.
- Curlander, J.C., and McDonough, R.N. (1991). *Synthetic aperture radar: Systems and signal processing*. New York. Wiley, xvii-647.
- Deng, H., and Clausi, D.A. (2005). Unsupervised segmentation of synthetic aperture radar sea ice imagery using a novel Markov random field model. *IEEE Transactions on Geoscience and Remote Sensing*, 43(3), 528-538.
- Derksen, C., Smith, S.L., Sharp, M., Brown, L., Howell, S., Copland, L., Mueller, D.R., Fletcher, C.G., Tivy, A., Bernier, M., Bourgeois, J., Brown, R., Burn, C.R., Duguay, C., Kushner, P., Langlois, A., Lewkowicz, A.G., Royer, A., and Walker, A. (2012). Variability and change in the Canadian cryosphere. *Climate Change*, 115(1), 59-88.
- Dierking, W., Garrity, C., and Ramseier, R.O. (1994). Interpretation of radar signatures observed in SAR images of ice island T-3 by means of backscatter modelling. *EARLSEL Advances in Remote Sensing* 3(2), 31-43
- Durand, G., Gagliardini, O., Thorsteinsson, T., Svensson, A., Kipfstuhl, S., Dahl-Jensen, D., (2006). Ice microstructure and fabric: an up-to-date approach for measuring texture. *Journal of Glaciology* 52(19), 619-630
- Dowdeswell, J.A., Gorman, M.R., Glazovsky, A. F., and Macheret, Y.Y. (1994). Evidence for floating ice shelves in Franz Josef Land, Russian High Arctic. *Arctic and Alpine Research*, 26(1), 86-92.
- Eicken, H., and Lange, M.A. (1989). Sea ice thickness data: The many vs. the few. *Geophysical Research Letters*, 16(6), 495-498.

England, J.H., Lakeman, T.R., Lemmen, D.S., Bednarski, J.M., Stewart, T.G. and Evans, D.J.A. (2008) A millennial-scale record of Arctic Ocean sea ice variability and the demise of the Ellesmere Island ice shelves. *Geophysical Research Letters*, 35(19), L19502

Faria, S.H., Weikusat, I., Azuma, N., (2014)a. The microstructure of polar ice. Part I: Highlight from ice core research. *Journal Structural Geology*, 61, 2-20

Faria, S.H., Weikusat, I., Azuma, N., (2014)b. The microstructure of polar ice. Part II: State of the art. *Journal Structural Geology*, 61, 21-49.

Fung, A.K., and Eom, H.J. (1982). Application of a combined rough surface and volume scattering theory to sea ice and snow backscatter. *IEEE Transactions on Geoscience and Remote Sensing*, GE-20(4), 528-536.

Gardner, A.S., Moholdt, G., Wouter, B., Wolken, G.J., Burgess, D.O., Sharp, M.J., Cogley, J.G., Braun, C., and Labine, C. (2011). Sharply increased mass loss from glaciers and ice caps in the Canadian Arctic Archipelago. *Nature*, 473(7347), 357-261.

Gibson, J.A.E., and Andersen, D.T. (2002). Physical structure of epishelf lakes of the southern bunger hills, East Antarctica. *Antarctic Science*, 14(3), 253-261.

Gow, A. J. (1986). Orientation textures in ice sheets of quietly frozen lakes. *Journal of Crystal Growth*, 74(2), 247-258.

Grenfell, T.C., Barber, D.G., Fung, A.K., Gow, A.J., Jezek, K.C., Knapp, E.J., Nghiem, S.V., Onstott, R.G., Perovich, D.K., Roesler, C.S., Swift, C.S., and Tanis, F. (1998). Evolution of electromagnetic signatures of sea ice from initial formation to the establishment of thick first-year ice. *IEEE Transactions on Geoscience and Remote Sensing*, 36(5), 1642-1654.

Hanna, E., Huybrechts, P., Steffen, K., Cappelen, J., Huff, R., Shuman, C., Irvine-Fynn, T., Wise, S., and Griffiths, M. (2008). Increased runoff from melt from the Greenland Ice Sheet: A response to global warming. *Journal of Climate*, 21(2), 331-341.

Hattersley-Smith, G., Serson, H., Keys, J.E., and Mielke, J.E. (1970). Density stratified lakes in northern Ellesmere Island. *Nature*, 225(5227), 55-56.

Haverkamp, D., Soh, L.K., and Tsatsoulis, C. (1993). A dynamic local thresholding technique for sea ice classification. In the 1993 IEEE International Geoscience and Remote Sensing Symposium (IGARRS'93), August 18-21, Tokyo, Japan, 638-640.

IPCC, 2013. Climate Change 2013: The Physical Science Basis. Contribution of Working Group I to the Fifth Assessment Report of the Intergovernmental Panel on Climate Change [Stocker, T.F., Qin, G.-K., Plattner, M., Tignor, S.K., Allen, J., Boschung, A., Nauels, Y., Xia, V., Bez, and P.M. Midgley (eds.)]. Cambridge University Press, Cambridge, United Kingdom and New York, NY, USA, 1533.

Jeffries, M.O. (1985a). Physical, chemical and isotopic investigations of Ward Hunt Ice Shelf and Milne Ice Shelf, Ellesmere Island, Northwest Territories. PhD thesis Department of Geography, University of Calgary.

Jeffries, M.O. (1985b). Ice shelf studies off Northern Ellesmere Island, spring 1983. *Arctic*, 38(3): 174-177.

Jeffries, M.O. (1986a). Ice Island calvings and ice shelf changes, Milne Ice Shelf and Ayles Ice Shelf, Ellesmere Island, NWT. *Arctic*, 39(1), 15-19.

Jeffries, M. O. (1986b). Glaciers and the morphology and structure of Milne Ice Shelf, Ellesmere Island, N.W.T., Canada. *Arctic and Alpine Research*, 18(4), 397-405.

Jeffries, M.O., Sackinger, W.M., Krouse, H.R. and Serson, H.V. (1988) Water circulation and ice accretion beneath Ward Hunt Ice Shelf (Northern Ellesmere Island, Canada) deduced from salinity and isotope analysis of ice cores. *Annals of Glaciology*, 10, 68-72.

Jeffries, M.O. and Sackinger, W.M. (1989) Some measurements and observations of very old sea ice and brackish ice, Ward Hunt Ice Shelf, N.W.T., *Atmosphere-Ocean*, 27(3), 553-564.

Jeffries, M.O., Serson, H.V., Krouse, H.R., and Sackinger, W.M. (1991). Ice physical properties, structural characteristics and stratigraphy in Hobson's Choice Ice Island and implications for the growth history of east Ward Hunt Ice Shelf, Canadian High Arctic. *Journal of Glaciology*, 37(126), 247-260.

Jeffries, M.O. (1992). Arctic Ice Shelves And Ice Islands: Origin, growth and disintegration, physical characteristics, structural-stratigraphic variability, and dynamics. *Reviews of Geophysics*, 30(3), 245.

Jeffries, M.O., Morris, K., Weeks, W.F., and Wakabayashi, H. (1994). Structural and stratigraphic features and ERS-1 synthetic aperture radar backscatter characteristics of ice growing on shallow lakes in NW Alaska, winter 1991-1992. *Journal of Geophysical Research*, 99(C11), 22.459-22.471.

- Jeffries, M.O. (2002). Ellesmere Island ice shelves and ice islands. In: Williams, R.S., and Ferrigno, J.G. (eds.), *Satellite Image Atlas of Glaciers of the World: North America*. Washington: United States Geological Survey, J147-J164.
- Johnston, M.E., and Timco, G.W. (2008). *Understanding and identifying old ice in summer*. Ottawa: Canadian Hydraulics Centre, National Research Council.
- Jouzel, J., Lorius, C, Petit, J.R., Barkov, N.I., Kotlyakov Petrov, V.M., and Genthon, C. (1987). Vostok ice core: A continuous isotope temperature record over the last climatic cycle (160,000 years). *Nature*, 329(6138), 403-408.
- Jungblut, A.D., Mueller, D.R. and Vincent, W.F. (In press) *Arctic Ice Shelf Ecosystems*. In L. Copland and D.R. Mueller (Eds.), *Arctic Ice Shelves and Ice Islands*. Dordrecht: Springer SBM.
- Kealey, C., Mueller, D. and Copland, L. (2011). *Canadian Ice Shelves Breaking up at High Speed*. [press release], September 27, 2011.
- Khan, S.A., Kjær, K.H., Bevis, M., Bamber, J.L., Wahr, J., Kjeldsen, K.K., Korsgaard, N.J., Stearns, L.A., Van den Broke, M.R., Liu, L., Larsen, N.K., and Muresan, I.S. (2014). Sustained mass loss of the Northeast Greenland Ice Sheet triggered by regional warming. *Nature Climate Change*, 4(4), 292-299.
- Koenig, L.S., Greenaway, K.R., Dunbar, M. and Hattersley-Smith, G. (1952) *Arctic Ice Islands*. *Arctic*, 5(2), 66-103.
- Koerner, R.M. (1968). Fabric analysis of a core from the Meighen Ice Cap, Northwest Territories, Canada. *Journal of Glaciology*, 7(51), 421-430.
- Koerner, R.M. (1970). Some observations on superimposition of ice on the Devon Island Ice Cap, N.W.T. Canada. *Geographical Analysis*, 52A(I), 57-67.
- Langway, C.C., Jr. (1958). *Ice fabrics and the universal stage*. SIPRE Tech. Rep. 62.
- Lemmen, D.S., Evans, D.J.A., and England, J. (1988)a. Discussion of "Glaciers and the morphology and structure of the Milne Ice Shelf, Ellesmere Island, N.W.T., Canada" by Martin O. Jeffries. *Arctic Alpine Research*, 20(3), 366-368.
- Lemmen, D. S., Evans, D.J.A., and England, J. (1988)b. Ice shelves of northern Ellesmere Island, NWT. *Canadian Geographic*, 32(4), 363-367.
- Lüthi, D., Floch, M.L., and Bereiter, B. (2008). High-resolution carbon dioxide concentration record 650,000-800,000 years before present. *Nature* , 453, 379.

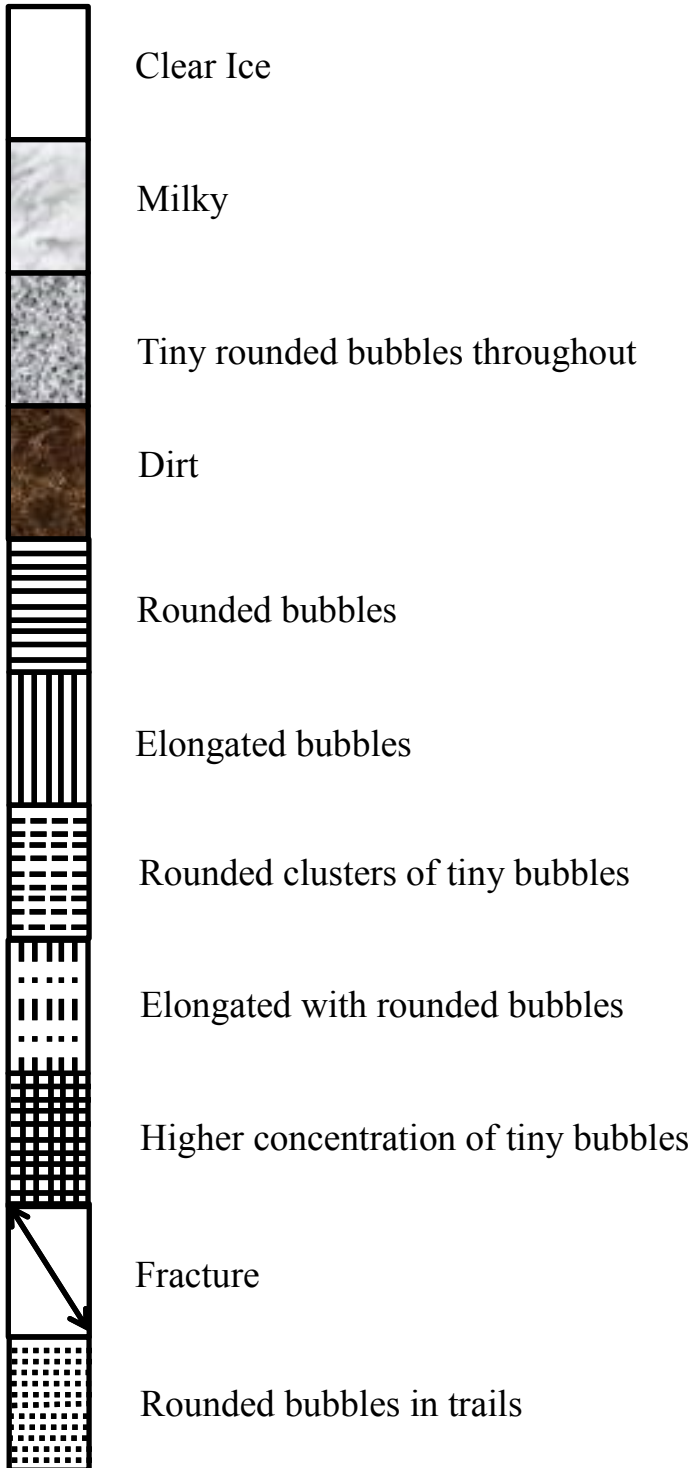
- Lyons, J.B., R.H. Ragle, and A.J. Tamburi (1972), Growth and grounding of the Ellesmere Island ice rises, *Journal of Glaciology*, 11(61), 43-52.
- Lyons, J.B., Savin, S.M., Tamburi, A.J. (1971). Basement ice, Ward Hunt Ice Shelf, Ellesmere Island, Canada. *Journal of Glaciology*, 10(38) 93-100.
- Marshall, E.W. (1955). Structural and stratigraphic studies of the northern Ellesmere Ice Shelf. *Arctic*, 8, 109-114.
- Marshall, E.W. (1960). Structure and stratigraphy of T-3 and the Ellesmere Ice Shelf, in *Scientific Studies of Fletcher's Ice Island, T-3, 1952 - 1955*, Res. Pap. 63, pp. 47 -57, U.S. Air Force, Cambridge Research Center, Bedford, Mass.
- McCandless, S.W. (1989). SAR in space - The theory, design, engineering and application of a space-based SAR system. *Space Based Radar Handbook*, L Cantafio, Ed. Artech House, 121-166
- McCandless, S.W., and Jackson, C.R. (2004). Principles of Synthetic Aperture Radar, S. W. McCandless and C. R. Jackson, Chapter 1 of *SAR Marine User's Manual*, NOAA, 1-23.
- Mortimer, C. (2010) Quantification of changes for the Milne Ice Shelf, Nunavut, Canada, 1950-2009. M.Sc. thesis, Department of Geography, University of Ottawa.
- Mortimer, C.A., Copland, L., and Mueller, D.R. (2012). Volume and area changes of the Milne ice shelf, Ellesmere Island, Nunavut, Canada, since 1950. *Journal of Geophysical Research*, 117, F04011.
- Mueller, D.R., Vincent, W.F. and Jeffries, M.O. (2003). Break-up of the largest Arctic Ice Shelf and associated loss of an epishelf lake. *Geophysical Research Letters*, 30(20), 2031.
- Mueller, D.R., Vincent, W.F. and Jeffries, M.O. (2006) Environmental gradients, fragmented habitats, and microbiota of a northern ice shelf cryoecosystem, Ellesmere Island, Canada. *Arctic, Antarctic, and Alpine Research*, 38(4), 593-607.
- Mueller, D.R., Copland, L., Hamilton, A., and Stern, D. (2008). Examining Arctic ice shelves prior to the 2008 breakup. *EOS, Transactions of the American Geophysical Union*, 89(49), 502-503.
- Narod, B.B., Clarke, G.K.C., and Prager, B.T. (1988). Airborne UHF radar sounding of glaciers and ice shelves, northern Ellesmere Island, arctic Canada. 25(1), 95-105.

- Obbard, R.W. (2006). Microstructural determinants in glacial ice. PhD Thesis, Department Engineering, Dartmouth College, New Hampshire.
- Onstott, R.G., Shuchman, R.A. (1992). SAR and scatterometer signatures of sea ice. American Geophysical Union, Washington D.C., 68, 2-4.
- Onstott, R.G., and Shuchman, R.A. (2004). SAR measurements of sea ice, S. W. McCandless and C. R. Jackson, Chapter 1 of SAR Marine User's Manual, NOAA, 81-115.
- Parker, W.V., 2012. Discover the benefits of radar imaging. Earthwide Communications LLC, [www.eijournal.com](http://www.eijournal.com).
- Parkinson, L. (2014). Global sea ice coverage from satellite data: Annual cycle and 35 yr. trends. *Journal of Climate*, 27(24), 9377-9382.
- Peary, R. E. (1907). *Nearest the Pole: A Narrative of the Polar Expedition of the Peary Arctic Club in the S.S. Roosevelt, 1906-1906*, 1st ed., 410 pp., Hutchinson, London.
- Petit, J.R., Lipenkov, V.Y., Kotlyakov, V.M., Barkov, N.I., Bender, M., Davis, M., Delaygue, G., Barnola, J.M., Stievenard, M., Lorius, C., Delmotte, M., Pépin, L., Chappellaz, J., Saltzman, E., Legrand, M., Basile, I., Jouzel, J., Raynaud, D., and Ritz, C. (1999). Climate and atmospheric history of the past 420,000 years from the Vostok ice core, Antarctica. *Nature*, 399(6735), 429-436.
- Polyak, L., Alley, R.B., Andrews, J.T., Brigham-Grette, J., Cronin, T.M., Darby, D.A., Dyke, A.S., Fitzpatrick, J.J., Funder, S., Holland, M., Jennings, A.E., Miller, G.H., O'Regan, M., Savelle, J., Serreze, M., St. John, K., White, J.W.C., and Wolff, E. (2010). History of sea ice in the arctic. *Quaternary Science Reviews*, 29(15), 1757-1778.
- Pope, S., Copland, L., and Mueller, D. (2012). Loss of multiyear landfast sea ice from Yelverton Bay, Ellesmere Island, Nunavut, Canada. *Arctic, Antarctic, and Alpine Research*, 44(2), 210-221.
- Ragle, R.H., Blair, R.G., and Persson, L.E.. (1964). Ice core studies of Ward Hunt Ice Shelf. *Journal of Glaciology*, 5(37), 39-59.
- Raney, R.K. (1998). Radar Fundamentals: Technical perspective. Principles and Applications of Imaging Radar. Manual of Remote Sensing, F.M. Henderson and A.J. Lewis, Eds., third ed., Vol. 2, John Wiley and Sons, 9-130.
- Schulson, E.M. (1999). The structure and mechanical behavior of ice. *The Journal of the Minerals, Metals, & Materials Society*, 51(2), 21-27.

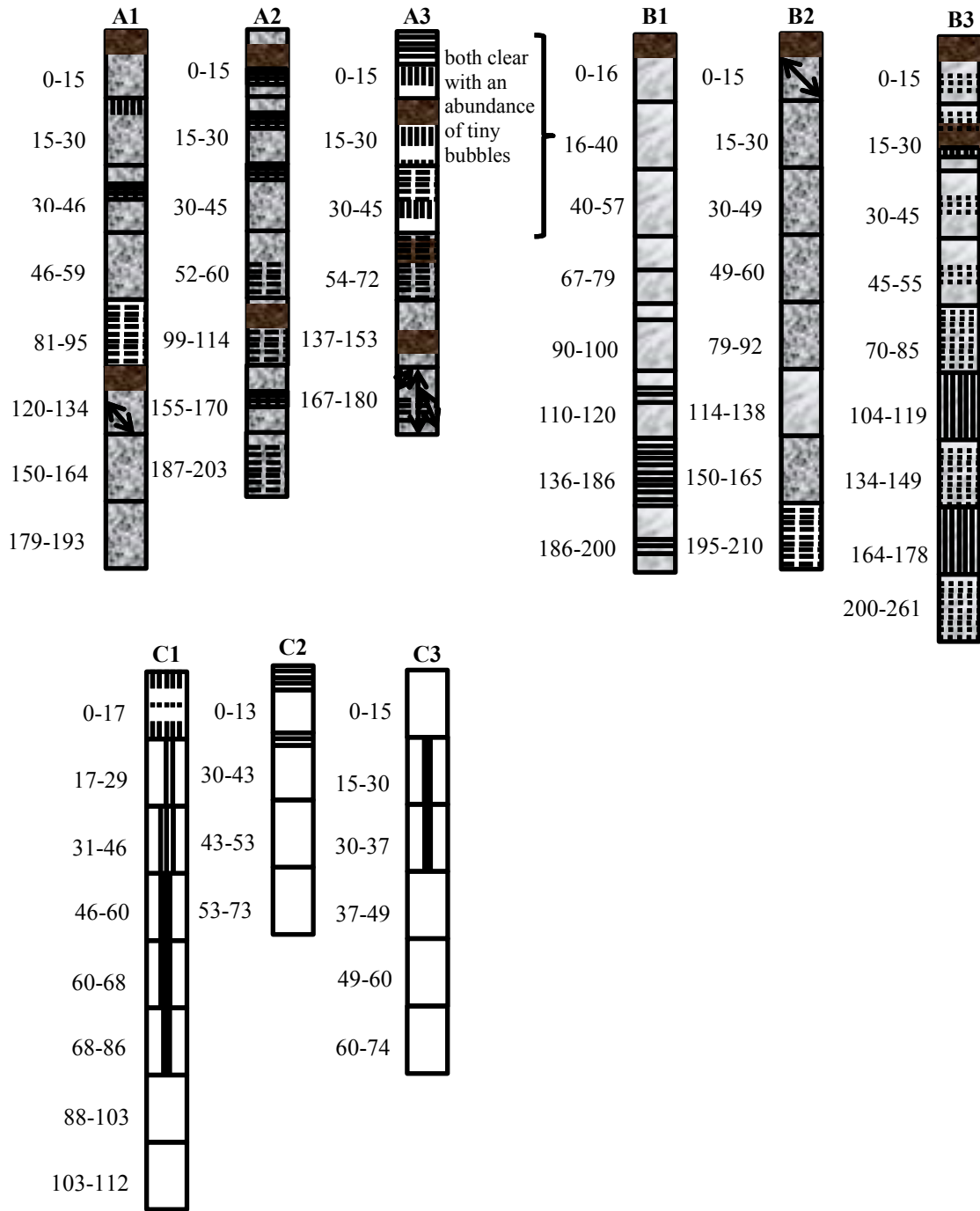
- Rignot, E., Echelmeyer, K., and Krabill, W. (2001). Penetration depth of interferometric synthetic-aperture radar signals in snow and ice. *Geophysical Research Letters*, 28(18), 3501.
- Scheuchl, B., Cumming, I.G., and Hajnsek, I. (2005). Classification of fully polarimetric single- and dual-frequency SAR data of sea ice using the Wishart statistics. *Canadian Journal of Remote Sensing*, 31(1), 61-72.
- Serreze, M.C., and Barry, R.G. (2011). Processes and impacts of arctic amplification: A research synthesis. *Global and Planetary Change*, 77(1), 85-96.
- Sinha, N.K. (1986). Young Arctic frazil sea ice: Field and laboratory strength tests. *Journal of Materials Science*, 21(5), 1533-1546.
- Shokr, M.E., and Sinha, N.K. (1994). Arctic sea ice microstructure observations relevant to microwave scattering. *Arctic*, 47(3), 265-279.
- Shokr, M.E. (2009). Compilation of radar backscatter database of sea ice types and open water using operational analysis of heterogeneous ice regimes. *Canadian Journal of Remote Sensing*, 35(4), 369-384.
- Smith, J.A., Hodgson, D.A., Bentley, M.J., Verleyen, E., Leng, M.J., and Roberts, S.J. (2006). Limnology of two Antarctic epishelf lakes and their potential to record periods of ice shelf loss. *Journal of Paleolimnology*, 35(2), 373-394.
- Steffen, K., Nghiem, S.V., Huff, R., and Neumann, G. (2004). The melt anomaly of 2002 on the Greenland Ice Sheet from active and passive microwave satellite observations. *Geophysical Research Letters*, 31(20), L20402
- Stroeve, J.C., Serreze, M.C., Holland, M.M., Kay, J.E., Maslanik, J., and Barrett, A.P. (2012). The Arctic's rapidly shrinking sea ice cover: A research synthesis, *Climate Change*, 110, 1005-1027.
- Sullivan, R.J. (2000). *Microwave radar: Imaging and advanced concepts*. Boston, MA: Artech House.
- Thomsen, B.B., Nghiem, S.V., and Kwok, R. (1998). Polarimetric C-band SAR observations of sea ice in the Greenland Sea. Paper presented at the International Geoscience and Remote Sensing Symposium (IGARSS), 5, 2502-2504.
- Thorsteinsson, T., Kipfstuhl, J., and Miller, H. (1997). Textures and fabrics in the GRIP ice core. *Journal of Geophysical Research*, 102(C12), 26583-26599.

- Tomiyasu, K. (1978). Tutorial review of synthetic-aperture radar (SAR) with applications to imaging of the ocean surface. *Proceedings of the IEEE*, 66(5), 563-583.
- Tucker, W.B., Gow, A.J., and Richter, J.A. (1984). On small-scale horizontal variations of salinity in first-year sea ice. *Journal of Geophysical Research*, 89(C4), 6505-6514.
- Velicogna, I. (2009). Increasing rates of ice mass loss from the Greenland and Antarctic Ice Sheets revealed by GRACE. *Geophysical Research Letters*, 36(19), L19503.
- van der Sander, J.J., and Drouin, H. (2011). Satellite SAR observation of river ice: A RADARSAT-2 (C-band) and ALOS PALSAR (L-band) comparison. CGU HS Committee on River Ice Processes and the Environment 16th Workshop on River Ice Winnipeg, Manitoba, September 18 - 22, 2011.
- Van Wijngaarden, W.A. (2014). Temperature trends in the Canadian Arctic during 1895-2014. *Theoretical and Applied Climatology*
- Veillette, J., Mueller, D.R., Antoniades, D., and Vincent, W.F. (2008). Arctic epishelf lakes as sentinel ecosystems: Past, present and future. *Journal of Geophysical Research - Biogeosciences*, 113(G4), G04014.
- Vincent, W.F., Gibson, J.A.E., and Jeffries, M.O. (2001). Ice shelf collapse, climate change, and habitat loss in the Canadian High Arctic. *Polar Record*, 37, 133-142.
- Wadhams, P. (2000) *Ice in the Ocean*. Gordon and Breach Science Publishers, Amsterdam, 351.
- Wand, U., Hermichen, W.D., Bruggemann, E., Zierath, R. and Klokov, V.D. (1988). Stable isotope and hydrogeochemical studies of Beaver Lake and Radok Lake, MacRobertson Land, East Antarctica. *ZFI Mitteilungen*, 143, 99-111.
- Weeks, W.F., and Gow, A.J. (1978). Preferred crystal orientations in the fast ice along the margins of the Arctic Ocean. *Journal of Geophysical Research*, 83.
- Weeks, W.F., and Hibler, W.D.,III. (2010). *On sea ice*. Fairbanks: University of Alaska Press.
- Wilen, L.A., Diprinzio, C.L., Alley, R.B., and Azuma, N. (2003). Development, principles, and applications of automated ice fabric analyzers. *Microscopy Research and Technique*, 62(1), 2-18
- Williamson, S., Sharp, M., Dowdeswell, J., Benham, T. (2008). Iceberg calving rates from northern Ellesmere Island Ice Caps, Canadian Arctic, 1999-2003. *Journal of Glaciology*, 54(186): 391-400.

## Appendix A



Appendix A1: Ice structure legend for Figure A2



**Appendix A2:** Visual structure of each ice core extracted from each ice type. See Figure A1 for legend.

## Appendix B

**Table B1:** Results for the surface analysis (NA meaning no data available).

Core Name	Area	$\sigma^{\circ}_{HH}$ (dB)	$\sigma^{\circ}_{HV}$ (dB)	$\sigma^{\circ}_{VV}$ (dB)	Rayleigh	Snow Depth (cm)	Snow Density (g/cm <sup>3</sup> )	Snow Temperature (°C)
<b>A1</b>	ridge	-9	-17	-9	rough	30	0.26	-15
<b>A2</b>	ridge	-6	-12	-4	rough	35	0.36	-19
<b>A3</b>	middle ridge	-6	-10	-7	rough	50	0.26	-19
<b>B1</b>	ridge	-12	-22	-13	rough	27.5	0.21	-16
<b>B2</b>	ridge	-14	-20	-14	rough	35	0.35	-18
<b>B3</b>	flat	-13	-24	-14	rough	46	0.47	-13
<b>B4</b>	ridge	-19	-20	-28	rough	NA	NA	NA
<b>C1</b>	flat	-4	-12	-6	rough	60	0.5	-6
<b>C2</b>	flat	-14	-22	-16	smooth	58	NA	-7
<b>C3</b>	flat	-3	-16	-4	smooth	63	0.53	-7

**Table B2:** Ice structure, temperature and bulk salinity data. For the fracture and dirt variables 0=no presence, 1=presence, and the bubble concentration are rated 1-4 (1=low, 4=very high) (NA meaning no data available).

Core Name	Segment	Segment Start (cm)	Segment End (cm)	Salinity (psu)	Temperature (°C)	Bubble Concentration	Fracture	Dirt
A1	A1-1	0	15	0.01	-19	4	0	1
A1	A1-2	15	30	NA	-19	4	0	0
A1	A1-3	30	46	0.02	-19	3	0	0
A1	A1-4	46	59	0.01	NA	4	0	0
A1	A1-5	66	81.5	0.01	-19	NA	0	0
A1	A1-6	81	95	0.01	-19	4	0	0
A1	A1-7	95	111	0.01	NA	NA	0	0
A1	A1-8	120	134	0.01	-18	4	1	1
A1	A1-9	134	150	0.01	-19	NA	0	0
A1	A1-10	150	164	0.01	-19	4	0	0
A1	A1-11	164	179	0.02	-19	NA	0	0
A1	A1-12	179	193	0.01	-18	4	0	0
A2	A2-1	0	15	0.01	-20	3	0	1
A2	A2-2	15	30	0.01	-20	4	0	0
A2	A2-3	30	45	0.01	-21	4	0	0
A2	A2-4	52	69	0.01	-19	4	0	0
A2	A2-5	73	88	0.02	NA	NA	0	0
A2	A2-6	99	114	0.01	-20	4	0	1
A2	A2-7	120	135	0.02	-21	NA	0	0
A2	A2-8	155	170	0.01	NA	4	0	0
A2	A2-9	170	184	0.01	-19	NA	0	0
A2	A2-10	187	203	0.01	-21	3	0	0
A3	A3-1	0	15	0.02	-20	4	0	0
A3	A3-2	15	30	0.02	-21	4	0	1
A3	A3-3	30	45	0.01	-21	3	0	0
A3	A3-4	54	72	0.01	-20	3	0	1
A3	A3-5	76	90	0.02	NA	4	0	0
A3	A3-6	90	105	0.01	-20	NA	0	0
A3	A3-7	105	121	0.01	-19	NA	0	0
A3	A3-8	137	153	0.01	-20	4	0	1
A3	A3-9	153	168	0.01	-20	NA	0	0
A3	A3-10	167	180	0.01	-20	3	1	0
B1	B1-1	0	2.5	NA	NA	1	0	1

<b>B1</b>	B1-2	2.5	16	NA	-16	1	0	1
<b>B1</b>	B1-3	16	40	NA	-16	1	0	0
<b>B1</b>	B1-4	40	57.5	NA	-16	1	0	0
<b>B1</b>	B1-5	57	67	0.05	-15	1	0	0
<b>B1</b>	B1-6	67.5	79	NA	-16	NA	0	0
<b>B1</b>	B1-7	79	90	0.05	-16	NA	0	0
<b>B1</b>	B1-8	90	100	NA	-16	1	0	0
<b>B1</b>	B1-9	100	110	0.08	-16	NA	0	0
<b>B1</b>	B1-10	110	120	NA	-15	1	0	0
<b>B1</b>	B1-11	120	136	0.11	-15	NA	0	0
<b>B1</b>	B1-12	136	146	NA	-16	1	0	0
<b>B1</b>	B1-13	146	156	0.17	-15	NA	0	0
<b>B1</b>	B1-14	156	166	NA	-15	1	0	0
<b>B1</b>	B1-15	166	176	0.12	-15	NA	0	0
<b>B1</b>	B1-16	176	186	NA	-15	1	0	0
<b>B1</b>	B1-17	186	200	NA	-15	1	0	0
<b>B1</b>	B1-18	681	696	NA	NA	1	0	0
<b>B2</b>	B2-1	0	15	0.01	-19	3	1	1
<b>B2</b>	B2-2	15	30	NA	-19	3	0	0
<b>B2</b>	B2-3	34	49	0.01	-19	3	0	0
<b>B2</b>	B2-4	46	60	0.01	-19	3	0	0
<b>B2</b>	B2-5	64	79	0.01	-19	NA	0	0
<b>B2</b>	B2-6	79	92	0.01	-19	3	0	0
<b>B2</b>	B2-7	96	111	0.02	-19	NA	0	0
<b>B2</b>	B2-8	114	130	0.01	-18	3	0	0
<b>B2</b>	B2-9	137	150	0.01	-19	NA	0	0
<b>B2</b>	B2-10	150	165	0.01	-19	3	0	0
<b>B2</b>	B2-11	180	195	0.02	-19	NA	0	0
<b>B2</b>	B2-12	195	210	0.01	-19	3	0	0
<b>B3</b>	B3-1	0	15	0.56	-15	1	0	1
<b>B3</b>	B3-2	15	30	1.11	-16	2	0	1
<b>B3</b>	B3-3	30	45	0.76	-16	1	0	0
<b>B3</b>	B3-4	45	55	NA	-15	1	0	0
<b>B3</b>	B3-5	55	70	1.09	-15	NA	0	0
<b>B3</b>	B3-6	70	85	0.94	-15	2	0	0
<b>B3</b>	B3-7	85	100	0.60	-15	NA	0	0
<b>B3</b>	B3-8	104	119	1.01	-15	2	0	0
<b>B3</b>	B3-9	119	134	1.20	-15	NA	0	0
<b>B3</b>	B3-10	134	149	0.94	-15	2	0	0
<b>B3</b>	B3-11	149	164	1.54	-15	NA	0	0

<b>B3</b>	B3-12	164	178	1.36	-14	2	0	0
<b>B3</b>	B3-13	184	199	0.59	-14	NA	0	0
<b>B3</b>	B3-14	200	215	0.40	-14	1	0	0
<b>B3</b>	B3-15	215	230	0.72	-14	NA	0	0
<b>B3</b>	B3-16	246	261	1.16	-14	1	0	0
<b>B4</b>	B4-1	0	7	0.04	-4	2	0	1
<b>B4</b>	B4-2	7	16	0.05	-3	2	0	0
<b>B4</b>	B4-3	17	29	0.02	-3	2	0	1
<b>B4</b>	B4-4	30	40	NA	-3	NA	0	0
<b>B4</b>	B4-5	41	50	0.01	-3	1	0	0
<b>B4</b>	B4-6	50	64	NA	-2	NA	0	0
<b>B4</b>	B4-7	64	76	0.01	-2	2	0	0
<b>B4</b>	B4-8	76	90	NA	-2	NA	0	0
<b>B4</b>	B4-9	90	99	0.01	-1	1	0	1
<b>B4</b>	B4-10	100	108	NA	-1	NA	0	0
<b>B4</b>	B4-11	108	117	0.02	NA	1	0	0
<b>B4</b>	B4-12	117	125	NA	NA	NA	0	0
<b>B4</b>	B4-13	126	134	0.02	NA	1	0	0
<b>B4</b>	B4-14	134	143	NA	NA	NA	0	0
<b>B4</b>	B4-15	143	158	0.01	NA	2	0	0
<b>B4</b>	B4-16	158	168	NA	NA	NA	0	0
<b>B4</b>	B4-17	168	179	0.02	NA	2	0	0
<b>B4</b>	B4-18	179	190	NA	NA	NA	0	0
<b>B4</b>	B4-19	190	205	0.01	NA	2	0	0
<b>B4</b>	B4-20	205	214	NA	NA	NA	0	0
<b>B4</b>	B4-21	214	224	0.01	NA	2	0	0
<b>B4</b>	B4-22	224	234	NA	NA	NA	0	0
<b>B4</b>	B4-23	234	244	0.02	NA	1	0	0
<b>C1</b>	C1-1	0	17	NA	-2	3	0	0
<b>C1</b>	C1-2	17	29	0.02	NA	1	0	0
<b>C1</b>	C1-3	31	46	NA	-2	1	0	0
<b>C1</b>	C1-4	46	60	NA	NA	1	0	0
<b>C1</b>	C1-5	60	68	NA	NA	1	0	0
<b>C1</b>	C1-6	68	86	NA	-1	1	0	0
<b>C1</b>	C1-7	88	103	NA	0	1	0	0
<b>C1</b>	C1-8	103	112	0.01	NA	1	0	0
<b>C2</b>	C2-1	0	13	0.01	NA	1	0	0
<b>C2</b>	C2-2	20	30	0.01	-2	1	0	0
<b>C2</b>	C2-3	30	43	0.01	NA	1	0	0
<b>C2</b>	C2-4	43	53	NA	NA	1	0	0

<b>C2</b>	C2-5	53	73	NA	0	1	0	0
<b>C3</b>	C3-1	0	15	0.01	-1	1	0	0
<b>C3</b>	C3-2	15	30	NA	NA	1	0	0
<b>C3</b>	C3-3	30	37	NA	NA	1	0	0
<b>C3</b>	C3-4	37	49	NA	-1	1	0	0
<b>C3</b>	C3-5	49	60	NA	NA	1	0	0
<b>C3</b>	C3-6	60	74	0.02	0	1	0	0

**Table B3:** Measurements of individual bubbles from the structural analysis (NA meaning no data available).

<b>Core Name</b>	<b>Bubble Size Horizontal (cm)</b>	<b>Bubble Size Vertical (cm)</b>	<b>Bubble Aspect</b>	<b>Bubble Size (cm)</b>
<b>A1-1</b>	0.1	0.1	1.0	0.1
<b>A1-1</b>	0.5	0.5	1.0	0.5
<b>A1-1</b>	0.5	1.5	0.3	1.0
<b>A1-2</b>	0.3	2.0	0.2	1.2
<b>A1-2</b>	0.1	0.1	1.0	0.1
<b>A1-2</b>	0.2	0.2	1.0	0.2
<b>A1-3</b>	0.2	0.2	1.0	0.2
<b>A1-3</b>	0.5	0.5	1.0	0.5
<b>A1-3</b>	0.1	0.1	1.0	0.1
<b>A1-4</b>	0.1	0.1	1.0	0.1
<b>A1-4</b>	0.3	0.3	1.0	0.3
<b>A1-4</b>	0.1	0.1	1.0	0.1
<b>A1-6</b>	1.0	1.0	1.0	1.0
<b>A1-6</b>	0.1	0.1	1.0	0.1
<b>A1-6</b>	0.5	0.5	1.0	0.5
<b>A1-8</b>	0.5	0.5	1.0	0.5
<b>A1-8</b>	0.1	0.1	1.0	0.1
<b>A1-8</b>	0.2	0.2	1.0	0.2
<b>A1-10</b>	0.1	0.1	1.0	0.1
<b>A1-10</b>	0.5	0.5	1.0	0.5
<b>A1-10</b>	1.0	1.0	1.0	1.0
<b>A1-12</b>	0.1	0.1	1.0	0.1
<b>A1-12</b>	0.5	0.5	1.0	0.5
<b>A1-12</b>	1.0	1.0	1.0	1.0
<b>A2-1</b>	0.1	0.1	1.0	0.1
<b>A2-1</b>	2.0	2.0	1.0	2.0
<b>A2-1</b>	0.1	0.1	1.0	0.1
<b>A2-2</b>	0.1	0.1	1.0	0.1
<b>A2-2</b>	0.1	0.1	1.0	0.1
<b>A2-2</b>	0.5	0.5	1.0	0.5
<b>A2-3</b>	0.1	0.1	1.0	0.1
<b>A2-3</b>	0.5	0.5	1.0	0.5
<b>A2-3</b>	1.0	1.0	1.0	1.0

<b>A2-4</b>	1.0	1.0	1.0	1.0
<b>A2-4</b>	0.1	0.1	1.0	0.1
<b>A2-4</b>	1.0	1.0	1.0	1.0
<b>A2-6</b>	0.5	0.5	1.0	0.5
<b>A2-6</b>	1.0	1.0	1.0	1.0
<b>A2-6</b>	0.1	0.1	1.0	0.1
<b>A2-8</b>	0.1	0.1	1.0	0.1
<b>A2-8</b>	0.2	0.2	1.0	0.2
<b>A2-8</b>	0.5	0.5	1.0	0.5
<b>A2-10</b>	0.5	0.5	1.0	0.5
<b>A2-10</b>	1.0	1.0	1.0	1.0
<b>A2-10</b>	0.3	0.3	1.0	0.3
<b>A3-1</b>	1.0	1.0	1.0	1.0
<b>A3-1</b>	0.2	0.2	1.0	0.2
<b>A3-1</b>	0.5	1.0	0.5	0.8
<b>A3-2</b>	0.1	3.0	0.0	1.6
<b>A3-2</b>	0.2	0.2	1.0	0.2
<b>A3-2</b>	0.1	0.1	1.0	0.1
<b>A3-3</b>	0.0	0.0	1.0	0.0
<b>A3-3</b>	0.3	0.3	1.0	0.3
<b>A3-3</b>	0.0	0.0	1.0	0.0
<b>A3-4</b>	0.0	0.0	1.0	0.0
<b>A3-4</b>	0.0	0.0	1.0	0.0
<b>A3-4</b>	0.2	0.2	1.0	0.2
<b>A3-8</b>	0.0	0.0	1.0	0.0
<b>A3-8</b>	0.0	0.0	1.0	0.0
<b>A3-8</b>	0.0	0.0	1.0	0.0
<b>A3-10</b>	0.0	0.0	1.0	0.0
<b>A3-10</b>	0.0	0.0	1.0	0.0
<b>A3-10</b>	0.1	0.1	1.0	0.1
<b>B1-2</b>	0.1	0.1	1.0	0.1
<b>B1-2</b>	0.1	0.1	1.0	0.1
<b>B1-2</b>	0.1	0.1	1.0	0.1
<b>B1-3</b>	0.1	0.1	1.0	0.1
<b>B1-3</b>	0.1	0.1	1.0	0.1
<b>B1-3</b>	0.1	0.1	1.0	0.1
<b>B1-3</b>	0.1	0.1	1.0	0.1
<b>B1-4</b>	0.1	0.5	0.2	0.3
<b>B1-4</b>	0.1	0.1	1.0	0.1
<b>B1-4</b>	0.1	0.1	1.0	0.1

<b>B1-6</b>	0.1	0.1	1.0	0.1
<b>B1-6</b>	0.1	0.1	1.0	0.1
<b>B1-6</b>	0.1	0.1	1.0	0.1
<b>B1-8</b>	0.2	0.2	1.0	0.2
<b>B1-8</b>	0.1	0.1	1.0	0.1
<b>B1-8</b>	0.1	0.1	1.0	0.1
<b>B1-10</b>	0.2	0.2	1.0	0.2
<b>B1-10</b>	0.2	2.0	0.1	1.1
<b>B1-10</b>	0.2	0.2	1.0	0.2
<b>B1-12</b>	0.2	0.2	1.0	0.2
<b>B1-12</b>	0.1	0.1	1.0	0.1
<b>B1-12</b>	0.1	0.1	1.0	0.1
<b>B1-14</b>	0.1	0.1	1.0	0.1
<b>B1-14</b>	0.1	0.1	1.0	0.1
<b>B1-14</b>	0.2	0.2	1.0	0.2
<b>B1-16</b>	0.1	0.1	1.0	0.1
<b>B1-16</b>	0.1	0.1	1.0	0.1
<b>B1-16</b>	0.2	0.2	1.0	0.2
<b>B1-17</b>	0.1	0.1	1.0	0.1
<b>B1-17</b>	0.1	0.1	1.0	0.1
<b>B1-17</b>	0.1	0.1	1.0	0.1
<b>B2-1</b>	0.1	0.1	1.0	0.1
<b>B2-1</b>	0.2	0.2	1.0	0.2
<b>B2-1</b>	0.1	0.1	1.0	0.1
<b>B2-2</b>	0.1	0.1	1.0	0.1
<b>B2-2</b>	0.2	0.2	1.0	0.2
<b>B2-2</b>	0.1	0.1	1.0	0.1
<b>B2-3</b>	0.1	0.1	1.0	0.1
<b>B2-3</b>	0.2	0.2	1.0	0.2
<b>B2-3</b>	0.1	0.1	1.0	0.1
<b>B2-4</b>	0.1	0.1	1.0	0.1
<b>B2-4</b>	0.2	0.2	1.0	0.2
<b>B2-4</b>	0.1	0.1	1.0	0.1
<b>B2-6</b>	0.2	0.2	1.0	0.2
<b>B2-6</b>	0.2	0.2	1.0	0.2
<b>B2-6</b>	0.1	0.1	1.0	0.1
<b>B2-8</b>	0.2	0.2	1.0	0.2
<b>B2-8</b>	0.2	0.2	1.0	0.2
<b>B2-8</b>	0.1	0.1	1.0	0.1
<b>B2-10</b>	0.2	0.2	1.0	0.2

<b>B2-10</b>	0.2	0.2	1.0	0.2
<b>B2-10</b>	0.2	0.2	1.0	0.2
<b>B2-12</b>	0.2	0.2	1.0	0.2
<b>B2-12</b>	0.5	0.5	1.0	0.5
<b>B2-12</b>	0.5	0.5	1.0	0.5
<b>C1-1</b>	0.1	2.0	0.1	1.1
<b>C1-1</b>	0.1	2.0	0.1	1.1
<b>C1-1</b>	0.1	2.0	0.1	1.1
<b>C1-2</b>	0.3	12.0	0.0	6.2
<b>C1-2</b>	0.3	12.0	0.0	6.2
<b>C1-2</b>	0.1	5.0	0.0	2.6
<b>C1-3</b>	0.1	10.0	0.0	5.1
<b>C1-3</b>	0.2	10.0	0.0	5.1
<b>C1-3</b>	0.1	5.0	0.0	2.6
<b>C1-4</b>	1.0	5.0	0.2	3.0
<b>C1-4</b>	0.7	6.0	0.1	3.4
<b>C1-5</b>	2.0	8.0	0.3	5.0
<b>C1-5</b>	1.0	8.0	0.1	4.5
<b>C1-6</b>	1.0	10.0	0.1	5.5
<b>C1-7</b>	0.0	0.0	NA	0.0
<b>C2-1</b>	0.1	0.1	1.0	0.1
<b>C2-1</b>	0.1	0.1	1.0	0.1
<b>C2-1</b>	0.1	0.1	1.0	0.1
<b>C2-3</b>	0.0	0.0	NA	0.0
<b>C2-4</b>	0.0	0.0	NA	0.0
<b>C2-5</b>	0.0	0.0	NA	0.0
<b>C3-1</b>	0.0	0.0	NA	0.0
<b>C3-2</b>	1.0	10.0	0.1	5.5
<b>C3-3</b>	1.0	4.0	0.3	2.5
<b>C3-3</b>	1.0	3.0	0.3	2.0
<b>C3-4</b>	1.0	1.0	1.0	1.0
<b>C3-5</b>	0.0	0.0	NA	0.0
<b>C3-6</b>	0.0	0.0	NA	0.0
<b>B3-1</b>	0.3	0.3	1.0	0.3
<b>B3-1</b>	0.1	0.1	1.0	0.1
<b>B3-1</b>	0.2	0.2	1.0	0.2
<b>B3-2</b>	0.3	0.3	1.0	0.3
<b>B3-2</b>	0.2	0.2	1.0	0.2
<b>B3-2</b>	0.1	0.1	1.0	0.1
<b>B3-3</b>	0.1	0.1	1.0	0.1

<b>B3-3</b>	0.1	0.1	1.0	0.1
<b>B3-3</b>	0.2	0.2	1.0	0.2
<b>B3-4</b>	0.2	0.2	1.0	0.2
<b>B3-4</b>	0.1	0.1	1.0	0.1
<b>B3-4</b>	0.1	0.1	1.0	0.1
<b>B3-6</b>	0.4	0.4	1.0	0.4
<b>B3-6</b>	0.3	0.3	1.0	0.3
<b>B3-6</b>	0.3	0.3	1.0	0.3
<b>B3-8</b>	0.5	10.0	0.1	5.3
<b>B3-8</b>	0.5	5.0	0.1	2.8
<b>B3-8</b>	0.5	5.0	0.1	2.8
<b>B3-10</b>	0.7	4.0	0.2	2.4
<b>B3-10</b>	0.5	4.0	0.1	2.3
<b>B3-10</b>	0.4	0.4	1.0	0.4
<b>B3-12</b>	0.6	11.0	0.1	5.8
<b>B3-12</b>	0.6	11.0	0.1	5.8
<b>B3-12</b>	0.6	5.0	0.1	2.8
<b>B3-14</b>	0.2	0.2	1.0	0.2
<b>B3-14</b>	0.2	0.2	1.0	0.2
<b>B3-14</b>	0.2	0.2	1.0	0.2
<b>B3-16</b>	0.2	2.0	0.1	1.1
<b>B3-16</b>	0.2	1.0	0.2	0.6
<b>B3-16</b>	0.2	0.2	1.0	0.2

**Table B4:** Ice grain dimensions

<b>Core Segment</b>	<b>Thin Section</b>	<b>Grain Length (mm)</b>	<b>Grain Width (mm)</b>	<b>Grain Aspect</b>	<b>Grain Size (mm)</b>
A1-1	Horizontal	10	17	0.6	13.5
A1-1	Horizontal	10	7	1.4	8.5
A1-1	Horizontal	1	1	1.0	1.0
A1-1	Horizontal	5	4	1.3	4.5
A1-1	Horizontal	12	12	1.0	12.0
A1-1	Horizontal	4	4	1.0	4.0
A1-1	Horizontal	2	3	0.7	2.5
A1-1	Horizontal	4	4	1.0	4.0
A1-1	Horizontal	3	4	0.8	3.5
A1-1	Horizontal	7	9	0.8	8.0
A1-6	Horizontal	30	25	1.2	27.5
A1-6	Horizontal	20	16	1.3	18.0
A1-6	Horizontal	30	17	1.8	23.5
A1-6	Horizontal	6	4	1.5	5.0
A1-6	Horizontal	10	7	1.4	8.5
A1-6	Horizontal	13	20	0.7	16.5
A1-6	Horizontal	29	16	1.8	22.5
A1-6	Horizontal	4	4	1.0	4.0
A1-6	Horizontal	9	10	0.9	9.5
A1-6	Horizontal	10	4	2.5	7.0
A1-12	Horizontal	6	9	0.7	7.5
A1-12	Horizontal	5	6	0.8	5.5
A1-12	Horizontal	8	7	1.1	7.5
A1-12	Horizontal	2	3	0.7	2.5
A1-12	Horizontal	2	2	1.0	2.0
A1-12	Horizontal	7	9	0.8	8.0
A1-12	Horizontal	4	4	1.0	4.0
A1-12	Horizontal	6	7	0.9	6.5
A1-12	Horizontal	5	8	0.6	6.5
A1-12	Horizontal	3	3	1.0	3.0
A2-1	Horizontal	7	5	1.4	6.0
A2-1	Horizontal	14	10	1.4	12.0
A2-1	Horizontal	25	25	1.0	25.0
A2-1	Horizontal	14	9	1.6	11.5
A2-1	Horizontal	13	5	2.6	9.0

<b>A2-1</b>	Horizontal	9	10	0.9	9.5
<b>A2-1</b>	Horizontal	11	11	1.0	11.0
<b>A2-1</b>	Horizontal	12	10	1.2	11.0
<b>A2-1</b>	Horizontal	13	20	0.7	16.5
<b>A2-1</b>	Horizontal	10	13	0.8	11.5
<b>A2-1</b>	Vertical	13	6	2.2	9.5
<b>A2-1</b>	Vertical	18	10	1.8	14.0
<b>A2-1</b>	Vertical	5	5	1.0	5.0
<b>A2-1</b>	Vertical	30	30	1.0	30.0
<b>A2-1</b>	Vertical	17	8	2.1	12.5
<b>A2-1</b>	Vertical	10	8	1.3	9.0
<b>A2-1</b>	Vertical	12	9	1.3	10.5
<b>A2-1</b>	Vertical	12	7	1.7	9.5
<b>A2-1</b>	Vertical	10	4	2.5	7.0
<b>A2-1</b>	Vertical	15	17	0.9	16.0
<b>A2-6</b>	Horizontal	15	18	0.8	16.5
<b>A2-6</b>	Horizontal	11	9	1.2	10.0
<b>A2-6</b>	Horizontal	11	10	1.1	10.5
<b>A2-6</b>	Horizontal	12	18	0.7	15.0
<b>A2-6</b>	Horizontal	14	12	1.2	13.0
<b>A2-6</b>	Horizontal	9	10	0.9	9.5
<b>A2-6</b>	Horizontal	4	4	1.0	4.0
<b>A2-6</b>	Horizontal	5	5	1.0	5.0
<b>A2-6</b>	Horizontal	5	3	1.7	4.0
<b>A2-6</b>	Horizontal	4	3	1.3	3.5
<b>A2-6</b>	Vertical	12	10	1.2	11.0
<b>A2-6</b>	Vertical	9	11	0.8	10.0
<b>A2-6</b>	Vertical	5	5	1.0	5.0
<b>A2-6</b>	Vertical	8	7	1.1	7.5
<b>A2-6</b>	Vertical	11	12	0.9	11.5
<b>A2-6</b>	Vertical	16	18	0.9	17.0
<b>A2-6</b>	Vertical	4	10	0.4	7.0
<b>A2-6</b>	Vertical	14	8	1.8	11.0
<b>A2-6</b>	Vertical	15	13	1.2	14.0
<b>A2-6</b>	Vertical	4	3	1.3	3.5
<b>A2-10</b>	Horizontal	17	18	0.9	17.5
<b>A2-10</b>	Horizontal	11	14	0.8	12.5
<b>A2-10</b>	Horizontal	10	12	0.8	11.0
<b>A2-10</b>	Horizontal	9	8	1.1	8.5
<b>A2-10</b>	Horizontal	12	19	0.6	15.5

<b>A2-10</b>	Horizontal	10	11	0.9	10.5
<b>A2-10</b>	Horizontal	20	15	1.3	17.5
<b>A2-10</b>	Horizontal	13	14	0.9	13.5
<b>A2-10</b>	Horizontal	7	9	0.8	8.0
<b>A2-10</b>	Horizontal	15	11	1.4	13.0
<b>A2-10</b>	Vertical	16	15	1.1	15.5
<b>A2-10</b>	Vertical	7	10	0.7	8.5
<b>A2-10</b>	Vertical	37	60	0.6	48.5
<b>A2-10</b>	Vertical	15	10	1.5	12.5
<b>A2-10</b>	Vertical	23	25	0.9	24.0
<b>A2-10</b>	Vertical	17	10	1.7	13.5
<b>A2-10</b>	Vertical	9	7	1.3	8.0
<b>A2-10</b>	Vertical	13	12	1.1	12.5
<b>A2-10</b>	Vertical	9	12	0.8	10.5
<b>A2-10</b>	Vertical	9	8	1.1	8.5
<b>A3-1</b>	Horizontal	15	15	1.0	15.0
<b>A3-1</b>	Horizontal	7	10	0.7	8.5
<b>A3-1</b>	Horizontal	7	7	1.0	7.0
<b>A3-1</b>	Horizontal	7	6	1.2	6.5
<b>A3-1</b>	Horizontal	13	10	1.3	11.5
<b>A3-1</b>	Horizontal	12	12	1.0	12.0
<b>A3-1</b>	Horizontal	10	7	1.4	8.5
<b>A3-1</b>	Horizontal	6	5	1.2	5.5
<b>A3-1</b>	Horizontal	7	7	1.0	7.0
<b>A3-1</b>	Horizontal	9	8	1.1	8.5
<b>A3-7</b>	Horizontal	14	13	1.1	13.5
<b>A3-7</b>	Horizontal	5	6	0.8	5.5
<b>A3-7</b>	Horizontal	13	12	1.1	12.5
<b>A3-7</b>	Horizontal	9	10	0.9	9.5
<b>A3-7</b>	Horizontal	7	7	1.0	7.0
<b>A3-7</b>	Horizontal	14	9	1.6	11.5
<b>A3-7</b>	Horizontal	4	4	1.0	4.0
<b>A3-7</b>	Horizontal	5	6	0.8	5.5
<b>A3-7</b>	Horizontal	12	13	0.9	12.5
<b>A3-7</b>	Horizontal	5	4	1.3	4.5
<b>A3-10</b>	Horizontal	16	19	0.8	17.5
<b>A3-10</b>	Horizontal	8	9	0.9	8.5
<b>A3-10</b>	Horizontal	14	19	0.7	16.5
<b>A3-10</b>	Horizontal	11	13	0.8	12.0
<b>A3-10</b>	Horizontal	7	5	1.4	6.0

<b>A3-10</b>	Horizontal	10	12	0.8	11.0
<b>A3-10</b>	Horizontal	14	18	0.8	16.0
<b>A3-10</b>	Horizontal	13	10	1.3	11.5
<b>A3-10</b>	Horizontal	9	12	0.8	10.5
<b>A3-10</b>	Horizontal	9	7	1.3	8.0
<b>B1-2</b>	Horizontal	13	20	0.7	16.5
<b>B1-2</b>	Horizontal	12	30	0.4	21.0
<b>B1-2</b>	Horizontal	27	68	0.4	47.5
<b>B1-2</b>	Horizontal	15	8	1.9	11.5
<b>B1-2</b>	Horizontal	17	9	1.9	13.0
<b>B1-2</b>	Horizontal	17	40	0.4	28.5
<b>B1-2</b>	Horizontal	15	14	1.1	14.5
<b>B1-2</b>	Horizontal	19	12	1.6	15.5
<b>B1-2</b>	Horizontal	18	19	0.9	18.5
<b>B1-2</b>	Horizontal	30	20	1.5	25.0
<b>B1-2</b>	Vertical	14	15	0.9	14.5
<b>B1-2</b>	Vertical	12	20	0.6	16.0
<b>B1-2</b>	Vertical	18	18	1.0	18.0
<b>B1-2</b>	Vertical	7	8	0.9	7.5
<b>B1-2</b>	Vertical	12	17	0.7	14.5
<b>B1-2</b>	Vertical	16	19	0.8	17.5
<b>B1-2</b>	Vertical	20	35	0.6	27.5
<b>B1-2</b>	Vertical	7	9	0.8	8.0
<b>B1-2</b>	Vertical	20	12	1.7	16.0
<b>B1-2</b>	Vertical	7	5	1.4	6.0
<b>B1-5</b>	Horizontal	9	10	0.9	9.5
<b>B1-5</b>	Horizontal	9	12	0.8	10.5
<b>B1-5</b>	Horizontal	20	20	1.0	20.0
<b>B1-5</b>	Horizontal	20	11	1.8	15.5
<b>B1-5</b>	Horizontal	24	11	2.2	17.5
<b>B1-5</b>	Horizontal	5	7	0.7	6.0
<b>B1-5</b>	Horizontal	19	6	3.2	12.5
<b>B1-5</b>	Horizontal	4	4	1.0	4.0
<b>B1-5</b>	Horizontal	8	7	1.1	7.5
<b>B1-5</b>	Horizontal	23	18	1.3	20.5
<b>B1-10</b>	Horizontal	6	10	0.6	8.0
<b>B1-10</b>	Horizontal	7	5	1.4	6.0
<b>B1-10</b>	Horizontal	22	7	3.1	14.5
<b>B1-10</b>	Horizontal	15	9	1.7	12.0
<b>B1-10</b>	Horizontal	6	15	0.4	10.5

<b>B1-10</b>	Horizontal	15	32	0.5	23.5
<b>B1-10</b>	Horizontal	11	23	0.5	17.0
<b>B1-10</b>	Horizontal	7	30	0.2	18.5
<b>B1-10</b>	Horizontal	12	9	1.3	10.5
<b>B1-10</b>	Horizontal	6	19	0.3	12.5
<b>B1-10</b>	Vertical	7	6	1.2	6.5
<b>B1-10</b>	Vertical	7	17	0.4	12.0
<b>B1-10</b>	Vertical	7	5	1.4	6.0
<b>B1-10</b>	Vertical	25	20	1.3	22.5
<b>B1-10</b>	Vertical	9	8	1.1	8.5
<b>B1-10</b>	Vertical	22	15	1.5	18.5
<b>B1-10</b>	Vertical	6	4	1.5	5.0
<b>B1-10</b>	Vertical	4	3	1.3	3.5
<b>B1-10</b>	Vertical	20	16	1.3	18.0
<b>B1-10</b>	Vertical	11	12	0.9	11.5
<b>B1-16</b>	Vertical	12	10	1.2	11.0
<b>B1-16</b>	Vertical	7	10	0.7	8.5
<b>B1-16</b>	Vertical	6	5	1.2	5.5
<b>B1-16</b>	Vertical	2	3	0.7	2.5
<b>B1-16</b>	Vertical	15	10	1.5	12.5
<b>B1-16</b>	Vertical	13	5	2.6	9.0
<b>B1-16</b>	Vertical	7	7	1.0	7.0
<b>B1-16</b>	Vertical	9	7	1.3	8.0
<b>B1-16</b>	Vertical	9	8	1.1	8.5
<b>B1-16</b>	Vertical	2	2	1.0	2.0
<b>B1-17</b>	Horizontal	5	7	0.7	6.0
<b>B1-17</b>	Horizontal	6	7	0.9	6.5
<b>B1-17</b>	Horizontal	6	8	0.8	7.0
<b>B1-17</b>	Horizontal	4	4	1.0	4.0
<b>B1-17</b>	Horizontal	9	4	2.3	6.5
<b>B1-17</b>	Horizontal	3	3	1.0	3.0
<b>B1-17</b>	Horizontal	4	6	0.7	5.0
<b>B1-17</b>	Horizontal	2	2	1.0	2.0
<b>B1-17</b>	Horizontal	5	3	1.7	4.0
<b>B1-17</b>	Horizontal	7	3	2.3	5.0
<b>B1-17</b>	Horizontal	4	4	1.0	4.0
<b>B1-17</b>	Horizontal	9	8	1.1	8.5
<b>B1-17</b>	Horizontal	7	9	0.8	8.0
<b>B1-17</b>	Horizontal	10	20	0.5	15.0
<b>B1-17</b>	Horizontal	5	5	1.0	5.0

<b>B2-1</b>	Horizontal	5	8	0.6	6.5
<b>B2-1</b>	Horizontal	10	10	1.0	10.0
<b>B2-1</b>	Horizontal	15	15	1.0	15.0
<b>B2-1</b>	Horizontal	15	13	1.2	14.0
<b>B2-1</b>	Horizontal	17	17	1.0	17.0
<b>B2-1</b>	Horizontal	21	23	0.9	22.0
<b>B2-1</b>	Horizontal	4	4	1.0	4.0
<b>B2-1</b>	Horizontal	4	3	1.3	3.5
<b>B2-1</b>	Horizontal	29	24	1.2	26.5
<b>B2-1</b>	Horizontal	11	20	0.6	15.5
<b>B2-5</b>	Horizontal	8	19	0.4	13.5
<b>B2-5</b>	Horizontal	14	34	0.4	24.0
<b>B2-5</b>	Horizontal	6	11	0.5	8.5
<b>B2-5</b>	Horizontal	10	14	0.7	12.0
<b>B2-5</b>	Horizontal	5	7	0.7	6.0
<b>B2-5</b>	Horizontal	9	24	0.4	16.5
<b>B2-5</b>	Horizontal	28	20	1.4	24.0
<b>B2-5</b>	Horizontal	4	4	1.0	4.0
<b>B2-5</b>	Horizontal	6	9	0.7	7.5
<b>B2-5</b>	Horizontal	6	19	0.3	12.5
<b>B2-12</b>	Horizontal	10	28	0.4	19.0
<b>B2-12</b>	Horizontal	10	16	0.6	13.0
<b>B2-12</b>	Horizontal	32	17	1.9	24.5
<b>B2-12</b>	Horizontal	2	5	0.4	3.5
<b>B2-12</b>	Horizontal	8	25	0.3	16.5
<b>B2-12</b>	Horizontal	5	11	0.5	8.0
<b>B2-12</b>	Horizontal	16	31	0.5	23.5
<b>B2-12</b>	Horizontal	10	17	0.6	13.5
<b>B2-12</b>	Horizontal	5	7	0.7	6.0
<b>B2-12</b>	Horizontal	7	10	0.7	8.5
<b>B2-12</b>	Vertical	14	10	1.4	12.0
<b>B2-12</b>	Vertical	9	9	1.0	9.0
<b>B2-12</b>	Vertical	45	13	3.5	29.0
<b>B2-12</b>	Vertical	13	12	1.1	12.5
<b>B2-12</b>	Vertical	23	10	2.3	16.5
<b>B2-12</b>	Vertical	17	17	1.0	17.0
<b>B2-12</b>	Vertical	6	5	1.2	5.5
<b>B2-12</b>	Vertical	19	17	1.1	18.0
<b>B2-12</b>	Vertical	7	7	1.0	7.0
<b>B2-12</b>	Vertical	8	5	1.6	6.5

<b>B3-2</b>	Horizontal	14	10	1.4	12.0
<b>B3-2</b>	Horizontal	33	10	3.3	21.5
<b>B3-2</b>	Horizontal	88	40	2.2	64.0
<b>B3-2</b>	Horizontal	88	55	1.6	71.5
<b>B3-2</b>	Vertical	100	88	1.1	94.0
<b>B3-2</b>	Vertical	45	50	0.9	47.5
<b>B3-6</b>	Horizontal	8	5	1.6	6.5
<b>B3-6</b>	Horizontal	4	3	1.3	3.5
<b>B3-6</b>	Horizontal	10	13	0.8	11.5
<b>B3-6</b>	Horizontal	8	6	1.3	7.0
<b>B3-6</b>	Horizontal	1	1	1.0	1.0
<b>B3-6</b>	Horizontal	6	6	1.0	6.0
<b>B3-6</b>	Horizontal	6	8	0.8	7.0
<b>B3-6</b>	Horizontal	40	75	0.5	57.5
<b>B3-6</b>	Horizontal	55	40	1.4	47.5
<b>B3-6</b>	Horizontal	50	50	1.0	50.0
<b>B3-8</b>	Horizontal	88	55	1.6	71.5
<b>B3-8</b>	Horizontal	70	17	4.1	43.5
<b>B3-8</b>	Horizontal	75	10	7.5	42.5
<b>B3-8</b>	Horizontal	88	30	2.9	59.0
<b>B3-8</b>	Vertical	68	88	0.8	78.0
<b>B3-8</b>	Vertical	39	17	2.3	28.0
<b>B3-12</b>	Horizontal	11	7	1.6	9.0
<b>B3-12</b>	Horizontal	14	10	1.4	12.0
<b>B3-12</b>	Horizontal	60	12	5.0	36.0
<b>B3-12</b>	Horizontal	5	4	1.3	4.5
<b>B3-12</b>	Horizontal	61	76	0.8	68.5
<b>B3-12</b>	Vertical	60	77	0.8	68.5
<b>B3-12</b>	Vertical	65	55	1.2	60.0
<b>B3-12</b>	Vertical	12	5	2.4	8.5
<b>B3-12</b>	Vertical	16	9	1.8	12.5
<b>C1-1</b>	Horizontal	20	42	0.5	31.0
<b>C1-1</b>	Horizontal	23	31	0.7	27.0
<b>C1-1</b>	Horizontal	9	13	0.7	11.0
<b>C1-1</b>	Horizontal	21	20	1.1	20.5
<b>C1-1</b>	Horizontal	10	45	0.2	27.5
<b>C1-1</b>	Horizontal	20	6	3.3	13.0
<b>C1-1</b>	Vertical	160	60	2.7	110.0
<b>C1-1</b>	Vertical	125	30	4.2	77.5
<b>C1-1</b>	Vertical	95	10	9.5	52.5

<b>C1-1</b>	Vertical	122	15	8.1	68.5
<b>C1-1</b>	Vertical	160	24	6.7	92.0
<b>C1-7</b>	Vertical	150	66	2.3	108.0
<b>C1-7</b>	Vertical	92	16	5.8	54.0
<b>C1-8</b>	Horizontal	49	88	0.6	68.5
<b>C1-8</b>	Horizontal	25	88	0.3	56.5
<b>C1-8</b>	Horizontal	29	88	0.3	58.5
<b>C2-3</b>	Horizontal	13	30	0.4	21.5
<b>C2-3</b>	Horizontal	50	40	1.3	45.0
<b>C2-3</b>	Horizontal	30	50	0.6	40.0
<b>C2-3</b>	Horizontal	70	43	1.6	56.5
<b>C2-5</b>	Horizontal	88	88	1.0	88.0
<b>C3-5</b>	Vertical	57	88	0.6	72.5